# Phononic Crystals to Control the Propagation of Elastic Waves

Jinfeng Zhao

**THESE DE DOCTORAT DE**
**L'UNIVERSITE PIERRE ET MARIE CURIE**

**École Doctorale des Sciences Mécaniques, Acoustique, Electronique et Robotique de Paris**

Pour obtenir le grade de

**Docteur de l'Université Pierre et Marie Curie**

Présentée par :

**Jinfeng Zhao**

# Phononic Crystals to Control the Propagation of Elastic Waves

préparée à l'**Institut des NanoSciences de Paris**

Soutenance publique le 9 Janvier 2015 devant le jury

*Rapporteurs*:

**M. Badreddine Assouar**, Chargé de Recherche CNRS (HDR), Institut Jean Lamour, Université de Lorraine

**M. Yan Pennec**, Professeur, Institut d'Electronique, de Microélectronique et de Nanotechnoligie, Université Lille 1

*Examinatrices*:

**Mme Agnès Maître**, Professeure, Institut des NanoSciences de Paris, Université Pierre et Marie Curie

**Mme Sarah Benchabane**, Chargée de Recherche CNRS, Institut FEMTO-ST, Université de Franche-Comté

*Directeurs de thèse*:

**M. Bernard Bonello**, Directeur de Recherche CNRS, Institut des NanoSciences de Paris, Université Pierre et Marie Curie

**Mme Olga Boyko-Kazymyrenko**, Maître de Conférence, Institut des NanoSciences de Paris, Université Pierre et Marie Curie

# Contents

# General Introduction

In nature, many structures repeat themselves in space, from atoms to butterfly wings. More than twenty years ago, it has been proposed [i] to construct artificial elastic structures, *the phononic crystals* (PCs), by the repetition of inclusions embedded into a host matrix made of a different material. As a consequence of the periodicity of the elastic properties in the direct space, the elastic waves propagating in a PC are characterized by a periodic wavenumber in the reciprocal space. Equivalently, the band structure repeats itself in the Brillouin zone. Such a "wavenumber trap" in the Brillouin zone has given birth to several unconventional and even exotic properties for elastic waves propagating in PCs. Among these, one of the most widely studied is the hindering for the propagation in PC of any wave in some frequency bands, *i.e.*, the *bandgap*. Apart from this, the unit cell of a PC, acting as an atom or a molecule in a solid, can be artificially modulated to control the wave propagation; e.g. by removing one inclusion in an infinite PC, one creates a defect that may trap the elastic energy. By removing a line of inclusions, it helps guiding the wave along this line...

Specific designs of the unit cell also enable to control the dispersion curves of a PC. This is the case in particular when one deals with one of the most important applications of acoustics as the imaging acoustic is. Actually, new types of acoustic lenses, different from conventional ones, can be engineered from a PC. Conventional acoustic lenses, which generally have a precise geometrical shape as for example the Fresnel lenses or the elliptical ones, can be used to get an image of the source or to focalize incident waves. Indeed, under certain conditions, plane waves can alter into elliptical or circular wave by using transducers of similar shape, resulting them to converge to a small region. However, limited by the geometrical shape of the lens or by the arrangement of transducers, these lenses are usually designed to work within a narrow frequency range, which makes it hard to tune the operating frequencies or to combine them with other devices.

PC based acoustic lenses, on the other hand, can be engineered to have a second acoustic band featuring a negative slope in the Brillouin zone, which leads to

[i] Kushwaha *et al.*, Physical Review Letters 71: 2022, 1993

the unusual *negative refraction* of waves due to the opposite directions between the group velocity and the phase velocity. Such PC based structures with just a flat shape can give an almost perfect image of the source owing to the negative refraction. Indeed, in 2009, [ii] a PC-based lens was used to give an image of a point source with a resolution at the focus less than half a wavelength, *i.e.*, beyond the diffraction limit. The secret lies in the restoring of evanescent components emitted by the source, owing to the negative index, making PC-based acoustic lenses to overcome the diffraction limit as do the Maxwell fish-eye lenses, [iii] or the super-oscillations. [iv] Moreover, the PCs keep the easy modification of the unit cell or of the overall geometric shape.

For a long time, flat PC-based acoustic lenses have been investigated within the high frequency range (*i.e.*, above the band gap) in relation with imaging acoustic using the negative refraction processes. This implies uniform shape for all the unit cells in the heterostructure and a real periodicity along two perpendicular directions in space. The independent control of each unit cell in the PC, on the other hand, has triggered a new type of acoustic lenses, namely the g*radient-index* (*GRIN*) *PCs*, in the Cartesian, cylindrical and spherical coordinates. The principle lies in the careful modification of unit cells to obtain a varying sound velocity along some directions. When an incident wave confronts such a gradient of velocity, its trace of energy is shifted as it is the case for light impinging on a graded optical lens: the phenomenon is nothing else than an effect that can be daily observed in nature the "mirage effect".

Cartesian artificial acoustic lenses, which generally have a flat shape, can focalize, collimate or render divergent incident waves at low frequency with *a positive refractive index*. The potential applications of GRIN PC include the relatively large-band focalization and the convenient manipulation of elastic waves. These acoustical lenses offer the simplest and least expensive route to obtain a small focal zone with fairly high lateral resolution and energy efficiency. Although many studies have concentrated on this topic, very few address the performances of focalization, including the *location of the focus*, the *gain factor*, and the *focusing resolution*. Let us consider the location of the focus for example. As in optics, it may be affected by the operating wavelength or some defects of the PC. In terms of focusing resolution, whether it can overcome the diffraction limit or not, poses an interesting question and understanding the underlying physical mechanisms remains a challenge. Answering these questions not only requires numerical or experimental investigations but also further theoretical views.

This PhD research work aims at studying the focusing of acoustic waves us-

[ii] Sukhovich *et al.*, Physical Review Letters, 102: 154301, 2009
[iii] Ma *et al.*, New Journal of Physics, 14(2): 025001, 2012
[iv] Huang and Zheludev, Nano Letters, 9(3): 1249, 2009

ing GRIN PCs. The study enters the more general scheme of manipulating the elastic wave propagation using sub-wavelength unit, or equivalently to act on the trajectories of modes within the first acoustic band. Because both of them are of very broad interest in many fields of pure and applied physics or mechanics, such as non-destructive testing, telecommunication, geophysics and so on, we have been mainly interested in the lowest order anti-symmetric ($A_0$) Lamb mode and in the surface acoustic waves (Rayleigh mode). The manuscript is organized as follows:

In the first chapter we introduce the elastic waves focusing by flat acoustic lenses. We recall the concepts of negative index and negative refraction. We further describe the cutting edge of the researches devoted to the focusing with a positive-index PC.

The second chapter concentrates on the propagation of $A_0$ Lamb mode inside a GRIN PC. In this chapter, a new formalism to calculate the ray trajectories is proposed. This formalism is based on the consideration of the local anisotropy in the GRIN PC. The ray trajectories are calculated and compared to numerical and experimental results. The formalism is used all through this work.

Following the study of the focusing inside the GRIN PC, the third chapter deals with the focusing of $A_0$ Lamb mode downstream the GRIN PC. Through the analysis both of the ray trajectories and of the transverse wavenumber, we investigate the focusing pattern. To enhance the focusing achievements, we propose a resonant structure to get the desired Fourier components at the focus. Then, we present both numerical and experimental results in order to verify the focusing resolution.

In the fourth chapter, we investigate the focusing of Rayleigh waves, both inside and outside the GRIN PC. The formalism described in chapter 2 is extended to the case of surface waves. The ray trajectories together with some experimental results are used to analyze the focusing properties of the lens.

Lastly, we give the conclusions of this work.

# Chapter 1

# The controlled wave focalization in phononic crystals

## 1.1 Introduction

Engineered structures made of periodic inclusions in a matrix exhibit exotic and unique propagation properties not inherent to the individual constituent components. Proposed more than twenty years ago, the two-dimensional (2D) and three-dimensional (3D) PCs were conceived to have a similar band structure than other heterostructures, such as the photonic crystals or the electronic crystals.[1–4] The periodicity in the elastic or in the dielectric properties along one or two directions of space, enables them to have complete band gaps throughout the Brillouin zone, as it is the case for the one-dimensional (1D) super-lattices that have been investigated since more than half a century.[5] The key factor for acoustic bandgap engineering is the impedance mismatch between periodic elements, including the crystal and the surrounding medium. Actually, when an advancing wave front impinges a material with very large changes in the impedance, it tends to be back reflected. From then on, many interesting characteristics of elastic waves in PC can be anticipated, giving rise to many devices such as frequency filters, wave guides, noise absorbers, transducers, cloaks and so on.

Bandgap engineering may also help answering long standing questions in solid state matter studies, on the feasibility of shaping the elastic wave and focusing the elastic energy. These promising perspectives for acoustic imaging, which has been widely studied during the last ten years, are related to the fact that the PCs are systems in which one can control the wave propagation at the wavelength scale.

Considering that many studies refer to the fact that the acoustic imaging using PC based lenses is limited by the diffraction, J. Pendry stated in a seminal work[6] that negative index makes perfect lenses. A schematic of imaging with a negative

index PC (or photonic crystal) is shown in Figure 1.1. The part of the beam emitted by the source which impinges the interface with an angle above a critical value gets evanescent upon refraction. However, if the PC (or the photonic crystal) features a negative-index, the evanescent waves are amplified by the medium and these components may refocus and produce a near-field image.[6,7] The fine information carried by the restored evanescent components enables the resolution to be less than half a wavelength in the image plane, *i.e.*, to surpass the Abbé limit. This scheme applies whatever the waves are.

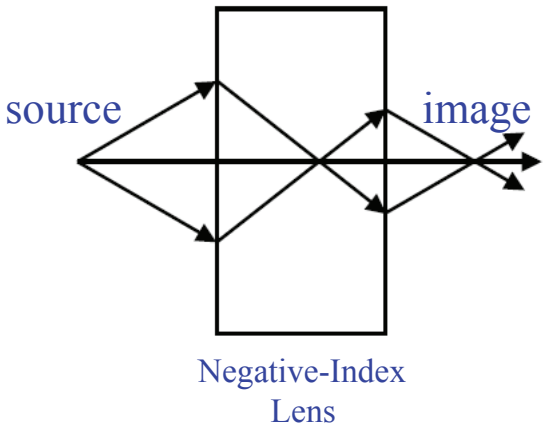


Figure 1.1: Scheme of imaging through a negative refraction lens.[6]

This so-called *superlensing* effect is the direct consequence of negative refraction of ultrasound in PCs. Let us note however that there are other artificial structures allowing for negative refraction: the acoustical metamaterials. They are generally formed by a set of local resonators embedded into a matrix. For homogenization theories to apply, these resonators must have lateral dimensions much less than the wavelength. If this condition is fulfilled, they may feature negative effective mass density and compressibility in certain frequency ranges, allowing for superlensing effect as well.

Similarly to the optical imaging by photonic crystals,[8,9] the acoustic imaging through PCs is only achievable within the bands above the first acoustic branch and can be tuned by controlling the elements in the PC in an *comprehensive manner*. Moreover, because of the exponential decay of the evanescent waves behind the lens, such superlensing effect is expected to appear only in the near field. To overcome this barrier, several authors[10–12] have proposed the negative-index *far-field superlens* which allows transferring behind the lens the evanescent components to the propagative ones. However, these systems still are designed to deal with elastic modes above the first acoustic branch.

*Gradually* altering the periodic elements along certain directions in space, pro-

vides another way to control the wave propagation. For example, the gradual modification of the filling ratio of inclusions creates in the PC, a graded sound velocity, or equivalently a graded refractive index, giving rise to the GRIN PCs which can produce an image of the wave source or focalize incident waves either in the Cartesian, cylindrical or spherical coordinates systems. Such wave focalization applies not only at frequencies above the first band gap in the dispersion curves but also for the first branch, at low frequency/large wavelength. For any mode in the first band, the dimensions of the unit cell are less than the wavelength, making suitable the homogenization of the elastic parameters of the GRIN PCs. All this shows that GRIN PCs can be designed and analyzed in the same way as it is generally done for the optical lenses. To now, flat GRIN PCs may lead to a focalization with highly concentrated elastic energy at frequencies in a broad range within the first band, distinguishing such positive-index systems from the negative-index ones. The focusing resolution can be less the wavelength.

In what follows, we analyze the focusing of elastic waves considering either the negative or the positive indices of PCs are presented together with their physical explanations.

## 1.2 Negative-index focusing of phononic crystal

### 1.2.1 Analysis of near-field superlensing focusing

The negative index comes from, not a mystery, but the band structures of PC. It appears within either the high frequency range in the first band,[13–15] or in the second band.[16–19] To illustrate the first case, figure 1.2(a) shows the bands structure of a PC with a square lattice.[13] Two operating frequencies on the first acoustic branch, namely 6.15 Hz and 7.20 Hz, are chosen as examples. At 6.15 Hz, the EFC is centered at M point in the reciprocal space while the EFC for the wave in the background is centered at $\Gamma$ point, as shown in figure 1.2(b). A wave incident from the background is denoted in the first Brillouin zone by the $\mathbf{k}$ vector together with the group velocity $\mathbf{v}_g$. Within the first branch of the dispersion curves, the relationship $\mathbf{k} \cdot \mathbf{v}_g > 0$ holds on. So that the incident wave undergoes negative refraction at the interface between the background and the PC, as confirmed by the direction of group velocity vector $\mathbf{v}_g$ and shown by the label in figure 1.2(b). Similar behaviors arise for 7.2 Hz (see figure 1.2(c)). However, in this latter case, the wavenumber $k$ is smaller in the PC than it is in the background, which in return changes a little the achievements of the PC.

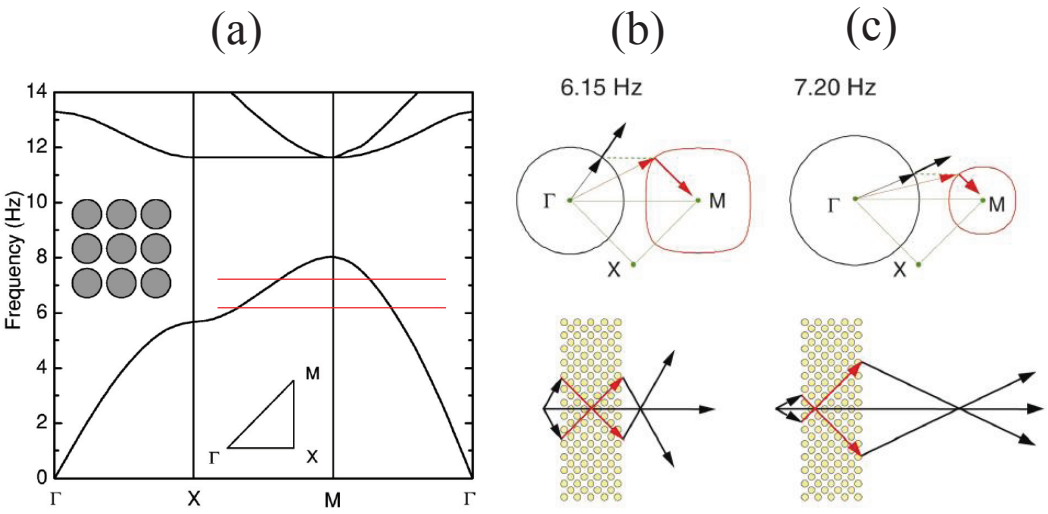


Figure 1.2: (a) Band structure of a PC. Two frequencies are chosen in the first branch at 6.15 Hz and 7.20 Hz. (b) The equal frequency contour at 6.15Hz for both the background medium (black line) and the PC (red line), and (c) the equal frequency contour at 7.20 Hz for both the background medium (black line) and the PC (red line).[13] The negative refraction lens is formed at the first branch through the relationship $\mathbf{k}\cdot\mathbf{v}_g > 0$.

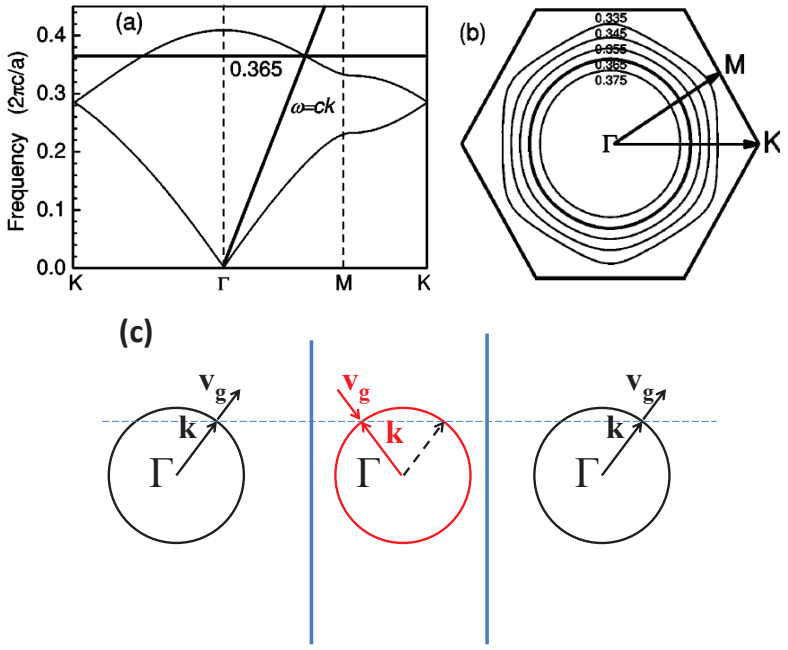


Figure 1.3: (a) Band structure of a PC, with $c$ the wave velocity of background medium. (b) Equal frequency contours at the second branch.[17] (c) Scheme of the wave vector and group velocity for an incident wave. The negative refraction lens is formed at the second branch through the relationship $\mathbf{k}\cdot\mathbf{v}_g < 0$.

To illustrate the second case of negative index, figure 1.3(a) shows the bands structure of another PC with the honeycomb lattice. The sound line, indicated

by the relationship $\omega = ck$, crosses the second branch at normalized frequency 0.365 ($2\pi c/a$). Figure 1.3(b) shows the EFCs at several frequencies. The modulus of $\mathbf{k}$ vector is almost constant whatever is the direction in the reciprocal space and therefore the EFC is close to a circle at 0.365 ($2\pi c/a$), indicating very few anisotropy at this frequency. Therefore, the EFCs both in the background and in the PC are considered as circles (see figure 1.3(c)). In this figure, an initial wave vector associated to the wave emitted by the source is drawn. The Snell's law predicts two potential wave vectors in the downstream medium, identified as solid line and dashed line starting from $\Gamma$ point, respectively. For frequency along the second branch, the relationship between $\mathbf{k}$ and $\mathbf{v}_g$ reads $\mathbf{k} \cdot \mathbf{v}_g < 0$ now. The dashed line gives the direction of the group velocity (associated to the flux of elastic energy) just in opposite direction to the wave incident from the background, which is not physically acceptable, so that only one wave vector indicated by the solid line is conserved. It is clear from the direction of the group velocity that the incident wave is negatively refracted.

It has been proved, both theoretically and experimentally, that a negative-index PC allows for the sub-wavelength focusing or imaging, by either of the geometries (first band or second band) described above.[13–22] To a certain extent, the resolution was beyond the diffraction limit, with the evanescent components gathered at the focus.[23–25] To further illustrate this, figure 1.4(a) shows a snapshot of the wave focusing through a negative-index PC at 530 KHz.[23] The transverse profile in figure 1.4(b) displays a resolution at the focus beyond the diffraction limit, at the peak value of the horizontal profile along the central layer in figure 1.4(c). This is a clear evidence that the superfocusing effect has been achieved.

To answer the question why the superfocusing effect was achieved in the work,[23] whereas it was not observed in systems featuring an effective refraction index equal to $-1$,[17,18] the bound modes have been calculated, as shown in figures 1.5(a) and 1.5(b). The bound modes are those bands that exit below the sound line (dash line in figure 1.5(a)) in the background medium. They correspond to leaky modes between the PC and background medium with the horizontal wavenumber being imaginary. These modes play the role of a real bridge transferring the information carried by the evanescent components to the near-field focus.[23] Therefore, they are essential the mechanism leading to the superlensing effect.

All these studies about the negative refraction and superfocusing of acoustic waves in a fluid (*i.e.*, longitudinally polarized) have inspired a series of works on both the negative refraction and the imaging or focusing of waves with other polarizations,[26–36] including some recent works about Lamb and Rayleigh waves in solids. However, in contrast with the state of the art in the photonic crystals side,[37–39] the mechanism at the origin of the bound modes by evanescent component has not been fully explored yet for PCs in solid matrices.

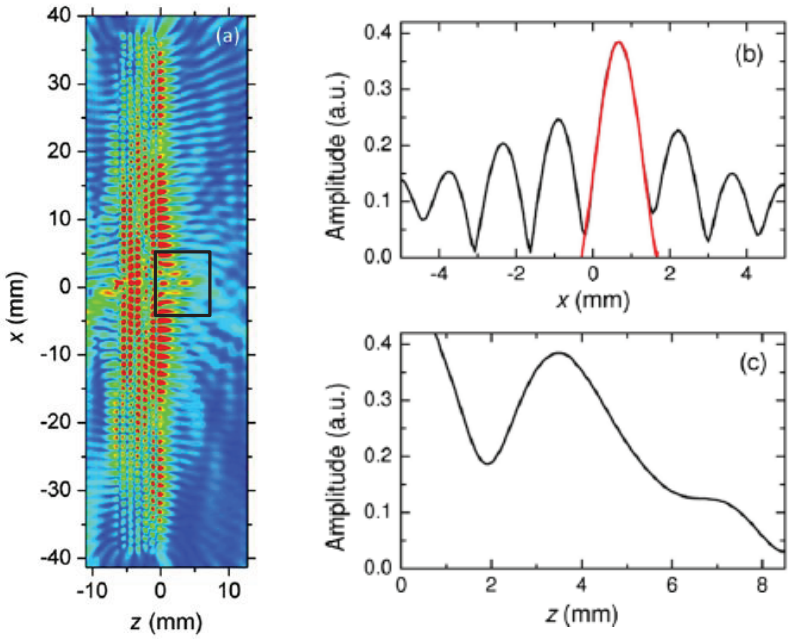


Figure 1.4: (a) Numerical superfocusing through negative refraction PC at 530KHz, (b) the transverse profile at the peak value, (c) the horizontal profile along the symmetric axis.[23]

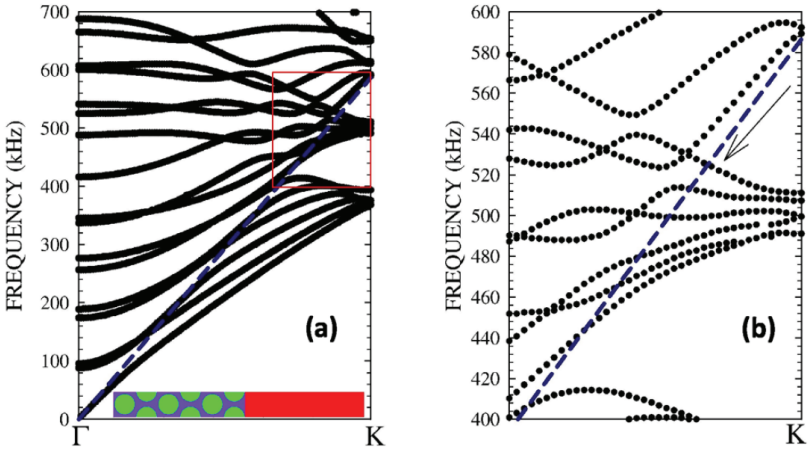


Figure 1.5: (a) Numerical investigation of the bound modes of a PC. The label indicates the used model while the dash line presents the sound line of background medium.(b) The zoom of the part in the box. The working frequency is 530 KHz, as shown in figure 1.4.[23]

The transverse profile at the peak value, when evanescent components are in-

cluded, can be estimated through[9]

$$|I(x)| = \left| \int_{-\omega/c}^{\omega/c} e^{ikx} dk + \left( \int_{-k_M}^{-\omega/c} + \int_{\omega/c}^{k_M} \right) e^{ikx} dk \right|^2, \quad k_M > \omega/c \tag{1.1}$$

where $I$ is the image intensity, $\omega$ is the angular frequency, $c$ is the velocity of background, $k$ is the transverse wavenumber, and $k_M$ is maximum value of $k$. In equation (1.1), not only the propagating components with $|k| < \omega/c$ but also the evanescent components with $|k| > \omega/c$ are integrated at the focus. Theoretically, in the perfect lens proposed by J. Pendry, the maximum wavenumber $k_M \to \infty$,[6] which is however not doable for PC based lenses since there is always a cut-off wavelength for $k_M$.[23,25]

### 1.2.2 Analysis of far-field superlensing focusing

The superlensing effect is considered to be limited to the near field because of the exponential decay of the evanescent components.[10,40] To illustrate this, figure 1.6(a) schematically depicts the changes in the amplitude of evanescent waves from the source to the far field behind a *conventional* superlens.[10] The amplitude is almost zero after one wavelength behind the lens. To overcome this barrier and get the super-solution effect in the far field, the so-called *far-field superlens* was proposed as a alternative to the conventional superlens.[10] As showed in figure 1.6(b), for the negative-index far-field superlens there is a one-to-one relationship between the near-field and far-field angular spectra: $k' = k + 2\pi/d \times p$, where $k$ is the incident transverse wavenubmer, $k'$ is the transmitted transverse wavenumber, and $p$ is the diffraction order. Clearly, the far-field superlens is not limited to single-mode analysis, as it is the case for the conventional superlens, and it has been established already for electromagnetic waves in photonic crystals based lenses for optics.[11,12] *In the view of angular momentum, the far-field superlensing applies not only to optics but also to acoustics, once the conditions are satisfied.* The effect has been numerically predicted for the image of a point source through a negative-index PC.[41] However, the experimental verification and the underlying mechanism are still missing.

In terms of imaging or focusing through the negative refraction, either in the near field or in the far field, more attention has been paid to recover the information of a point source. In return these works are more about the wave imaging than about focusing, although a clear distinguishing between these effects is generally not made.

Negative-index PC, involving either the near-field or the far-field focusing, works at the high frequency in the first acoustic or the second branch. The positive-index PC, on the other hand, provides a practical way to focus acoustic waves at low

frequency in the first acoustic branch.

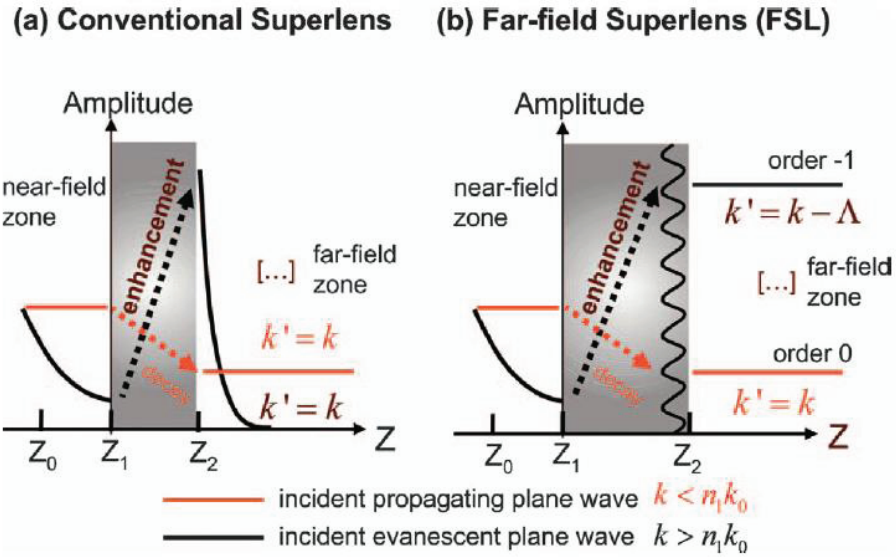


Figure 1.6: Transmitted properties of (a) conventional superlens versus (b) the far-field superlens. The conventional lens has enhanced the incident evanescent component. However the amplitude decreases quickly at the near field. The far-field superlens can also recover the incident evanescent component. Meanwhile, the evanescent component to propagating mode at the boundary through the angular spectrum. [10]

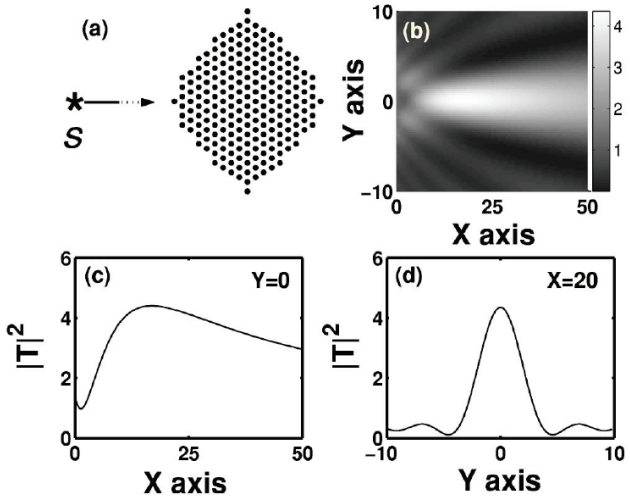


Figure 1.7: Acoustic focusing[42] by using a shaped PC featuring a positive index at the low frequencies: (a) scheme of geometric lens, (b) two-dimensional distribution of the measured intensity $|T|^2$, (c) the intensity along the symmetric axis, and (d) the intensity along the transverse axis at the peak value in (c).

## 1.3 Positive-index focusing of phononic crystal

Attention has been paid to the focusing by PCs based acoustical lenses featuring a positive index since almost the beginning of the PC topic emerges. In the early studies, the lenses were composed of uniform PC and were shaped in different geometries to make them behave similarly as optical lenses.[42–46] Figure 1.7(a) shows the drawing of an acoustical lens with a parabolic surface shape, while figure 1.7(b) shows the intensity distribution behind the lens.[42] A focusing zone is clearly observable behind the lens and it focal distance can be identified by the peak value on the horizontal profile of intensity along $y = 0$, as shown in figure 1.7(c). Figure 1.7(d) shows the transverse profile of intensity at the peak value. As it is the case with the geometric optical lenses, these acoustic lenses cannot gather the fine information carried by the evanescent components.

The GRIN PC has the advantage over these former PC based prototypes to be a flat lens, providing therefore more freedom to control the wave propagation. GRIN PCs, analogously to graded metamaterials or photonic crystals,[47–57] allow waves propagating in themselves to converge, to collimate or to diverge . Although certain GRIN PCs featured a negative index,[58,59] most of the studies involved heterostructures with the positive index, i.e., they worked within the first acoustical band.[60–71] The concept of the GRIN PC, was chiefly proposed to manipulate elastic waves at low frequencies, in the first band. To now GRIN PCs have been developed in either the Cartesian, cylindrical or spherical coordinates systems, such as Eaton lens and Luneburg lenes.[68,72,73] In this work however, we restricted ourselves to study the focusing of elastic waves or the imaging via the flat GRIN PC in Cartesian coordinates system.[61]

As an illustration, figure 1.8(a) shows the drawing of an optical lens featuring a refractive index with a hyperbolic secant profile along the $y$ axis, together with the light trajectories in it.[61] To get a gradual refractive index, the discrete GRIN PC is formed by modifying either the radii of inclusions (figure 1.8(b)) or the elastic constants (figure 1.8(c)) along the transverse direction. The reasons of such a choice are well explained by the first bands of PCs for different radii of inclusions (figure 1.9(a)) or different elastic constants (figure 1.9(b)). These first bands shift gradually with the alteration of inclusions, which in return results an effective refractive index at a given frequency accordingly to the radii or the materials the inclusions are made of. Therefore the GRIN PC is supposed to feature a graded refractive index, with a profile that can be finely tune accordingly to the design.

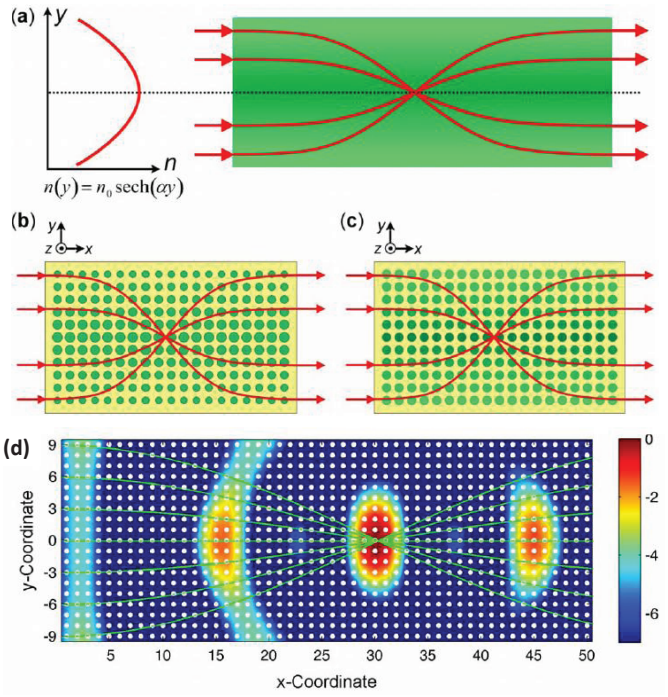


Figure 1.8: (a) A gradient-index medium featuring a hyperbolic secant profile along the transverse direction. A GRIN PC which performs as the GRIN lens is realized by modifying(b) either the radii of cylinders or (c) the elastic constant.[61]

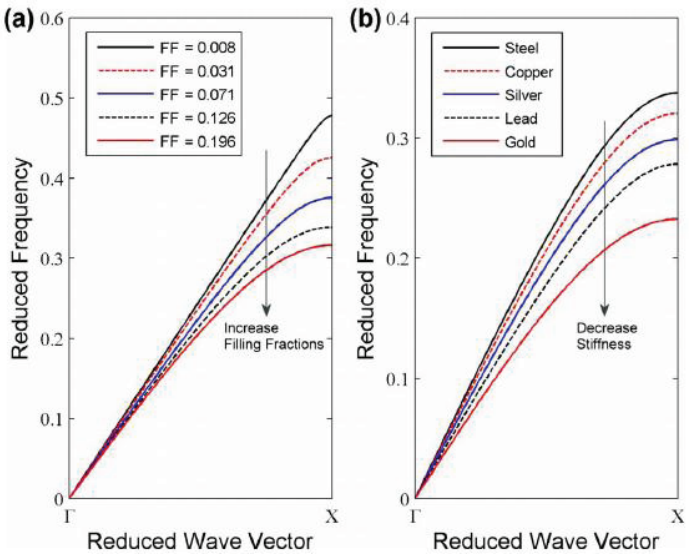


Figure 1.9: Band diagrams of the first shear-vertical wave along the $\Gamma X$ orientation. (a) By modifying the radii of the inclusion keeping the same material, (b) by modifying the material of the inclusion keeping the geometry the same.[61]

Figure 1.8(d) shows the subwavelength focusing at low frequency which manifests itself by the large amplitude of the displacements at the focus. Similar results

can be observed within a broad range of frequencies, which is different from the negative-index flat lenses. These advantages can be well explained by the working band of GRIN PC. The first band generally ensures high transmission of waves for the small impendence mismatch between lens and background, so that energy can be well gathered. Secondly, a given GRIN PC can exhibit similar profile of refractive index within the first band, which makes lens have similar function within this broad range of frequencies.

The focusing behavior of different waves inside the GRIN PC, including the numerical investigation $A_0$ mode, has been studied.[60–67] These research works, as well as those came later, allowed observing the subwavelength focusing both inside and outside the GIRN PC. However, they mainly were dealing with acoustic waves in fluids.[68,69] To now, the focusing of $A_0$ mode and of the so-called "spoof surface-acoustic-waves" (SSAW) has been verified experimentally.[70,71,74–77]

In the long-wavelength regime, the PC is considered to have an *effective* refractive index. This effective index serves as a basis to design the GRIN PC. However, it should be noticed, that the theory predicts the focusing to occur at a different distance than deduced from the numerical simulations.[61] The disagreement can be large at the short-wavelength regime where the definition of effective refraction index losses its efficiency. Certain physical explanations were given, including the homogenization and anisotropy of GRIN PC.[61,66] However, no quantitative analysis has been done to date. Actually, studies about the mirage effect of graded photonic crystal, gave the opportunity to investigate the anisotropy of photonic crystal. It has been qualitatively shown that the modulus of EFC has an important influence on the behavior of the optical waves.[49] However, few studies dealing with the propagation of acoustic waves in a GRIN PC are available.

# Chapter 2

# Subwavelength Focalization of $A_0$ mode inside GRIN PC

## 2.1 Introduction

Using PC to focalize elastic waves with frequencies in the first branch of the Brillouin zone where negative refraction effects are not involved, is possible if considering gradient index phononic crystals (GRIN PCs).[60–66,68–71,74–77] These two-dimensional (2D) systems are engineered with a gradual variation of their constitutive parameters (e.g., filling factors, geometry of the inclusions or material properties) along one direction. As a result, they feature a sound velocity gradient along that direction making it possible the focalization of an incident wave. Actually, when an acoustic beam propagates through a 2D GRIN PC, it encounters redirection at every virtual interface between layers, resulting in successive reorientations of the acoustic beam inside the structure. Thus, by gradually modulating the parameters of a GRIN PC, one may create a focusing trajectory for the acoustic waves.[61–64,66,68–71,74–77] In principle, this trajectory can be analytically calculated, at least for some forms of the gradient.

However, deviation between the focal distance predicted by the theory and that derived from numerical simulations may be sometime significant, even in the homogenization frequency range.[61–64,66,68–71,74–76] There are several reasons for this. First, the actual 2D acoustic lenses feature discretized indices which may be imperfectly represented by a continuous gradient. However, this is probably not the most relevant reason since small deviations of a few percent were observed for wavelength only five times larger than the period.[61–64,66,68–71,74–76] The observed disagreement between theory and numerical simulations can be explained in a larger extent by the overall shape of the equi-frequency contours (EFCs).[77] Actually, in PCs with large filling factors the EFCs may depart from a circle, even at low frequency, and

analyzing the trajectories in terms of an effective index may not be relevant.

Instead, the effects of anisotropy are better described by considering both the group velocity and the **k** vector as local parameters.[49] Based on the same idea, Hamiltonian optics approach has been recently proposed to study light propagation in a graded photonic crystals in the short-wavelength regime.[55,57] However, up to now there is only few theoretical works enabling for a quantitative analysis of the ray trajectory in the homogenization range. This is the reason why we address this issue in this chapter where we describe a method that allows analyzing the trajectory of an elastic beam propagating in a GRIN PC. Then we use this physical model to analyze the focusing properties of 2D acoustical lenses where the velocity gradient is realized either by gradually modifying the lattice spacing or by varying the size of the air inclusions along one direction of the PC, as published in the Ref [77].We present then an experimental investigation of the focusing of the zero order anti-symmetric Lamb waves propagating through air/silicon GRIN PCs with either of the two geometries and we compare their efficiency in focusing flexural Lamb waves at sub-wavelength.

## 2.2 Band structures of phononic crystal

### 2.2.1 Description of physical model

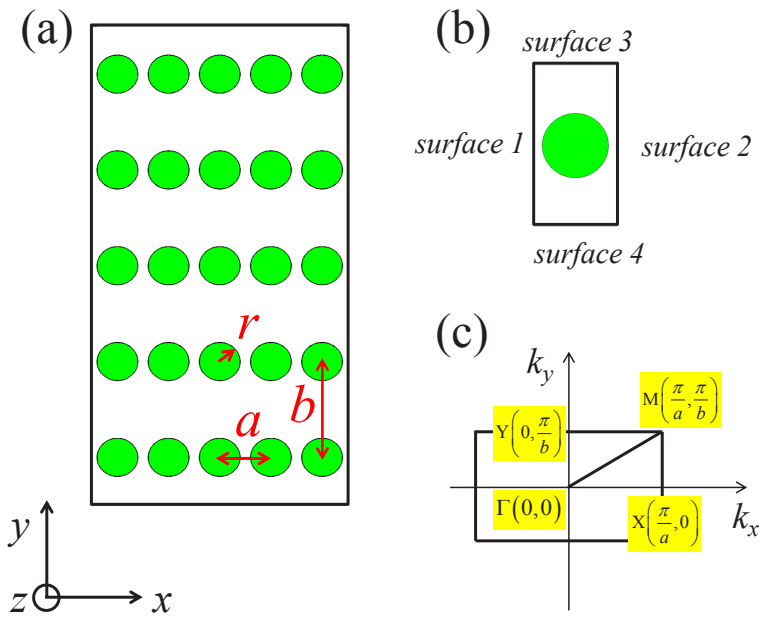


Figure 2.1: Scheme of (a) PC in rectangular lattice in the direct space, (b) unit cell, and (c) the corresponding **k** vector in the reciprocal space.

The PC was obtained by piercing air holes of radius $r$ through a silicon plate of thickness $h$. Figure 2.1(a) shows a scheme of air holes arranged in a rectangular lattice, with $a$ the periodic constant along $x$-axis and $b$ along $y$-axis. The aspect ratio is defined as $b/a$ while the filling ratio is determined by $ff = \pi r^2/ab$. Silicon has its elastic constants $C_{11} = 165.6$ GPa, $C_{12} = 63.9$ GPa, $C_{44} = 79.5$ GPa, and its mass density $\rho = 2331$ kg/m$^3$. The $x$, $y$ and $z$ directions are parallel to the crystallographic directions $< 100 >$, $< 010 >$ and $< 001 >$, respectively. Figure 2.1(b) shows the unit cell of a PC with lateral surfaces identified as surfaces 1-4, respectively. Figure 2.1(c) shows the first Brillouin zone with wavenumber $k_x$ belonging to $[-\pi/a,\ \pi/a]$ along ΓX direction while wavenumber $k_y$ belonging to $[-\pi/b,\ \pi/b]$ along ΓY direction.

The elastic medium obeys the constitutive equation[78,79]

$$\mathbf{T} = \mathbf{C} : \mathbf{S}, \tag{2.1}$$

where $\mathbf{T}$ is the stress tensor, $\mathbf{C}$ is the elastic tensor, and $\mathbf{S}$ is the strain tensor. The strain tensor is related to displacement field $\mathbf{u}$ by equations

$$\mathbf{S} = \nabla_{\mathbf{s}}\mathbf{u}, \tag{2.2}$$

where $\nabla$ stands for the *nabla* operator. At the same time, the dynamic equations are

$$\nabla \cdot \mathbf{T} = \frac{\partial^2 \mathbf{u}}{\partial t^2}, \tag{2.3}$$

where $t$ is time, and $\nabla\cdot$ is the *divergence* operator. Equations (2.1)-(2.3) are written in a tensor form. Their expansions can be derived for silicon of cubic symmetry to be

$$\begin{bmatrix} T_x \\ T_y \\ T_z \\ T_{yz} \\ T_{xz} \\ T_{zy} \end{bmatrix} = \begin{bmatrix} C_{11} & C_{12} & C_{12} & 0 & 0 & 0 \\ C_{12} & C_{11} & C_{12} & 0 & 0 & 0 \\ C_{12} & C_{12} & C_{11} & 0 & 0 & 0 \\ 0 & 0 & 0 & C_{44} & 0 & 0 \\ 0 & 0 & 0 & 0 & C_{44} & 0 \\ 0 & 0 & 0 & 0 & 0 & C_{44} \end{bmatrix} \begin{bmatrix} S_x \\ S_y \\ S_z \\ S_{yz} \\ S_{xz} \\ S_{zy} \end{bmatrix}, \tag{2.4}$$

$$\begin{bmatrix} S_x \\ S_y \\ S_z \\ S_{yz} \\ S_{xz} \\ S_{zy} \end{bmatrix} = \begin{bmatrix} \partial u_x/\partial x \\ \partial u_y/\partial y \\ \partial u_z/\partial z \\ \partial u_y/\partial z + \partial u_z/\partial y \\ \partial u_x/\partial z + \partial u_z/\partial x \\ \partial u_x/\partial y + \partial u_y/\partial x \end{bmatrix}, \tag{2.5}$$

$$\begin{aligned} \partial T_x/\partial x + \partial T_{xy}/\partial y + \partial T_{xz}/\partial z &= \partial^2 u_x/\partial t^2 \\ \partial T_{xy}/\partial x + \partial T_y/\partial y + \partial T_{yz}/\partial z &= \partial^2 u_y/\partial t^2 \\ \partial T_{xz}/\partial x + \partial T_{yz}/\partial y + \partial T_z/\partial z &= \partial^2 u_z/\partial t^2 \end{aligned} , \tag{2.6}$$

Displacement field in the PC satisfies the Bloch theorem[1]

$$u_j(\mathbf{r}) = u_{j\mathbf{k}}(\mathbf{r}) e^{i\mathbf{k}\cdot\mathbf{r}}, \quad j = x, y, z \tag{2.7}$$

where $\mathbf{r}$ is the position, and $\mathbf{k}$ is the wave number vector ($k_x,\ k_y$) as shown in figure 2.1(c). $u_{j\mathbf{k}}$ has the same periodicity as the structure. Due to Bloch theorem, it is sufficient to calculate Band structures by using just one unit of PC as shown in figure 2.1(b), with Bloch theorem or periodic conditions applied on the lateral surfaces 1-4.

Meanwhile, it is necessary to apply the free condition on any surface open to air or vacuum. The stress $\mathbf{T}$, and the unit normal vector $\mathbf{n}$ on such a surface obey the relationship

$$\mathbf{T} \cdot \mathbf{n} = 0. \tag{2.8}$$

### 2.2.2 Bands calculation by finite element method

FEM is recognized as being one of the most powerful methods to solve the above three-dimensional (3D) problem. It is convenient to modify the shape of inclusions or unit cell in combination with commercial softwares. Details of FEM can be found in many known references.[79–81] So that it will not be repeated here. We used the *eignemode* module in *structures* in Comsol Multiphysics to solve the 3D problem. Wave motion equations, as described by equations (2.4)-(2.6), are initialized for elastic medium in the software while the user just needs to put in the elastic constants. Among the two groups of boundary conditions, the free conditions are set as the default in the software. It needs only set up the periodic condition on the lateral surfaces. The Bloch theorem is derived as[79,80]

$$\begin{aligned} u_j^2 &= u_j^1 e^{ik_x a} \\ u_j^4 &= u_j^3 e^{ik_y b} \end{aligned} , \quad j = x, y, z \tag{2.9}$$

The subscripts 1, 2, 3, 4 are for the surfaces 1, 2, 3, and 4, respectively. By implanting the Bloch theorem as periodic condition on the lateral sides, it becomes possible to calculate the eigenfrequency and eigenmode for any wave vector in the first Brillouin zone and solve the set of equations[81]

$$\left[K(\mathbf{k}) - \omega^2(\mathbf{k}) M(\mathbf{k})\right] \mathbf{u}(\mathbf{r}) = 0, \tag{2.10}$$

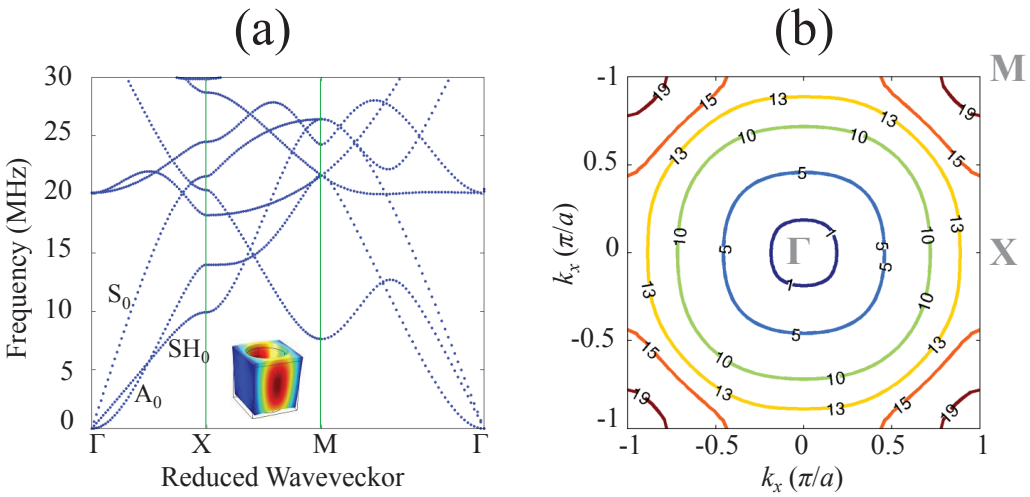


Figure 2.2: (a) Band-gap structures of air/silicon PC with unit width $a = b = 100m$, radius of air hole $r = 40\mu m$, and plate thickness $h = 110\mu m$. (b) Equal frequency contours of A0 mode in the first Brillouin

where $K$ is the reduced stiffness matrix; $M$ is the reduced mass matrix.

### 2.2.3 Bands structures and equal frequency contours

The eigenfrequencies are usually obtained for wave vectors along the primary directions ΓX, XM, and ΓM, and allow in turn to calculate the band structures of the PC within the first Brillouin zone. Figure 2.2(a) shows the band structures for a PC with $a = 100$ $\mu$m, $b = 100$ $\mu$m, $r = 40$ $\mu$m, and $h = 110$ $\mu$m. For comparison, similar results can be found[66] although with the value $h = 50$ $\mu$m. Same results were repeated by FEM, which helped ensure the validity of our model. The lowest order symmetric ($S_0$) mode wave, the lowest order antisymmetric ($A_0$) mode wave, and the lowest order shear horizontal ($SH_0$) mode wave were identified in figure 2.2(a) according to their eigenmodes, respectively. The inset of figure 2.2(a) shows the eigenmode of $A_0$ mode, with its displacement polarized along the $x$ and $z$ axis. However, in this work, we considered $A_0$ mode only.

Band structures can be calculated along any direction in the first Brillouin zone. The bands for a given mode, together with the corresponding **k** vectors, give rise to a 2D mode surface. At a given frequency, it corresponds to a 2D equal frequency contour (EFC, or isofrequency contour) in ($k_x$, $k_y$) plane. Figure 2.2(b) shows the EFCs for $A_0$ mode at several frequencies. As the frequency increases, the modulus of EFCs evolves gradually from a small quasi-circular shape centered at Γ point at 1 MHz to a large quasi-circle almost until the edge of the first Brillouin zone at 13 MHz. After that, for frequencies larger than 13 MHz the modulus gets centered at M point with decreasing radius. However, at close sight, the EFC shape is not exactly

a circle for frequencies below 13 MHz. The mismatch may be different depending on the direction within the first Brillouin zone. To account for this relationship, we defined the ratio $\eta(\theta) = (k - k_{\Gamma X})/k_{\Gamma X}$ with $\theta$ the angle between wave vector $\mathbf{k}$ and ΓX. Along ΓM, $\eta$ takes the values 0.066, 0.068, 0.036, 0.024 for 1 MHz, 5 MHz, 10 MHz, and 13 MHz respectively.

Having introduced the basic characteristics of PC, attention is turned now to the wave behaviors in a GRIN PC.

## 2.3 Beam paths of waves in GRIN PC

### 2.3.1 Designs of GRIN PCs

Generally, as long as the wavelength is much larger than the size of unit cell, the medium can be considered as homogeneous and the group velocity can be simply derived from the derivative of the corresponding dispersion curve at any location in the GRIN PC. This allows in turn defining an effective index $n_{eff}$ as being the average of the index along ΓX and along ΓM directions[61]

$$\begin{aligned} n_{eff} &= \frac{n_{\Gamma X} + n_{\Gamma M}}{2}, \\ n_{\Gamma X} = v_B/v_{\Gamma X}, &\quad n_{\Gamma M} = v_B/v_{\Gamma M}. \end{aligned} \tag{2.11}$$

$v_{\Gamma X}$ and $v_{\Gamma M}$ are the group velocity along ΓX and ΓM. $v_B$ is the group velocity in the background medium. Equation (2.11) clearly shows that the refraction index is dispersive.

#### Parabolic profile

GRIN PCs can be designed to have various profiles of refractive index. However, deriving the trajectory without any approximation does not hold for all of them. Following Wu *et al.*, numerical simulations of a GRIN PC were performed on a silicon plate with a thickness $h = 110$ $\mu$m with periodic constant $a = 100$ $\mu$m.[66] The scheme was shown in figure 2.3(a).[71] The lens was fabricated in such a way that its refractive index $n_{eff}$ has a transverse profile close to a parabola

$$n^2(y) = n_0^2(1 - \delta^2 y^2) \tag{2.12}$$

at 7 MHz, where $n_0 = 1.247$ and $\delta = 0.011a^{-1}$. Figure 2.3(b) shows the $A_0$ bands for each horizontal inclusion layer in the sample with clear drop of the band at $ff = 0.726$. Figure 2.3(c) shows the EFCs at 7 MHz. The EFC along the central

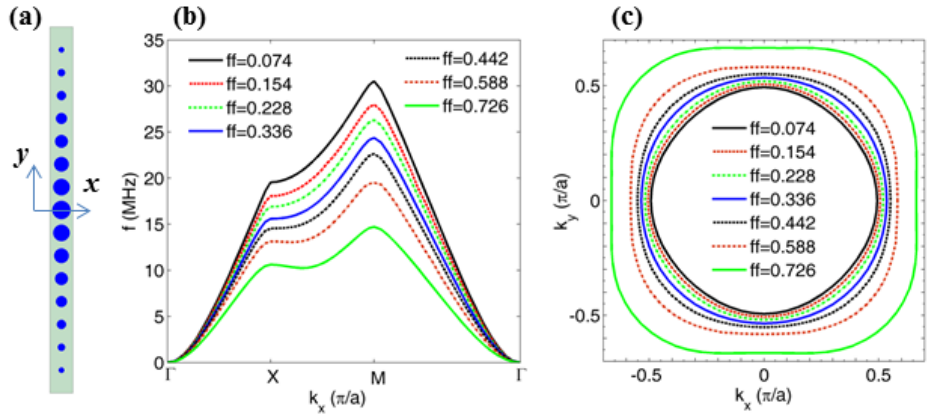


Figure 2.3: (a) Scheme of the GRIN PC with wave propagating along the $x$-direction. (b) Dispersion curves of the $A_0$ mode wave for the air/silicon phononic slab with different filling ratios. (c) Equal frequency contours of $A_0$ mode at 7 MHz.

layer of the sample is far from being a circle, indicating a strong anisotropy.

Numerical simulations and experiment have been done to find the field distribution of wave focusing in the GRIN PC at 7 MHz. We will describe main features of the experiment later in the section 2.5 in this chapter. Figure 2.4 shows the maxima of (a) simulated and (b) experimental $u_z$ in a GRIN PC featuring 35 columns as shown in figure 2.4(c). For both simulation and experiment, we found a focusing zone well located at the center of lens with a *gain factor* (*i.e.*, the ratio between amplitude at the focus and that of the incident wave) about 3.8. However, the experiment demonstrates an oscillatory trajectory to have another peak (slightly smaller than the first one) while it is not the same case for the simulation. This is clearly shown in figure 2.5(a) by the horizontal profile along the central layer, in which there is a small distance between adjacent peaks. Simulation and experiment give also a shift between transverse profiles observed at their first peaks as found in figure 2.5(b).

Such disagreements can find their origin in the fabrication process: actually the largest holes had larger diameters than expected. Besides, the large holes may have their radii on one side of slab larger than on the other side. As a consequence, both $n_0$ and $\delta$ may be larger than expected, and the focal distance is shorter than calculated. However, such a qualitative analysis cannot further reveal the focusing features of the lens for several reasons. First, we set the refractive index have a parabolic profile which, in theory, leads to aberrations of the ray trajectories. Secondly, GRIN PCs are discrete structures and the influence of discreteness can hardly be analysed precisely. Thirdly, the EFCs depart from being circular in some rows of the system. The effective refractive index can be dependent both on the local position and on the direction in the Brillouin zone, as shown in figure 2.3(c). Therefore equation (2.11) may not keep the same efficiency at describing the index

and in turn at describing the trajectories at any position in the GRIN PC or along any direction.

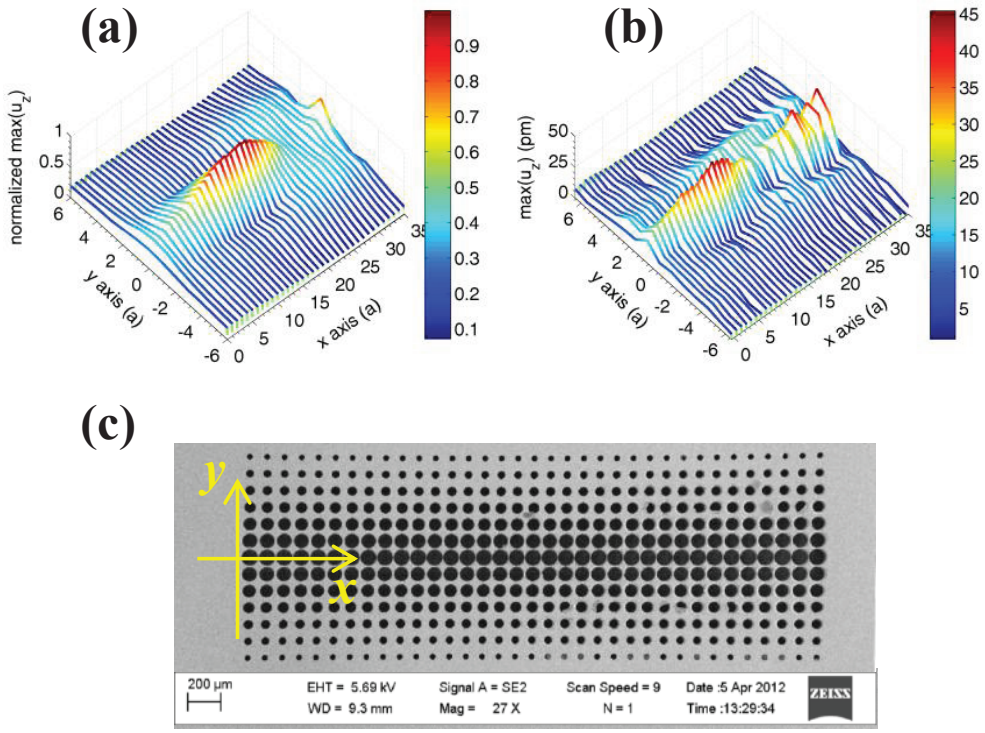


Figure 2.4: (a) Simulated maxima and (b) experimental maxima of $u_z$ on the top surface of air/silicon slab at 7 MHz. (c) Image of surface of experimental sample.

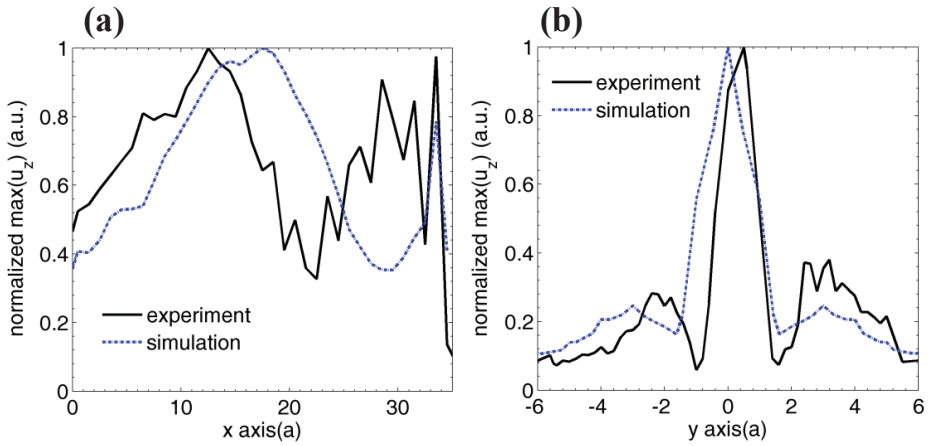


Figure 2.5: (a) Experimental (solid line) and numerical (dashed line) of maxima of $u_z$ along the acoustic symmetric axis. (b) Experimental (solid line, $x = 12.5a$) and numerical (dashed line, $x = 17a$) of maxima of $u_z$ along the $y$ axis.

Finding the primary factor to design the GRIN PC requires a subtle treatment of the above physical conditions. This is the reason why we have continued our

study with the case of the hyperbolic secant profile of which a parabolic profile is the first-order Taylor series expansion. Actually, the hyperbolic secant profile allows for an exact determination of the acoustical rays.[82]

### Hyperbolic secant profile

GRIN PCs were designed to have an refraction index obeying a transverse hyperbolic secant profile, which can be formally written as[66]

$$n^2(y) = n_0^2 \mathrm{sech}^2(\delta y), \tag{2.13}$$

where $n_0$ is the index along $x$-axis, at the center of the lens and $\delta$ the gradient parameter. A lens whose index features a hyperbolic secant profile is free of aberration, *i.e.*, any ray normally incident on the lens converges to a single point on the axis, at the focal length $f_l$, which depends only on $\delta$ through

$$f_l = \pi/2\delta. \tag{2.14}$$

The derivation of equation (2.14) is found in the Appendix A together with the ABCD law to calculate the ray trajectories.[82] The gradient index along $y$-axis obeying equation (2.13) may result from the gradual variation of the filling factor. This can be achieved by modulating either the diameter of the cylindrical air inclusions or the distance separating two consecutive inclusions while keeping uniform their diameter. In the former case, the GRIN PC has a square lattice whereas the unit cell is rectangular in the latter case. In what follows, the frequency was supposed to be 5 MHz. All the results are for this frequency unless specified otherwise.

To achieve an effective index with a hyperbolic secant profile, length $b$ was imposed to gradually vary along $y$-axis, whereas both parameters $a$ and $r$ kept constant values. This was equivalent to vary both the aspect ratio $b/a$ and the filling factor along $y$-axis. The result for frequencies along the first branch is shown in figure 2.6 for different values of the ratio $b/a$ in between 1 and 2.09.

In all the calculations the size of the unit cell along $x$ axis and the thickness of the plate were $a = 100$ $\mu$m and $h = 110$ $\mu$m respectively. The radius of the holes was kept constant to $r = 40$ $\mu$m. However, one should notice that, strictly speaking, GRIN PCs are not 2D phononic crystals since they do not exhibit exact periodicity along $y$-axis. Nevertheless, the dispersion properties can be computed by considering as many reduced Brillouin zone as the number of discrete values taken by the parameter $b$. All these reduced Brillouin zones extend over $[-\pi/a,\ \pi/a]$ along $\Gamma$X but the component $k_y$ takes values in intervals $[-\pi/b,\ \pi/b]$ that are different according to the value of $b$ (see the inset in figure 2.6).

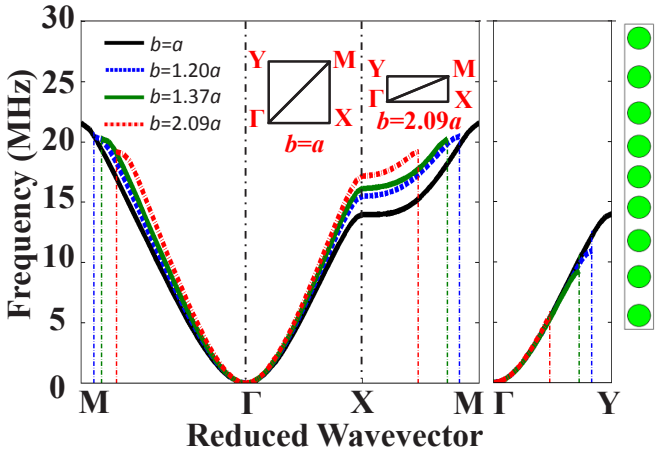


Figure 2.6: First dispersion band of Lamb mode $A_0$ propagating in a Si/air phononic plate with a rectangular lattice for different sizes of the unit cell along $y$-axis

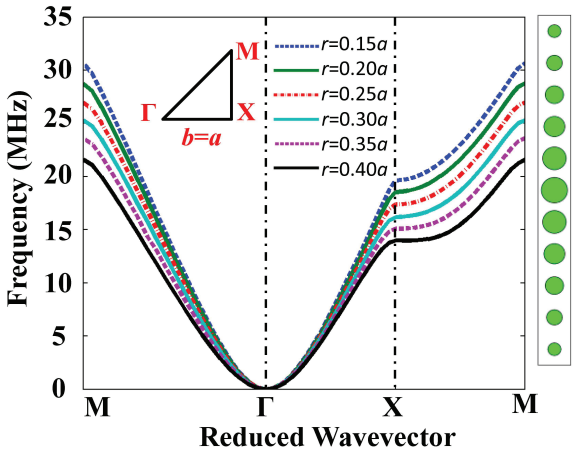


Figure 2.7: First dispersion band of Lamb mode $A_0$ propagating in a Si/air phononic plate with a square lattice for different values of the air inclusions radius

The squared array was deduced from the preceding case by setting $a = b$. In that case, ΓX and XM have identical lengths in the reciprocal space and one obtains a dispersion curve for each value of *ff* (figure 2.7). The hyperbolic secant profile was achieved by gradually varying the radius $r$ of the holes, or equivalently, the filling factor *ff*. Note that the different geometrical parameters were fixed in such a way that they allow for further comparisons between the two symmetries and that they remain compatible with elaboration and experimental constraints. Actually, the parameters of the lenses namely $n_0 = 1.32$ and $\delta = 0.088\ a^{-1}$ turned out to represent the best compromise in equation (2.13). However, anisotropy along some rows of inclusions may occur and consequently the EFCs may depart from being circular along these rows. In that case, equation (2.13) fails to describe the actual index profile since it does not account for this anisotropy. Indeed, the

anisotropy coefficient $\eta(\theta)$ is maximum for $\theta = \pi/4$ where, depending on the filling ratio, it takes a value in between $-0.03$ ($r = 0.2a$) and $0.07$ ($r = 0.4a$). As for the rectangular lattice, the anisotropy coefficient has a maximum at an angle that depends on the filling ratio but it remains always below 0.09.

*Still, as shown below, equation (2.13) is not factored in the calculation of the ray trajectories and it was solely used to design both lenses.*

### 2.3.2 Beam path calculations

To calculate the ray trajectory within the GRIN PC of an elastic beam normally incident on the lens, $\varphi$ was defined as being the angle between the group velocity $\mathbf{v}_g$ (tangent to the trajectory) and $x$-axis (figures 2.8(a) and 2.8(c)). The filling factor varying from one horizontal layer to the next, one must compute the EFC in each layer, as depicted in figure 2.8(b). Because of Snell's law, which states that the component $k_x$ is conserved across the interface between two consecutive layers, the initial $\mathbf{k}$ vector tilts gradually as the wave propagates in the medium, from the horizontal direction to a maximum angle at the mid layer. In the general case, the EFCs are not circular[66,71] and the $\mathbf{k}$ vector makes an angle $\theta$ with respect to $x$ axis which is not equal to $\varphi$ (figure 2.8(c)).

To account for this anisotropy, we state that the modulus of the $\mathbf{k}$ vector along a given row of inclusions located at position $y$, may be written as

$$k(y,\theta) = k_{\Gamma X}(y)p(y,\theta), \tag{2.15}$$

where $k_{\Gamma X}(y)$ is the $\mathbf{k}$ vector along $\Gamma$X at position $y$, and $p(y,\theta)$ is a function whose value deviates all the more from unity as the EFC departs from being circular.

The components of the wave vector $\mathbf{k}$ along $x$ and $y$ directions are given by

$$\begin{array}{l} k_x = k(y,\theta)\cos(\theta) \\ k_y = k(y,\theta)\sin(\theta) \end{array} . \tag{2.16}$$

To account for the effect of the local anisotropy, one must relate angles $\varphi$ and $\theta$. To this end, it is sufficient to observe that the direction vector to the tangent to the EFC is $(\frac{\partial k_x}{\partial \theta}, \frac{\partial k_y}{\partial \theta})$; the group velocity, defined by $\mathbf{v}_g = \nabla_k \omega(\mathbf{k})$, is normal to this tangent and points in the direction given by a vector whose components are $(\frac{\partial k_y}{\partial \theta}, -\frac{\partial k_x}{\partial \theta})$. Hence, the relationship between angles $\varphi$ and $\theta$ reads:

$$\tan(\varphi) = -\frac{\partial k_x}{\partial \theta}\left(\frac{\partial k_y}{\partial \theta}\right)^{-1}. \tag{2.17}$$

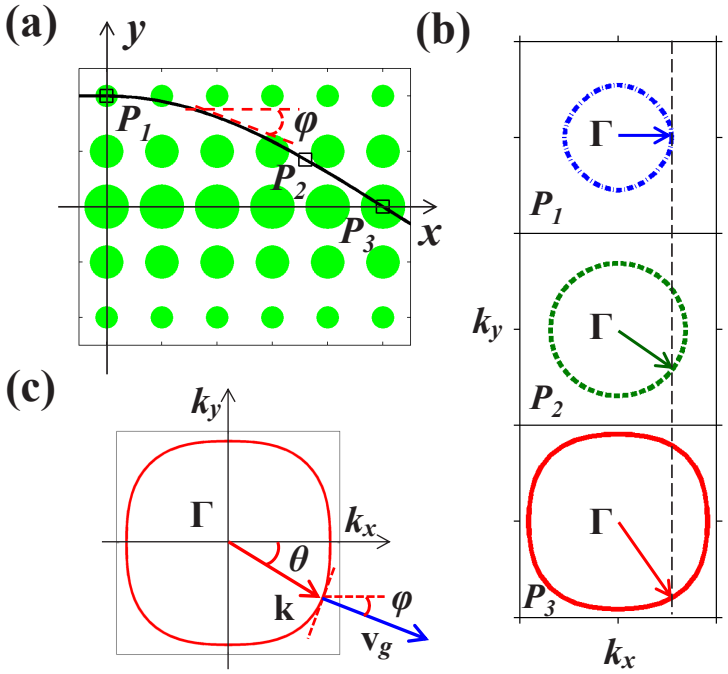


Figure 2.8: (a) Ray trajectory in a simplified GRIN PC made of five layers. $P_1$, $P_2$ and $P_3$ indicate three different positions along the ray trajectory and $\varphi$ is the angle between the tangent to the ray trajectory and $x$ axis; (b) the $\mathbf{k}$ vector gradually tilts from being horizontal at $P_1$ to a direction with an angle $\theta$ which depends on $x$, at $P_3$. The tangential component $k_x$ is conserved across the interface as shown by the location dependent EFCs; (c) $\mathbf{k}$ vector in a typical EFC with group velocity $\mathbf{v}_g$ normal to the EFC. The above representation is general and applies to any other ray trajectory in the lens.

In the direct space, $\mathbf{v}_g$ is tangent to the trajectory and therefore:

$$\tan(\varphi) = \frac{\mathrm{d}y(x)}{\mathrm{d}x}. \tag{2.18}$$

In the long wavelength limit, the value at $x = 0$ of the $x$-component of the wave vector varies continuously along $y$ axis according to equation (2.13). Moreover, as a consequence of the Snell's law, the component $k_x$ keeps constant value all along the acoustical ray that originates at position ($x = 0$, $y$), which translates into:

$$k_x = k_x^0(y). \tag{2.19}$$

Finally, an iterative procedure is used to derive the ray path from equations (2.15)-(2.19). Actually, for a given value of $y$ and at each position along $x$ axis, the angle $\theta$ was derived from equation (2.16) after setting $k_x^0(y)$ to an initial value, allowing in turn computing the slope $\varphi$ using equation (2.17), from which the trajectory $y(x)$ is obtained by numerically integrating equation (2.18).

To complete this procedure for both symmetries that we have considered, one

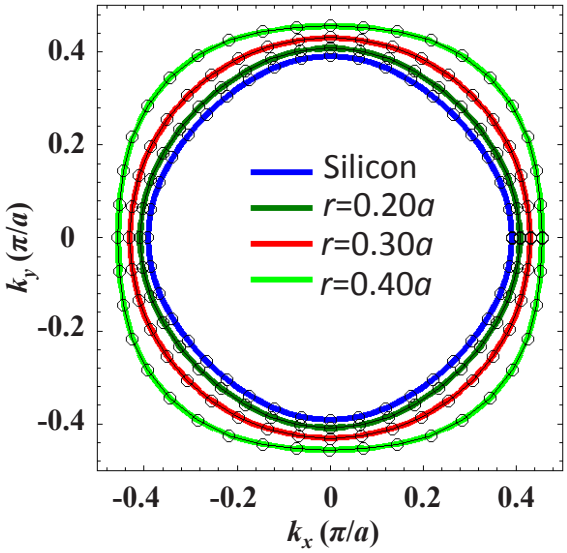


Figure 2.9: EFCs at 5 MHz (solid lines) and the corresponding fits derived from equation (2.20) (circular markers) for a PC with the square symmetry and for different sizes of the air holes.

must make assumptions on the form of the function $p(y, \theta)$ appearing in equation (2.15).

### Square lattice

In order to well reflect the anisotropy of the square lattice, the function $p(y, \theta)$ must account both for any departure from the circular shape of the EFC and for the four-fold axis characterizing this class of symmetry. Introducing the dimensionless coefficient $\alpha(y) = \frac{k_{\Gamma M} - k_{\Gamma X}}{k_{\Gamma M} + k_{\Gamma X}}$ in the definition of $p(y, \theta)$ allows satisfying the first requirement. On the other hand, a cosine function was introduced in the definition of $p(y, \theta)$ in order to fulfill the condition of periodicity of the wave vector, as $\theta$ scans all angles within $[0 - 2\pi]$ in the first Brillouin zone. The analytical form of $k(y, \theta)$ that the closest matches to the EFCs whatever is the filling factor within the interval $[0.07 - 0.5]$, corresponding to the actual samples that we have investigated (see below), is:

$$k(y, \theta) = k_{\Gamma X}(y) \frac{1 - \alpha(y) cos(4\theta)}{1 - \alpha(y)}. \tag{2.20}$$

The EFCs at 5 MHz for several values of the filling factor computed using FEM (full lines) or derived from equation (2.20) (indicated by circular markers) are displayed in figure 2.9. The agreement between both is excellent. EFCs are computed using both methods and setting the frequency to different values in between 3 and 13 MHz (see $r = 0.4a$ in figure 2.2(b)): whatever the frequency and the filling ratio are, the agreement is equally good.

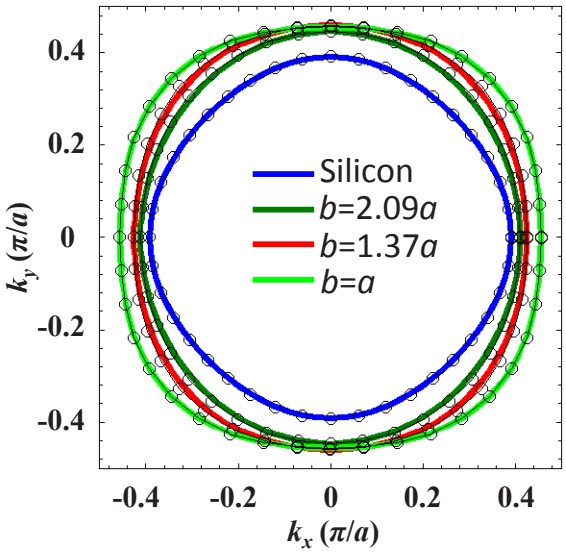


Figure 2.10: EFCs at 5 MHz (solid lines) and the corresponding fits derived from equation (2.21) (circular markers) for a PC with the rectangular symmetry and for different aspect ratios $b/a$.

Deriving the trajectory $y(x)$ within the GRIN PC is then straightforward. Indeed, one must simply calculate both the derivatives of $k_x$ and $k_y$ with respect to $\theta$, using equation (2.16) and equation (2.20) and then integrate their ratio according to equations (2.17) and (2.18).

### Rectangular lattice

As with the preceding case, one can account for the anisotropy of the rectangular lattice by introducing in the definition of $p(y,\theta)$ two dimensionless parameters, $\alpha(y) = \frac{k_{\Gamma M} - k_{\Gamma X}}{k_{\Gamma M} + k_{\Gamma X}}$ to account for the difference in the lengths of the wave vector along ΓX and ΓM and $\beta(y) = \frac{k_{\Gamma Y} - k_{\Gamma X}}{k_{\Gamma Y} + k_{\Gamma X}}$ for the mismatch along ΓX and ΓY. In addition, we introduced in the definition of $p(y,\theta)$ a cosine function to account for the two-fold axis of the rectangular symmetry. Considering both these requirements, we obtained the best fits to the computed EFCs with the function:

$$k(y,\theta) = k_{\Gamma X}(y)\left\{\frac{1-\alpha(y)cos(4\theta)}{1-\alpha(y)} + \beta(y)[1-cos(2\theta)]\right\}. \tag{2.21}$$

As can be seen from figure 2.10, whatever is the value of the aspect ratio $b/a$ in the sample, or equivalently the filling factor in the range $[0.24 - 0.5]$, the fits to the EFCs were as good as for the square lattice. Indeed, at 5 MHz, the largest deviation was less than 2%; it appears along ΓM for the aspect ratio $b/a = 2.09$.

Both equations (2.20) and (2.21) well take into account the anisotropy along the

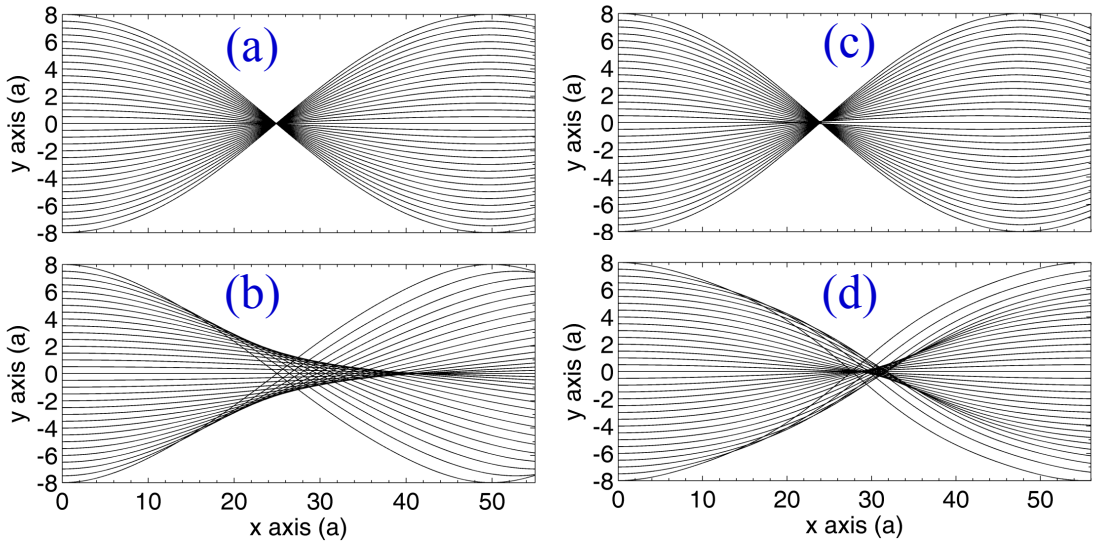


Figure 2.11: Ray trajectories of GRIN PC in square lattice (a) ignoring the anisotropy by setting $k = k_{\Gamma X}$ and (b) with an exact consideration of anisotropy; Ray trajectories of GRIN PC in rectangular lattice (c) ignoring the anisotropy by setting $k = k_{\Gamma X}$ and (d) with an exact consideration of anisotropy.

lines of inclusions where the EFCs may depart from a circle. Both remain valid as long as the EFC is a closed curve and for any frequency below the first band gap in the dispersion curves that opens at point X and 13 MHz for the square symmetry (figure 2.7) and at point Y and 5 MHz for the rectangular symmetry (see right panel in figure 2.6).

An example of computing ray trajectories is found in the Appendix A for the GRIN PC with square symmetry. Such an example can be easily extended to GRIN PCs of other lattices.

### 2.3.3 Effect of anisotropy of GRIN PCs

It is interesting to visualize the influence of anisotropy of EFCs before further investigations by other methods. To this end, the ray trajectories of wave beams were obtained for two cases: anisotropy ignored by setting $k(y, \theta) = k_{\Gamma X}(y)$ for each horizontal layer, and anisotropy considered by using the above formalism.

Figures 2.11(a) and 2.11(b) present the corresponding results for elastic waves in GRIN PC with square symmetry. When the local anisotropy is ignored, incident wave beams are converging to a single point at about $x = 25a$ with no aberration, as shown in figure 2.11(a). Actually, in the designed GRIN PC with a square lattice, $k_{\Gamma X}(y)$ variation is close to a hyperbolic secant profile with $k_{\Gamma X0} = 0.457\pi/a$, $n_0 = 1.166$, and $\delta = 0.065a^{-1}$. If ignoring the anisotropy, the focusing is expected

at $x = 24.2a$, in good agreement with the ray trajectory calculation and equation (2.14). When the local anisotropy is considered exactly, a focusing zone with strong spherical aberrations occurs. The anisotropy of GRIN PC, as the irregularity of geometry of optical lenses, leads to strong aberration at the focusing zone. Therefore the focusing zone spreads out to a position at about $x = 30a$. This is unexpected from the original design of GRIN PC.

Ray trajectories of the beam have also been obtained for GRIN PC with a rectangular lattice for the same two cases: ignoring anisotropy or considering anisotropy, as shown in figures 2.11(c) and 2.11(d) respectively. No aberration is found when anisotropy is ignored with a focal distance almost equal to the counterpart of the square lattice. This can be well explained by the fact that, in the designed lens with a rectangular lattice, the $k_{\Gamma X}(y)$ obeys a hyperbolic with $k_{\Gamma X0} = 0.457\pi/a$, $n_0 = 1.166$, and $\delta = 0.066a^{-1}$. When the anisotropy is accounted for, strong aberrations are observed in the focusing zone, in the vicinity of $x = 31a$. The aberrations here, with ray trajectories concentrated at $x \sim [26a, 33a]$, are less spread along $x$-axis than displayed in figure 2.11(b). This is because of the reduced anisotropy for the GRIN PC of rectangular lattice, which will be discussed below in the subsection 2.5.3.

*In what follows, we investigated the dynamics of the focusing process with the help of numerical methods and experimental observations.*

## 2.4 Numerical study of focalization

### 2.4.1 Time dependent computations

FEM was applied to calculate the displacements field of $A_0$ mode associated with the propagation in the GRIN PCs.[66] To this end, we used the *time dependent* module in *structures* in Comsol Multiphysics. The systems were designed in such a way that they had a width (along $y$ axis) $17a$ for the square lattice and $16.5a$ for the rectangular lattice. In addition, to mimic at the best the experimental situation and to avoid unwanted reflections on the boundaries of the phononic plate, the structured part of the sample were surrounded by a large area of homogeneous silicon, free of air inclusions.

A line *force*, along $z$-direction vibrating at 5 MHz, was applied in front of the GRIN PCs to continuously excite the waves. The calculation was set to follow a time step of one-tenth period. Such a source gave a wavelength along $x$-axis in good agreement with the theoretical predication $\lambda_{\Gamma X}(y) = 2\pi/k_{\Gamma X}(y)$ for any wave vector measured along $y$-axis. Meanwhile, the Fourier transform of time dependent $u_z$ was centered at exactly 5MHz. These two features have confirm the accuracy of

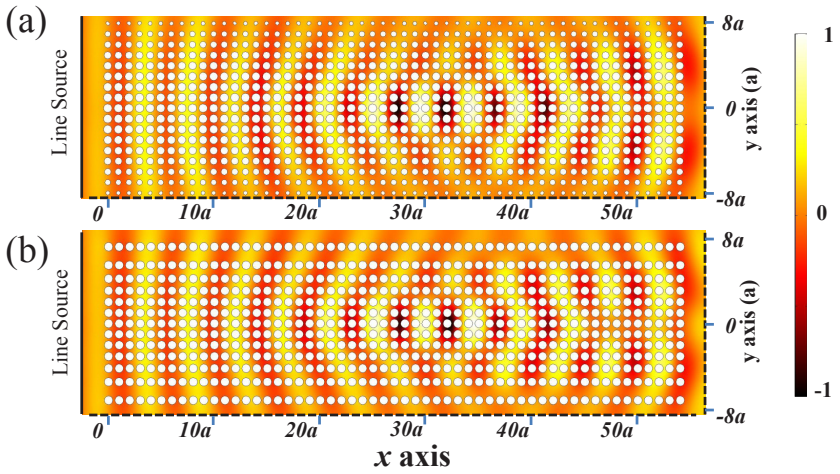


Figure 2.12: Snapshot of the out-of-plane displacement $u_z$ in a GRIN PC of 55 columns with a square lattice (a) or with a rectangular lattice (b).

the antisymmetric mode source, paving the way for further studies.

### 2.4.2 Numerical results of $A_0$ mode focalization in GRIN PC

Figure 2.12 shots the snapshots of $u_z$ on a GRIN PC of 55 columns with (a) square symmetry and (b) rectangular symmetry. $u_z$ is normalized to unity in both cases. The displacement field has its maximum value at about $x = 32a$.

To allow for more precise comparisons with the ray trajectories, $u_z$ was calculated for GRIN PC of 120 columns for both symmetries. For each point measured on the surface of GRIN PCs, we found the maximum value of $u_z$ during the whole recorded time range. After that, all these maxima were normalized to the same scale accordingly to the GRIN PC. Figure 2.13 depicts the normalized maximum amplitude of $u_z$ in the GRIN PC with (a) square symmetry and (b) rectangular symmetry. In these figures, the dash lines are for the ray trajectories derived from the formalism established in the preceding section.

For the GRIN PC with square symmetry, FEM simulations predict the normal displacement to be maximum at the distance $34.5a$ from the origin, in good agreement with the 55 columns long sample. The focal distance is almost twice the distance of $18a$ derived from equation (2.14). Moreover, the amplitude along $x$-axis is more than 90% of its maximum value in between $x = 28a$ to $x = 40a$ (figure 2.13(a)). These spherical aberrations that are not predicted by a simple theory of rays in a GRIN lens with a hyperbolic secant profile, are the consequence of the non-circular shape of the EFC. Actually, in this case $\theta$ and $\varphi$ are not equal, all the rays do not converge on a single point, and equation (2.14) is not relevant to

calculate the focus distance anymore. Consequently, the elastic energy spreads out along $x$-axis and the focal spot covers an area larger than expected.

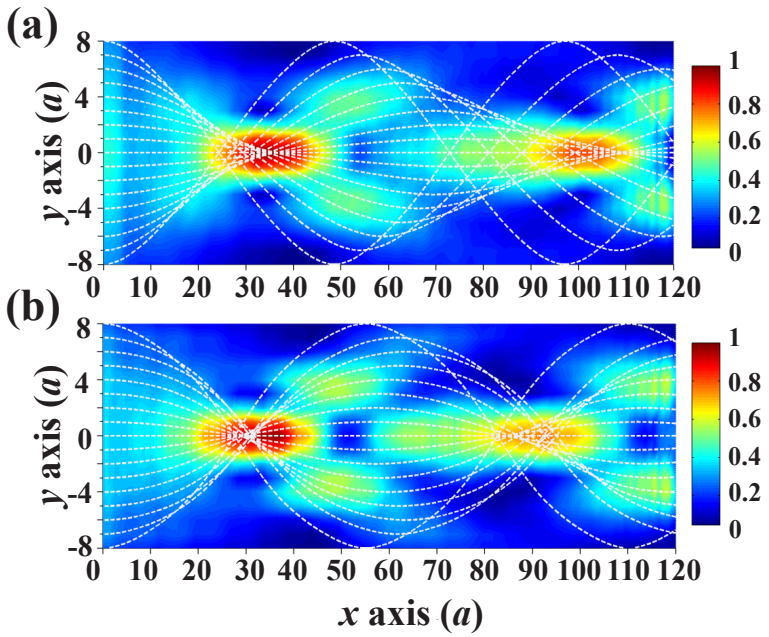


Figure 2.13: Normalized maximum of the displacement $u_z$ in a GRIN PC of 120 columns with a square lattice (a) or with a rectangular lattice (b). Dash lines are for the ray trajectories derived from the formalism described in section 2.

As expected, the second maximum appears at $x = 103a$, about three times the focal length of $35a$. The sound ray paths displayed in figure 2.13(a) well explain the large spreading out of the elastic energy along $x$ axis. Indeed, the aberrations increase as the waves propagate and the maximum amplitude on this second focus spot is only $\sim 84\%$ of the value measured on the first one. At the same time, the normal displacement has a smoother profile along $x$-axis.

Similar features are observed for the spatial distribution of displacement in the GRIN PC with rectangular symmetry (figure 2.13(b)). As in the previous case, the first focal point arises around $33.5a$, far from the theoretical value derived from the effective refractive index and equation (2.14) (about $18a$). However, this geometry leads to less spherical aberration, as can be seen from the ray paths drawn in figure 2.13(b), and the elastic energy spreads out over a smaller distance along $x$-axis: the area where the amplitude is 0.95 times the maximum value extends over $5a$ in the case of the rectangular lattice, against $\sim 8a$ for the square lattice. This also explains the lateral profile along $y$-direction that turns out to be sharper with the rectangular symmetry than it is with the square symmetry (see below). As expected, a second focus arises at $x = 92a$, about three times the focal length. The maximum amplitude of this second focus is $\sim 0.80$ times the maximum amplitude at the first focus, corresponding to a lessening similar to what is observed with the

square lattice.

## 2.5 Experimental study of focalization

### 2.5.1 Background

In order to allow for relevant comparisons with theory, two GRIN PCs were elaborated on a 110 $\mu$m thick silicon plate according to the designs described in the previous sections.

In known studies, many methods have been applied to generate $A_0$ Lamb mode, including a laser-based technique,[28,83,84] piezoelectric transducers,[85–88] and interdigital transducers (IDTs).[89–91] Among these methods, excitation of elastic waves using piezoelectric transducers are widely used to examine elastic properties of large-scale composites, featuring a high intensity of energy. Laser based technique and IDTs, however, can be sufficient for investigating small-scale samples of one hundred micrometers or even smaller.

IDTs need being put on the surface of a substrate, which may add some complexity of the experimental process. IDTs have also their excitation efficiency limited by the distance between transducers. This is to say, once the transducers are fixed on the substrate, it is impossible modifying the frequency of the generated elastic waves while at the same time keeping a high efficiency.[89–91] The laser based technology allows to overcome this barrier. Laser pulses go through certain optical system to obtain a periodical pattern of bright and dark strips similar to the arrangement of IDTs. Distance between these strips can be monitored in order to pursue the aimed frequency. During the experiments of this thesis, the frequency has been tilted from 3 MHz to 20 MHz or even higher depending on the configuration of the optical system, covering almost the whole range of $A_0$ mode band compatible with the detection stage. Based on these considerations, the laser-based technique was applied all through this work to generate wave pulses.

$A_0$ Lamb mode as well as Rayleigh waves features the dominance of out-of-plane displacement. To measure this displacement, ultrasonic transducers and IDTs have similar limitations as for exciting elastic waves. However, the optical method described in the next section can be used to detect the displacement almost everywhere on the surface of samples.[28,83,84] Therefore, we made use of this laser-based technique to measure the out-of-plane displacements all through in this work.

### 2.5.2 Description of experiments

#### Wave excitation

We used Nd:YAG laser that delivers ultra-short light pulses lasting 35 ps with a wavelength 532 nm and 20 MHz repetition rate. Figure 2.14 shows the experimental configuration where the green flashes indicate the trace of laser pulses. These laser pulses passed through a mask and several mirrors before being focused onto the surface of the silicon plate, just a few millimeters in front of the GRIN PCs.

The mask, featuring a periodic constant $d$, caused a spatially alternating bright and dark pattern that is focused onto the sample. At a certain distance, the bright and dark strips correspond to the bottom and peak values of intensity, producing a maximum contrast of the energy between the two areas and making the fringes look *clear*. Distance between the grading mask and silicon plate can be adjusted to satisfy such a contrast or very close to it. These bright strips are partially absorbed by silicon which induces expansion of the plate surface and in return produces elastic waves pulses through photoelastic process.

Both the first and the second optical lenses had a cylindrical shope (figure 2.14). To explain the function of these lenses, figure 2.15 shows the fringe pattern on a card just in front of the silicon plate with an angle to the incident beam. The $x$ and $y$ indicate the local horizontal and vertical axis on the card. The first cylindrical lens was set in such a way that it controlled the distance between fringes along $x$-axis. It had few influences on the length of the strips along $y$-axis. The second cylindrical lens, on the contrary, controlled the length of strips along $y$-direction with few influences on the distance between the fringes along $x$-direction. Such an independent control of the fringes pattern by two cylindrical lenses enabled to finely tune the pulses.

The first lens had its support fixed on a slide which could be moved precisely. By changing the position of this lens, the distance between fringes on the silicon plate was modified, so that the central frequency of the elastic wave pulses was shifted. Figure 2.16 presents the central frequency of the observed signal against the distance between the first lens and the silicon plate. A linear relationship is observed between the two parameters, so that the frequency can be predicted from this curve.

During all the process, the second optical lens was fixed to a certain position so that the impinged area had an elliptic shape on the card. A short strip length along $y$-axis concentrated energy in a small area in order to increase the efficiency of wave excitation. The strip length, however, needs to be large enough in comparison to the length of the GRIN PC, so that elastic wave pulses can be treated as plane wave

sources. The second cylindrical lens was placed at a position insuring this property.

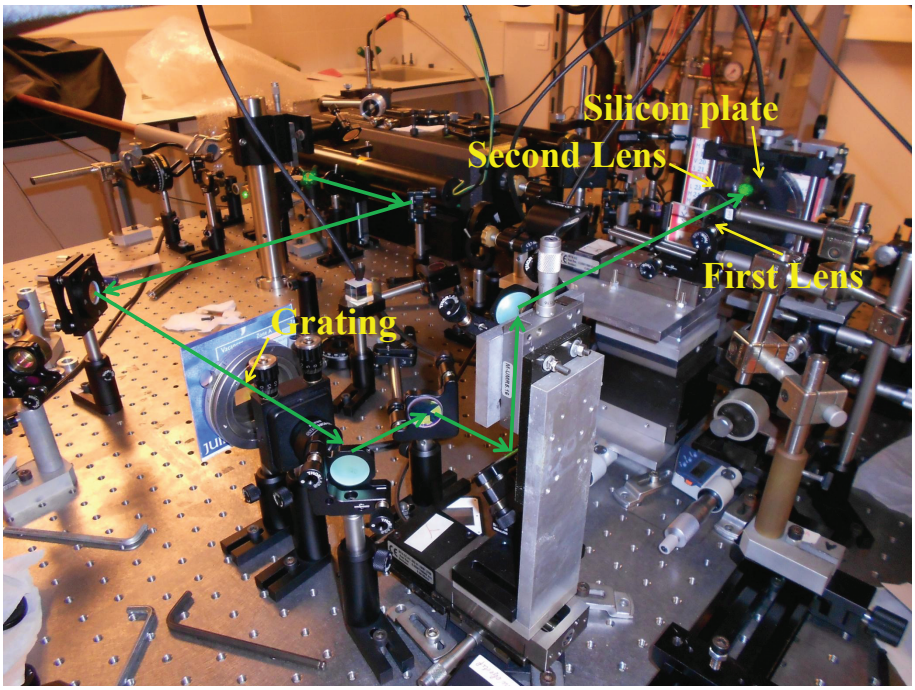


Figure 2.14: Experimental configuration of wave excitation.

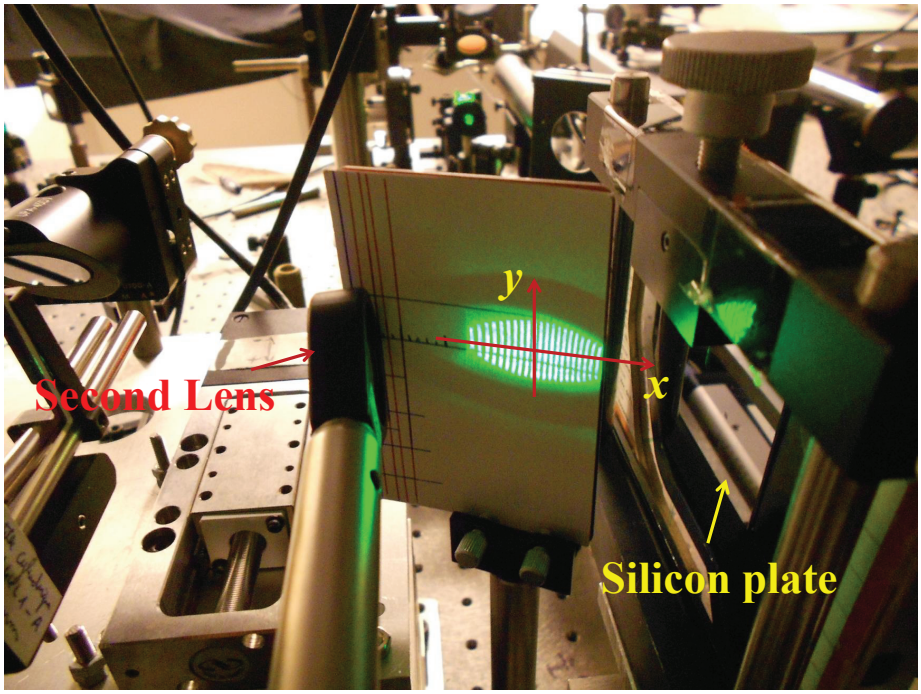


Figure 2.15: Configuration of fringe pattern.

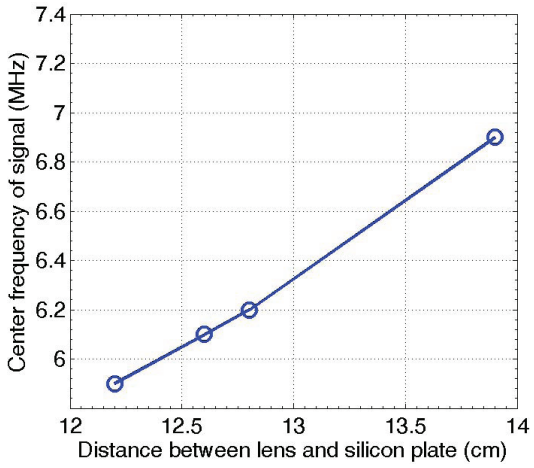


Figure 2.16: Shift of the central frequency of the observed signal against the distance between the first cylindrical lens and the silicon plate.

### Wave detection

We recorded the time dependance of $u_z$ at any point on the surface of the sample, inside the GRIN PC using a Michelson interferometer in which the light source was a He-Ne laser (632.8 nm). Figure 2.17 shows the experimental configuration of Michelson interferometer. One beam of the interferometer was focused on the sample acting as one of the mirrors of the interferometer to a spot size of $\sim 5$ $\mu$m, whereas the reference beam was reflected by an actively stabilized mirror. A high-speed photodiode collected the interference pattern that was then digitized at 500 MS$\cdot$s$^{-1}$ by a digital oscilloscope. We obtained a very good S/N ratio after averaging a few hundreds of scans. The microscope and the sample were both mounted on translation stages in such a way that the probe beam could be scanned across the sample with a precision of about 1 $\mu$m. This noncontact technique allowed us to record the out-of-plane component at any location on the surface of the sample and to study in details the focalization of the acoustic waves into the GRIN PC.

Figure 2.18 shows an example of the treatment of recorded signals. Figure 2.18(a) shows a signal recorded directly by the high speed photodetector noted as $I(t)$. Mean value of $I(t)$ was then removed by the relationship $\widetilde{I}(t) = I(t)/I_{ave} - 1$ with $I_{ave}$ presenting the mean value of $I(t)$ at the initial time range being about -66 (figure 2.18(b)).[92] Frequency spectrum of the signal of interest $\widetilde{I}(t)$ recorded in the time domain $t = [2 - 5]$ $\mu$s was then analyzed. The central frequency was located at about 5.1 MHz (figure 2.18(c)), satisfying the requirement. A Gaussian window centered at 5 MHz with a width of about 1 MHz was used to filter the frequency spectrum. The filtered spectrum was Fourier transformed back to the time domain noted as $\widehat{I}(t)$, as shown by the figure 2.18(d).

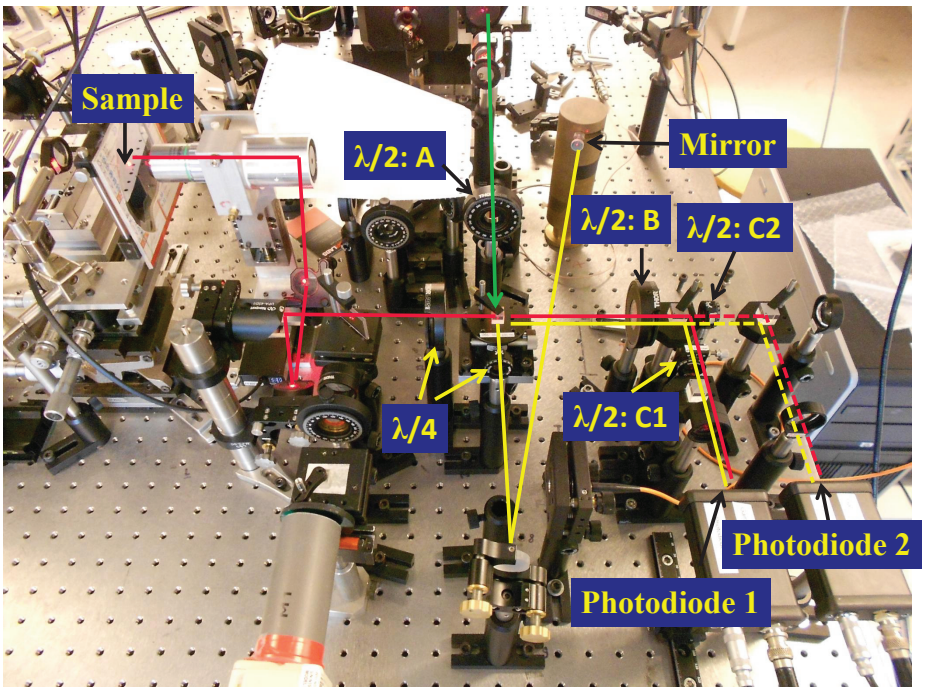


Figure 2.17: Experimental configuration of Michelson interferometer

$u_z$ is finally determined by the relationship[92]

$$u_z(t) = \frac{\widehat{I}(t)\lambda_{HeNe}}{4\pi C_{contrast}}, \tag{2.22}$$

where $\lambda_{HeNe}$ is the wavelength of the He-Ne laser 632.8 nm. $C_{contrast}$ is a parameter presenting contrast of the interference pattern

$$C_{contrast} = \frac{C_{max} - C_{min}}{C_{max} + C_{min}}, \tag{2.23}$$

where $C_{max}$ and $C_{min}$ are the maximum and minimum value of Michelson interferometer. This parameter is dependent on surface qualities, such as the smoothness and cleanness.

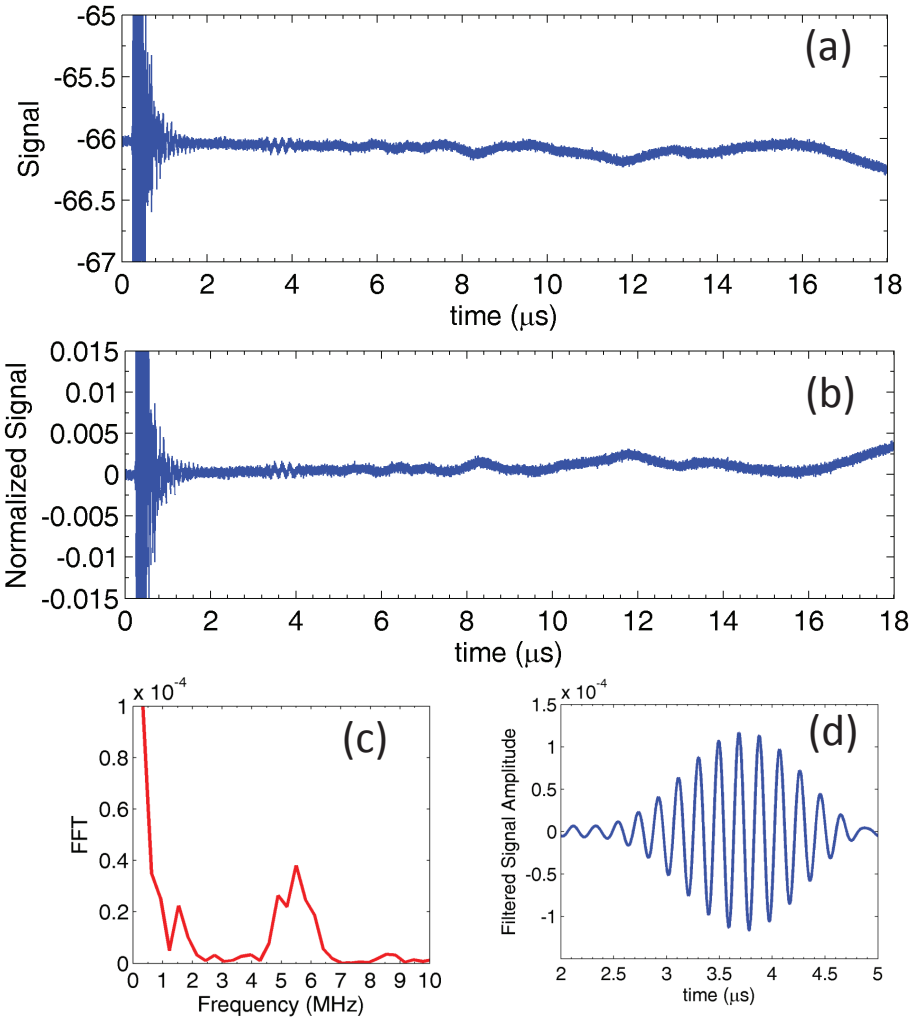


Figure 2.18: (a) Signal measured directly by the photodetector $I(t)$, (b) normalized signal $\tilde{I}(t)$ by removing the mean value $I_{ave}$, (c) frequency spectrum of normalized signal of $[2-5]$ $\mu s$, and (d) time signal $\hat{I}(t)$ obtained from the inverse Fourier transform of data in figure (c) filtered by a Gaussian window centered at 5 MHz with a width of 1 MHz.

### 2.5.3 Experimental results of $A_0$ mode focalization in GRIN PC

Wave propagation has been monitored in the middle the section of the sample featuring 120 columns of inclusions. Figure 2.19 shows snapshots of $u_z$ at three different moments after the sample with the square symmetry has been excited into vibration. A first focus is observed to be centered at a focal length about $x = 32.5a$ (figure 2.19(a)), which is good agreement both with the numerical results ($x = 34.5a$) and the ray trajectory analysis presented in previous sections. Behind the focus spot, the elastic beam is expected first to be divergent within the waveguide, as it is shown in figure 2.19(b), and then to re-focus on a second point located at $97.5a$, i.e., three times the focal distance of the lens (figure 2.19(c)). This is what is indeed observed, in good agreement with the numerical results. The maximum amplitude of the second focus is measured to be about 0.68 times what was observed on the first focal spot, which is a little less than the numerical result.

Very similar behaviors were observed with the experimental sample featuring the rectangular symmetry (figure 2.20). The focal distance in this latter case is measured to be $\sim 28a$, slightly less than the focal distance of $32.5a$ measured in the previous sample. As expected, a second focus is formed at $x = 90a$ with an amplitude of about 0.63 times the maximum value. This is in good agreement with the corresponding numerical simulations.

The gain factor, defined as being the ratio of the maximum displacement at the focus to the amplitude of the elastic wave measured close to the excitation area of lens, allows for quantitative comparisons between both structures. We observed a value of 3.5 (corresponding to a maximum displacement of 21 pm at the focus) with the square lattice against 3.2 (maximum displacement 16 pm) when using the lens with the rectangular lattice. These values fairly well agree with the ones derived from the numerical simulations: 3.9 in the former case and 3.6 in the latter case. Beside the smaller gain factor obtained with the rectangular lattice, this system features a greater uniformity in the distribution of elastic energy inside the first focus.

As described in figures 2.21(a) and 2.21(b), the measured maxima of $u_z$ for the square symmetry and for the rectangular symmetry respectively. Whatever the symmetry is, the amplitude is not homogeneous in between the two focal points. This is consistent with numerical results (see figure 2.13); this feature is ascribed to the spherical aberrations at the second focus. It is noticed that the amplitude recorded within an area about $20a$ long along $x$-axis before the second focus is slightly less than expected from the simulations (see figure 2.13): a mean amplitude around 0.4 is measured (in normalized units) instead of 0.5 as predicted by simulations.

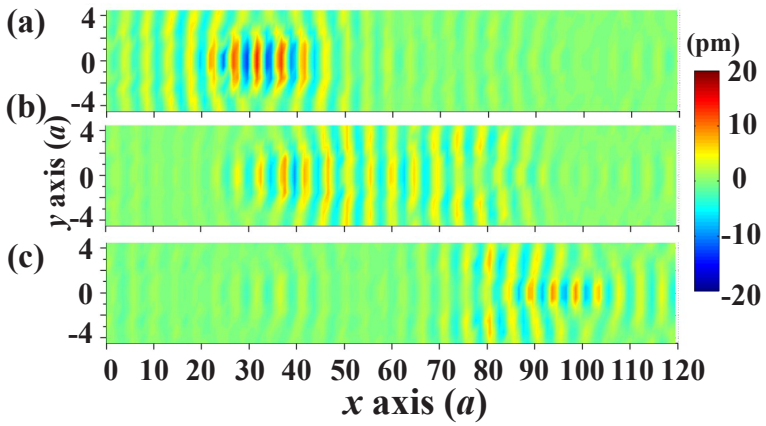


Figure 2.19: Amplitude of the out-of-plane displacement $u_z$ in a GRIN PC with the square lattice, measured at three different times

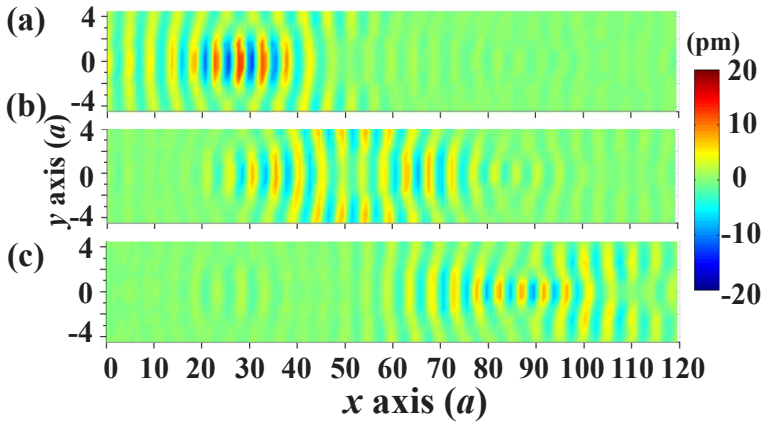


Figure 2.20: Amplitude of the out-of-plane displacement $u_z$ in a GRIN PC with the rectangular lattice, measured at three different times

Several reasons may explain this small discrepancy, including the slightly coupling of the symmetric mode [10] or tiny irregularities in shape, sizes and spacing of the holes, which may induce the non-coherent diffusion of the elastic waves onto the air inclusions.

As regards the focalization efficiency of the acoustic lenses, it can be evaluated through the profiles of the focal spot along both $x$-and $y$-directions. In the left panel of figure 2.22, we show as full lines the normalized longitudinal profiles achieved with the square lattice (figure 2.22(a)) and with the rectangular lattice (figure 2.22(b)). We show the corresponding profiles along $y$-axis in figure 2.22(c) and 2.22(d) respectively. From these data, the full width at half maximum (FWHM) was measured to be $7\lambda$ along $x$-axis. The experimental transverse size of the spot was $0.71\lambda$ for the square lattice and $0.64\lambda$ for the rectangular lattice. These values are in good agreement with the ones derived from the numerical simulations: $0.84\lambda$ in the former case and $0.75\lambda$ in the latter case, quite close to the Abbé limit of $0.5\lambda$.

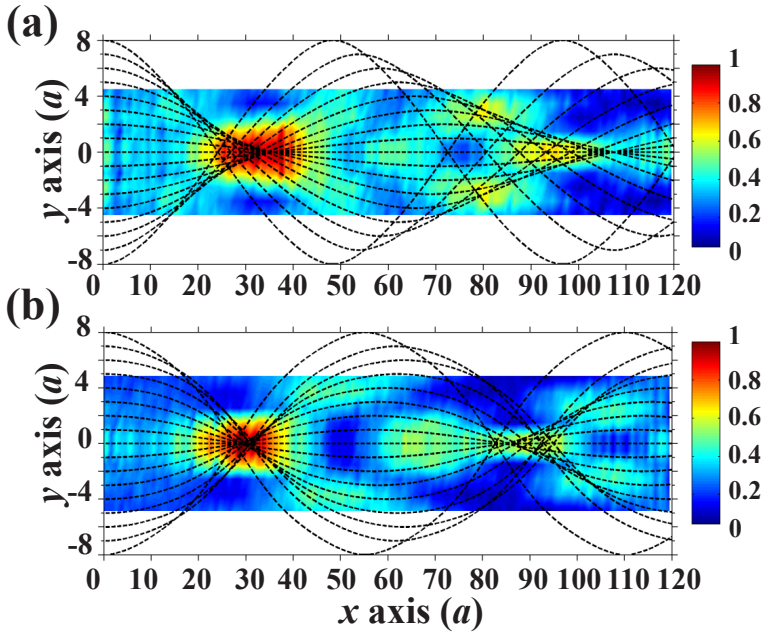


Figure 2.21: Experimental maximum of the out-of-plane displacement $u_z$ in a GRIN PC with a square lattice (a) or with a rectangular lattice (b). Dash lines represent the calculated ray trajectories.

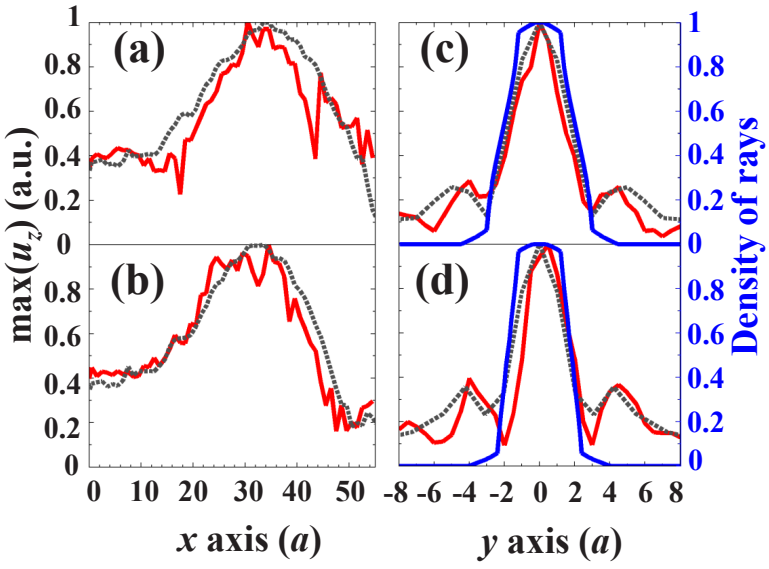


Figure 2.22: Normalized profiles of the out-of-plane component $u_z$ in the focus area. The red lines are for the experimental data, the black lines are for the numerical simulations, and the blue lines represent the density of rays (see the text). Along $x$-axis: square lattice (a) ; rectangular lattice (b). Along $y$-axis: square lattice (c) ; rectangular lattice (d).

In addition, it should be noted that the formalism developed in section 2 also allows for a quantitative analysis and efficiently predicting the waist of the beam. To

show that, we have drawn the ray trajectories for more than 3000 initial positions evenly distributed along y-direction in between $\pm 8a$ and we have computed the number of rays intersecting a segment of a given length, sliding along a line parallel to $y$ axis at position $x = 30a$. This *linear density of ray* against the position of the segment is drawn as a blue line in figures 2.22(c) and 2.22(d). The agreement with the experimental results and the FEM calculations is very good, except for the peaks centered at $y = \pm 4a$ that are not predicted by the model.

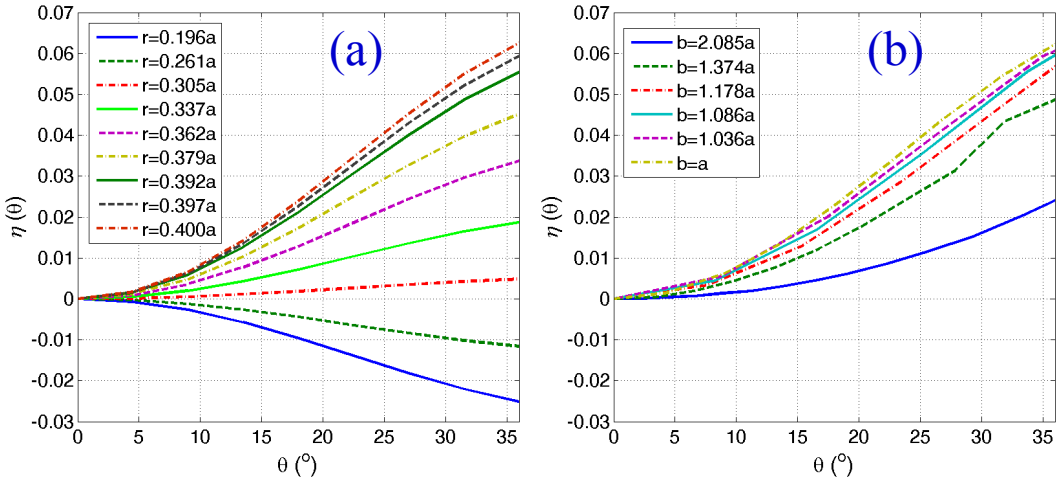


Figure 2.23: Profile of anisotropic ratio $\eta(\theta)$ for GRIN PC (a) in square lattice with different air holes or (b) in rectangular lattice with different aspect ratios $b/a$.

It is important to understand the physical reasons why the lateral profile along $y$-axis is sharper with the rectangular symmetry than it is with the square symmetry. Actually, the origin of a better FWHM clearly lays in the smaller aberrations along $y$ axis in the former case than the ones founded in the GRIN PC with square lattice. This follows from the dependence against $\theta$ of the anisotropy coefficient $\eta$, which is very different according to the symmetry. Indeed, for both symmetries and for any ray trajectory, the wave vector $\mathbf{k}$ lays along a direction that makes an angle $\theta$ with respect to $x$ axis ranging between $0°$ and $\sim 35°$ (see figures 2.23 (a) and (b)). In this range, for the rectangular symmetry, $\eta(\theta)$ very few depends on the aspect ratio $b/a$ (figure 2.23(b)): as long as this ratio takes a value no more than $\sim 1.5$, $\eta(\theta)$ varies almost linearly from 0 at $\theta = 0°$ to a value comprised in between 0.05 (for $b/a = 1.37$) and 0.06 (for $b/a = 1$) at $\theta = 35°$. This is in contrast to the situation encountered in the lens with the square symmetry (figure 2.23(a)). In that case, $\eta(\theta)$ varies quasi-linearly against $\theta$ as well, but with a mean slope, which is either positive or negative and strongly depends on the aspect ratio. As long as the ratio $r/a$ keeps values around $\sim 0.3$ or less, the anisotropy of the medium is mainly that of crystalline silicon whereas the anisotropy of the effective medium dominates for

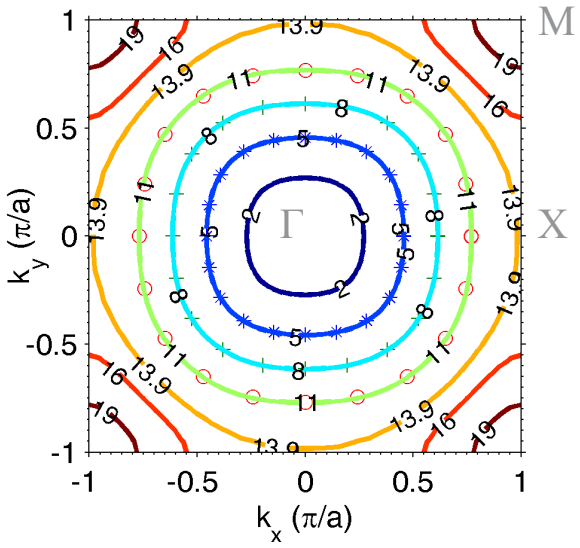


Figure 2.24: Equal frequency contours of $A_0$ mode in the first Brillouin zone for air/silicon phononic crystal with unit width $a = 100$ $\mu$m, radius of air hole $r = 40$ $\mu$m, and plate thickness $h = 110$ $\mu$m. The star, plus and circle are symbols obtained from the fitting formula.

larger values of the aspect ratio. Consequently, a greater spreading out of the rays, and a broader profile in turn, occur with the square symmetry.

## 2.6 Discussion on focalization within large frequency range

Besides the investigation of the wave focusing at 5 MHz, it is interesting to extend the study to higher frequencies. As mentioned before, EFCs can be fitted in almost the whole range of $A_0$ band. To demonstrate this, figure 2.24 depicts the EFCs of PC featuring $a = 100$ $\mu$m, $r = 40$ $\mu$m, and $h = 110$ $\mu$m (see figure 2.2(b)). The stars, plus and circles are for the fitting data derived from equation (2.20) for 5 MHz, 8 MHz and 11 MHz, respectively. Good agreement has been found between the results of three groups. However, the fitting formula losses its validness when EFC is no more centered at Γ point at 16 MHz or 19 MHz in the first Brillouin zone, which is out of the scope of this thesis although similar procedures can be applied. Figure 2.25 shows the normalized maximum of $u_z$ in the GRIN PC with square symmetry at (a) 5 MHz, (b) 8 MHz, and (c) 11 MHz, respectively. The dash lines are for the corresponding ray trajectories derived from the formalism.

In figure 2.25(a), a focusing zone appears at $x \sim [27a,\ 42a]$ with the overall maximum of $u_z$ located at $x = 35a$. Inside this focusing zone, the ray trajectories are dispersed, because of aberrations which are very similar to the spherical

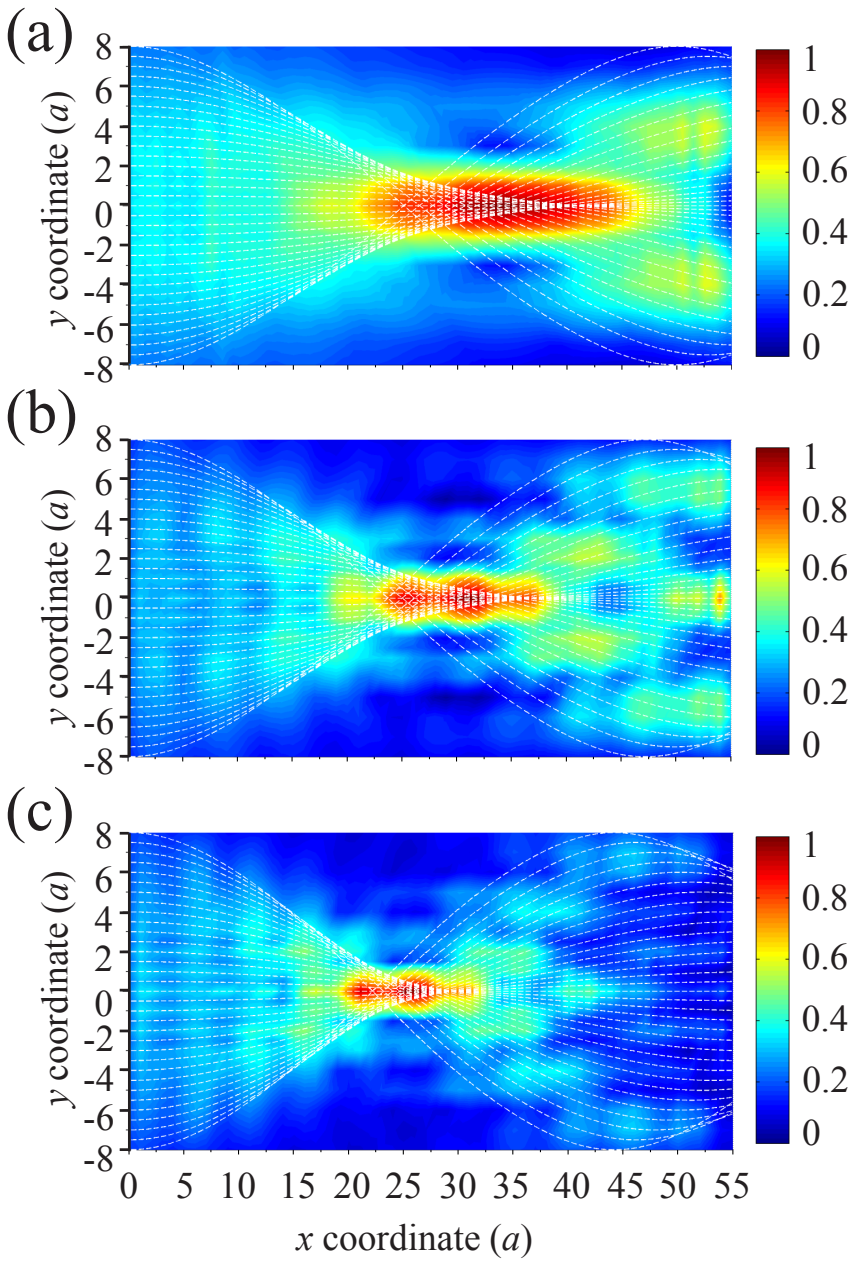


Figure 2.25: Normalized maximum of out-of-plane displacement $u_z$ at the inner of GRIN PC of 55 columns at (a) 5 MHz, (b) 8 MHz, and (c) 11 MHz; in all of figures, dashed lines indicate the corresponding ray trajectories.

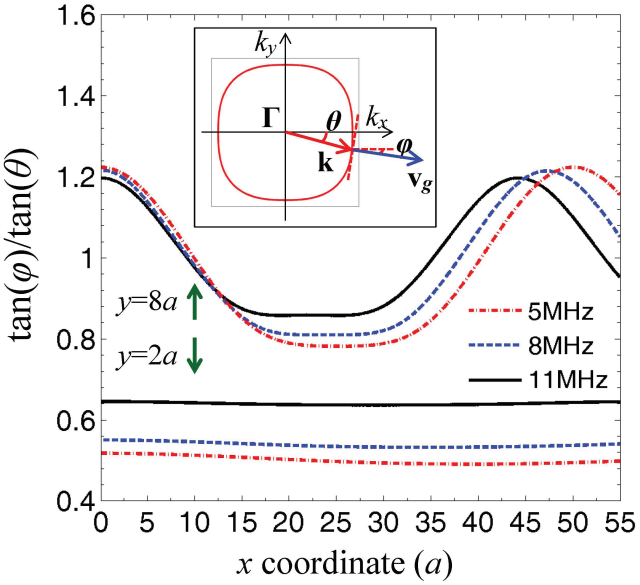


Figure 2.26: The ratio $\tan(\varphi)/\tan(\theta)$ at 5 MHz(dot-dashed lines), 8 MHz(dashed lines) and 11 MHz(solid lines) for two ray trajectory incident at $y = 8a$ and $y = 2a$.

aberrations encountered in optical lenses. The focusing zone much more extends along $x$ axis than it does along $y$ axis, where the lateral dimensions of the spot is $y \sim [-1.5a,\ 1.5a]$.

Furthermore, the ray trajectories issued from the edges converge at a shorter distance than the ray trajectories issued from the zone close to the central axis axis of the GRIN PC do. For example, the rays impinging the lens at $y = \pm 8a$ converge at a distance $x = 26a$, while the value goes to $40a$ for rays at $y = \pm 2a$. This must be related to the anisotropy coefficient which takes larger values for $y$ close to the central axis than it does for larger values of $y$, where the filling ratios are small. When the anisotropy within each PC line constituting the lens is ignored by setting $k(y, \theta) = k_{\Gamma X}(y)$, all rays focalize to a single point, at a distance $24.2a$ from the origin. However, when considering this anisotropy the directions of phase velocity and group velocity are not parallel anymore, as shown in the inset in figure 2.26. As a consequence of Snell's law that states the conservation of the wave vector $\mathbf{k_x}$ at the entrance of lens, for incident waves close to the central layer the angle $\theta$ is limited to a very small region where the angle $\varphi$ is much smaller than $\theta$, as shown by the ratio $\tan(\varphi)/\tan(\theta)$ for the rays incident at $y = 2a$. Thus the ray trajectory is prolonged along $x$-coordinate, and the focal distance becomes larger than expected. For rays incident far from the central axis, angle $\varphi$ is first larger than $\theta$, and then becomes smaller as $x$ coordinate increases, as shown by the ratio $\tan(\varphi)/\tan(\theta)$ for the ray incident at $y = 8a$. This characteristic may compensate the anisotropy to a certain extent, resulting to a focal distance very close to value derived from

$f_l = \pi/2\delta$ (equation (2.14)).

In figure 2.25(b), the overall maximum of $u_z$ at 8 MHz was found to be centered at $x = 30a$, inside a focusing zone extending over $x = [27a,\ 32a]$ and the focal distance becomes shorter. Actually, the refraction index fits with a hyperbolic secant profile with $n_0 = 1.129$ and $\delta = 0.063$. Meanwhile, the ratio $\tan(\varphi)/\tan(\theta)$ keeps values close to 1, with smaller variations for rays impinging the lens at $y = \pm 8a$ than it was at 5 MHz; even, this ratio deviates less from 1 for the ray trajectory with $y = \pm 2a$. This behavior corresponds to the reduced influence caused by the anisotropy of the GRIN PC. In turn, the focus area is less elongated along $x$ axis, and the focal distance becomes smaller. Similar characteristics can be observed in figure 2.25(c) for focalization at 11 MHz with even a shorter focal distance at $x = 25a$: the refraction index can well be fitted by a hyperbolic secant profile with $n_0 = 1.151$ and the $\delta = 0.068$; moreover, the anisotropy is expected to have less influence as can be seen from the almost constant value of the ratio $\tan(\varphi)/\tan(\theta)$ at 11 MHz.

It is important to ask for the physical reasons leading to the high accuracy of the formalism that we have developed. To now the formalism is valid on the first acoustic branch and is simply based on the Snell's law. There are few opportunities for the appearance of high-order Bragg scatterings. Accordingly, the single mode approximation is supported, which agrees well with former study.[93] As a result, applying the Snell's law is sufficient to account for the aberrations in almost the whole range of $A_0$ Lamb mode along $\Gamma X$. The anisotropy of PC is considered to be location dependent and angle dependent which translates into $k = k(y, \theta)$ in an accurate way. As a result, the formalism remains valid for the $A_0$ mode even for high frequencies in the first acoustic branch.

To now, the effective refractive index is defined in equation (2.11) by the ratio of the group velocity in the background to that of the PC. In our formalism, equations (2.15)-(2.17) and (2.19)-(2.21) can be rewritten using an effective refraction index defined by the wavenumber

$$n_{eff}(y, \theta) = k/k_B(y, \theta), \tag{2.24}$$

or equivalently defined by the phase velocity $v_p$ ($k = \omega/v_p$)

$$n_{eff}(y, \theta) = v_p^B/v_p(y, \theta), \tag{2.25}$$

where $v_p^B$ and $v_p(y, \theta)$ are the phase velocities in the background and in the PC, respectively. Therefore it is more suitable to use the phase velocity to define the effective refractive index.

## 2.7 Conclusion

In this work, it is demonstrated that one can accurately determine the focal length, the size of the focal spot, and the displacement distribution within a GRIN PC when accounting for the overall shape of the EFCs or equivalently, for the local anisotropy if any, within a raw of inclusions. Being based onto a geometrical approach, the ray analysis presented here is phenomenological in that it gives full account of the observation although not derived from a theory but it remains valid whatever the polarization of the waves is. Whereas the paraxial ray equation[82] is well suited to accurately determine the focusing properties of a GRIN lens only when the EFCs are circular[61], this ray analysis is more general and allows accounting both for the position of the focus on $x$-axis and for the extension along $y$-axis. It should be also noted that only real $\mathbf{k}$ vectors are considered in the formalism described in section 2 and hence evanescent waves are not involved in the focusing processes.

From the experimental side, the focusing of $A_0$ mode has been demonstrated at 5 MHz in GRIN PCs featuring two different designs. These heterostructures are free from curved surfaces, compact, and therefore they can be integrated easily with other phononic devices. In both systems, a very good agreement is found between the numerical simulations and the experimental results. In particular, we have shown that the focusing over a spot with lateral dimension close to the Abbé limit are easily obtained with the acoustic lens with the rectangular symmetry. The anisotropy being responsible for the spreading out at the focus, one must recognize that, on average, the ultrasound beam shall be subject along the path, to less anisotropy with the rectangular symmetry than it is with the square symmetry. However, larger vibration amplitudes are obtained with the heterostructure with the square symmetry. As predicted by the numerical simulations, a second focus point was actually observed. For both systems we studied, the vibration amplitudes at this second focal point are more than half the vibration amplitude at the first focus.

Finally, we have investigated the focalization inside the GRIN PC within a large range frequency of the $A_0$ mode, from long-wavelength regime to short-wavelength regime. Through the analysis of the ray trajectories and numerical simulations, the focal distance is found to become smaller due to the enlarged variations of the refractive index as the frequency increases, always in conjunction with the spherical aberration caused by the anisotropy in the GRIN PC.

# Chapter 3

# Enhanced focalization of $A_0$ mode outside GRIN PC

## 3.1 Introduction

The acoustic beams emitted by a typical sound source, as for example a piezoelectric transducer, are often of low spatial quality. Roughly speaking, the spatial quality relates to inhomogeneities in the beam intensity and/or in the phase profile. It is commonly accepted that the beams of the highest spatial quality feature a Gaussian profile. The experimental technique we used in this thesis is based on the excitation of elastic waves using a frequency doubled laser beam. Thus, we kept the optical path of this laser as short as possible in order to avoid any distortion in the spatial quality of the beam. As a consequence, the elastic waves carry the signature of the pump laser quality and has a Gaussian profile as well.

We have justified in the second chapter the inner focusing of elastic waves using a GRIN PC, and we have shown their achievements including highly concentrated elastic energy and subwavelength resolution. However, under some situations or for some applications, it may be difficult to measure the amplitude of the acoustic displacement in the heterostructure or even, it may be more interesting to excite some other structures outside the GRIN PCs. Get a focusing behind an acoustic lens, as do the optical lenses, can be useful to solve such problems and to extend the applications of GRIN PCs. In the following, we investigate how we could obtain the focal point located behind the GRIN PC.

It has been shown in some studies[6,9,23] that the external focusing can still go beyond the diffraction limit. As noticed in chapter one, the super-resolution focusing has been observed both theoretically and experimentally through a number of unconventional lenses.[6,8–12,23–25,41,94,95] Some of these realizations stressed on the participation of the evanescent components to the spot, such as the negative-index

lens,[6] and negative-index phononic/photonic crystals.[6,8,9,23] While others have not being claiming that; such as in the works about the super oscillations[96–98] or the metalens.[12] In contrast to the negative-index lenses, the later devices consider the diffraction or the scattering of high-order wave numbers, leading to extreme focusing resolutions, while at the same time suffering from a low intensity at focus.

GRIN PCs that we used here feature a positive index and deal with the single-mode Bragg scattering.[60–66,68–71,74–77] A question then raises: whether the focusing resolution can be enhanced to the diffraction limit or even overcome it or not? Remembering the literature on optical GRIN lenses, it has been shown that enhanced resolutions are foreseeable for lenses with large values of the gradient coefficient and large refractive index.[82] To comply with this requirement, the first step is to find suitable PCs with extremely large refractive index. To this end, resonant structures are excellent candidates since unusual phenomena are expected at frequencies close to resonance(s).[99,100] Moreover, some of them have been highlighted by the extreme value of their refractive index.[101]

In this chapter, we start with the *conventional* GRIN PCs as the ones we used in chapter two. We are studying the limit of the resolution behind these lenses, and we are seeking the requirements for the GRIN PC to enhance the focusing achievements. As an answer both to this question and to these requirements, we have redesigned the GRIN PCs and we have been considering a resonant structure as the basic unit. The focusing of elastic waves behind such GRIN PCs has been investigated both numerically and experimentally. We demonstrate in this chapter that it is possible to further enhance the focusing with such a heterostructure. At last, we discuss on the physical phenomena at the origin of the enhancement of the resolution at the focus.

## 3.2 Focusing outside GRIN PC

### 3.2.1 Focusing through conventional GRIN PC

Let's consider the propagation of $A_0$ Lamb mode in a GRIN PC made of 21 columns with the same design as the rectangular symmetry in chapter 2. We first made a numerical study of this lens. A line source was placed in front of the sample to excite elastic waves at the monochromatic frequency of 5 MHz. Figure 3.1(a) shows a snapshot of the field distribution of the out-of-plane component $u_z$. The maximum value was measured to occur at $x = 23.5a$, *i.e.*, $2.5a$ behind the exit interface of the GRIN PC. This is very close to the value $x = 25a$ where the ray trajectories have a high density. Accordingly, the focus position can be predicted by the ray trajectories.

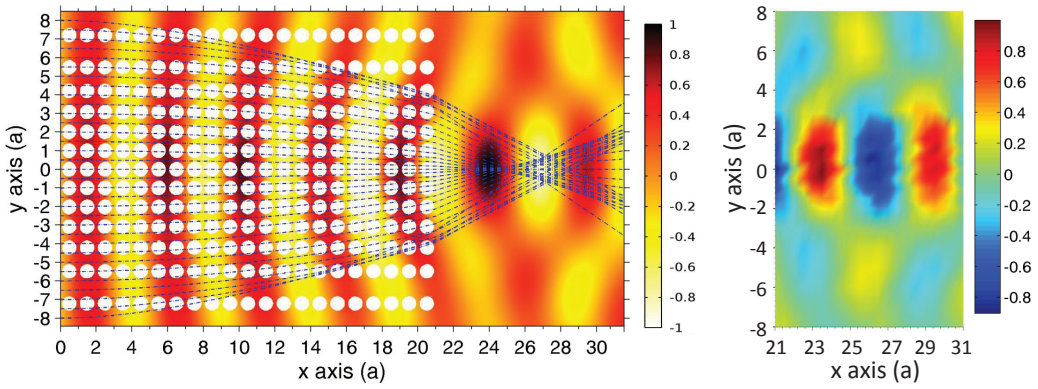


Figure 3.1: (a) Numerical and (b) experimental snapshot of normalized out-of-plane displacement $u_z$. Dashed lines indicate the ray trajectories.

We then made an experimental investigation of the system. The laser-based technique was applied both to excite $A_0$ Lamb mode pluses and to record the displacement filed $u_z$ in the time domain, as already described in chapter 2. Figure 3.1(b) shows the experimental distribution of normalized $u_z$ behind the GRIN PC at the moment when the overall maximum $u_z$ appears. The maximum value is found at $x = 23.5a$, at exactly the same position as the numerical results. Furthermore, the phase distribution of $u_z$ is in excellent agreement with the numerical counterpart. Therefore, very good accordance of focal distance is found between the distribution of ray trajectories, the simulations, and experiments.

We then investigated GRIN PCs with several lengths. Figure 3.2 shows the profiles of normalized maxima of $u_z$ along the central axis behind a GRIN PC with a length $L = 15a$ (a), $18a$ (b), $21a$ (c) and $24a$ (d), respectively. For both numerical (dashed lines) and experimental (solid lines) results, the peak values appear at $7a$, $4.5a$, $2.5a$ and 0 behind the of GRIN PC. Such a decreasing distance is expected since incident waves converge all the more as $L$ is large.

The focusing distance is however reduced in a large extendt, in comparison to the focal distance of $32a$ of the inner focusing at 5 MHZ described in chapter 2. One important reason, One important reason, as can be understood from the ray trajectories drawn in figure 3.1(a), is the wave refraction occurring at the exit interface between the GRIN PC and the background. The outgoing waves are refracted closer to the interface so that the focusing zone is shifted toward a shorter focal distance. Secondly, if the focus appears too close to the interface, the inhomogeneity of the PC can affect the field distribution of $u_z$, at least to an extend. As a result, when the GRIN PC takes a length $L = 24a$, the maximum value appears very close to the exit.

Experimentally, we measured the gain factors to be 2.04, 2.18, 2.20 to 2.44, in good agreement with the numerical outputs, namely 1.93, 2.12, 2.18 to 2.31. Such

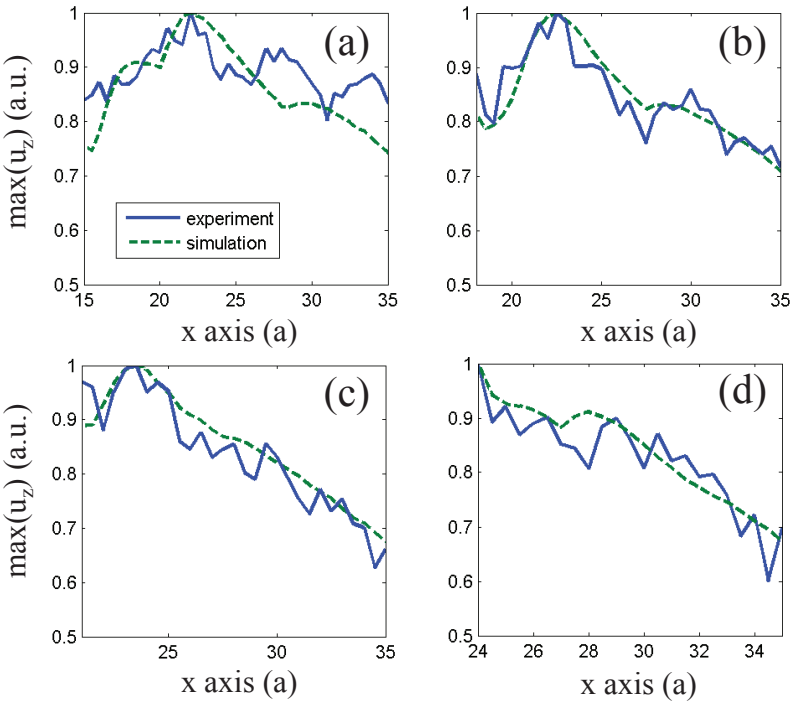


Figure 3.2: Numerical (dashed lines) and experimental (solid lines) maximum displacement profile along the $x$-axis for GRIN PC with (a) 15, (b) 18, (c) 21 and (d) 24 layers, respectively.

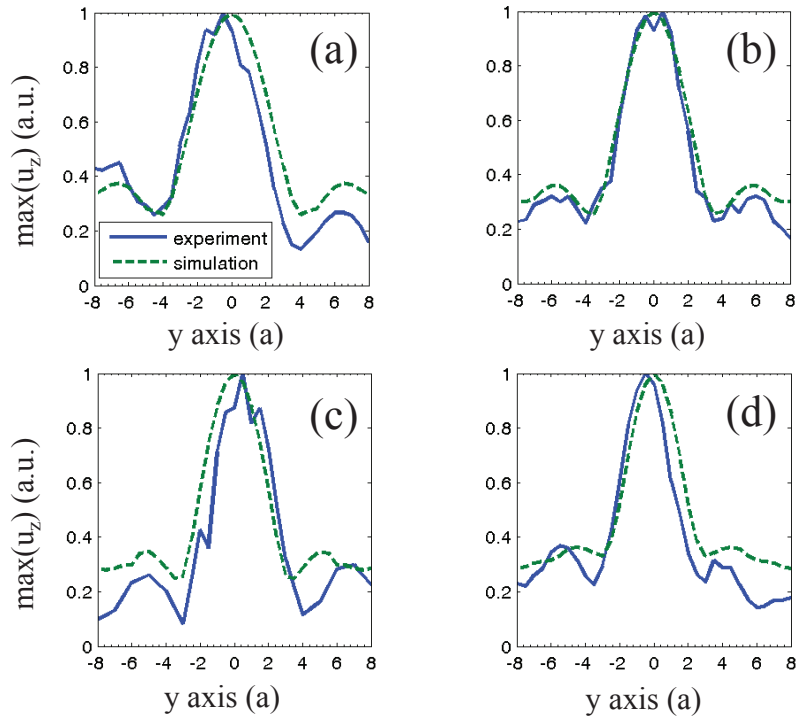


Figure 3.3: Numerical (dashed lines) and experimental (solid lines) maximum displacement profile along $y$-axis for GRIN PC with (a) 15, (b) 18, (c) 21 and (d) 24 layers, respectively.

an increasing trend of the gain factor is well explained if remembering that the waves are more convergent as $L$ increases.

Figure 3.3 shows the transverse profile of normalized maximum $u_z$ at the peak value for GRIN PCs with a length $L = 15a$ (a), $18a$ (b), $21a$ (c) and $24a$ (d), respectively. The numerical results (dashed lines) show a FWHM equal to $1.08\lambda_B$, $0.96\lambda_B$, $0.87\lambda_B$, or $0.82\lambda_B$ in turn, with $\lambda_B = 5.1a$ being the wavelength in the background. This agrees well with the fact that incident waves are more strongly converged for a larger $L$. The experimental results, on other hand, have given a FWHM $1.00\lambda_B$, $0.86\lambda_B$, $0.75\lambda_B$, and $0.72\lambda_B$, in good agreement with their numerical counterparts. Both the experimental results and numerical ones illustrate that a length $L$ large enough ($> 18a$) in needed in order to get the subwavelength focusing with a GRIN PC.

### 3.2.2 Discussion on limit of focusing outside GRIN PC

To explore the limit of focusing outside the GRIN PC, figure 3.4 shows the scheme of beam paths through a simplified GRIN PC of square symmetry. A monochromatic plane wave is normally incident from background medium to GRIN PC, resulting in a focusing zone on the unstructured plate at $L_0$ faraway behind output interface. Generally, only propagating modes with $|k_y| < |k_B|$ are excited at the exit with $k_B$ standing for the wavenumber in the background. In such a situation, it allows replacing the GRIN PC with an effective medium, because the working frequency is chosen within the first acoustic branch; high-order Bragg scattering processes are ignored.[39,93,102]

Inside this focus zone, the transverse wave number $k_y$ of the beams changes from $-k_M$ to $k_M$ with $k_M$ the maximum value of $|k_y|$. This is similar to an image of a point source. The transverse profile at the peak value becomes straight, and it is assumed to obey[9,25]

$$|U(x,y)| = \left| \int_{-k_M}^{k_M} exp\Big[ik_y y + i\sqrt{k_B^2 - k_y^2}(x - L - L_0)\Big]dk_y \right|, \quad k_M < k_B \qquad (3.1)$$

with $U(x,y)$ indicating the field intensity. Equation (3.1) evaluates the field intensity in a normalized way, and it cannot give a predication of the gain factor. However, one may evaluate the primary focus spot of such a transverse profile to be at full width $\Delta = 2\pi/k_M$, giving arise to a minimum feature size that is $\Delta/2$ (Rayleigh criteria).[9,25]

Figure 3.5 shows the transverse profiles (dashed lines) of $|u_z|$ derived from equation (3.1) with $k_M$ equal to $0.221\pi/a$, $0.250\pi/a$, $0.269\pi/a$ and $0.279\pi/a$ respectively. Profiles of the numerical results (solid lines) have their primary peaks in a position

in very good agreement with the theoretical predications. This shows that the resolution of focus is limited by $k_M$. It is worthy to notice that there is no imaginary wavenumber in this model, and thus the contribution of the evanescent components have not to be considered here.

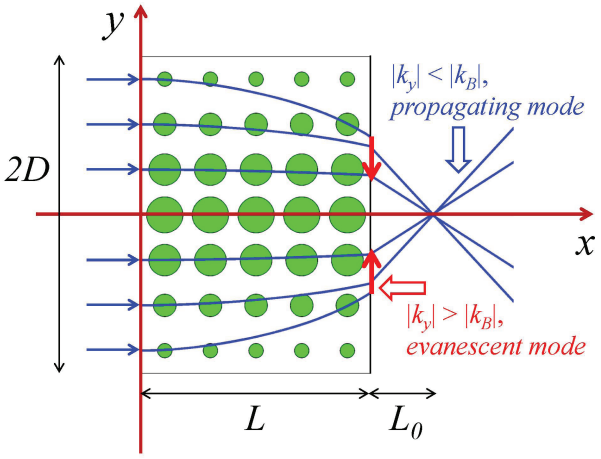


Figure 3.4: Scheme of a plane wave incident to a transverse GRIN PC.

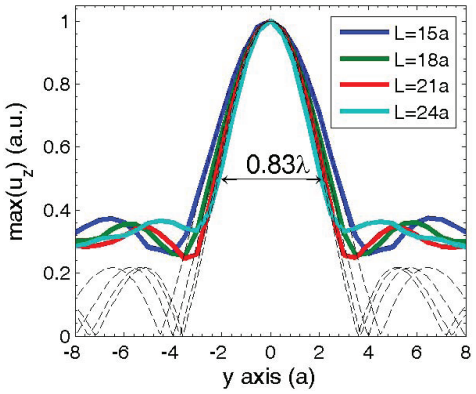


Figure 3.5: Numerical (solid lines) and theoretical (dashed lines) maximum displacement profile along $y$ axis for GRIN PC with 15, 18, 21 and 24 layers, respectively.

## 3.3 Theoretical predication to enhance focusing

Following the discussion in the previous subsection, naturally raises some questions: $(i)$ what is the resolution when $k_M$ is equal to or even larger than $k_B$? When $k_M$ is equal to $k_B$, the resolution will be close to half a wavelength according to equation (3.1) and $(ii)$ when $k_M$ is larger than $k_B$ while at the same time the focusing is limited to the near field, what will be the resolution at the focus? Many studies have been proposed to explore such near-field focusing, accounting both for the

propagating and for the evanescent modes.[9,103,104] However, few analytical solutions have been found due to the complex behaviors of the elastic field. It is assumed here that both propagating and evanescent modes give contributions at the same level in the near-field focus plane at $x = L+L_0$. It is then straight that, the focusing through GRIN PC is analogous to the image of a point source through a negative-index flat lens: at the exit of lens, both propagating and evanescent modes contribute to the formation of image. The transverse profile in the near-field, through negative-index lens applies directly to GRIN PC at the focus $x = L + L_0$ as[9]

$$|U(x,y)| = \left| \int_{-k_B}^{k_B} exp\Big[ik_y y + i\sqrt{k_B^2 - k_y^2}(x - L - L_0)\Big]dk_y + (\int_{-k_M}^{-k_B} + \int_{k_B}^{k_M})exp\Big[ik_y y + i\sqrt{k_y^2 - k_B^2}(x - L - L_0)\Big]dk_y \right|, \quad k_M > k_B \tag{3.2}$$

The primary spot of such a transverse profile features a value of $\Delta/2$ less than half a wavelength.[9,25] Indeed, the detailed focus pattern depends strongly on the interplay between propagating and evanescent modes.[9] Besides, the $L_0$ can be different for each beam path due to the Snell's law at the exit, which leads to aberrations. Despite these uncertainties, the focus can still be compensated by the evanescent modes to enhance the focusing resolution.

## 3.4 Physical model through resonant structures

### 3.4.1 Band structures of trampoline

To insure the relationship $k_M > k_B$, we elaborated a metamaterial featuring erected pillars on the surface in between adjacent holes in a PC slab,[105] as shown in figure 3.6. The benefits brought by this metamaterial, that we will name "trampoline" in what follows, will be presented later together with the thorough design of the GRIN PC.

We drilled air holes of radius $r_a$ with a square lattice of constant $a = 100$ $\mu$m through a silicon plate of thickness $h = 153$ $\mu$m. The silicon plate lies in $x-y$ plane and the thickness is along $z$-direction. The $x$-, $y$- and $z$-axes are parallel to the crystallographic directions of silicon $< 001 >, < 010 >$ and $< 100 >$, respectively. Arrays of identical silicon pillars of radius $r_p = 30$ $\mu$m and thickness $h_p = 65$ $\mu$m were erected on one side of the PC slab, located at the center in between air holes along $\Gamma$M direction. The transverse gradient is controlled by gradually modifying the radii of the air inclusions along $y$-axis.

Since investigating the negative elastic properties of this structure does not enter the scope of this work, the trampolines were seen as periodic structures rather than metamaterials. However, one should mention that, besides their relevance for acoustical lenses, they are very promising structures in what concerns the acoustical cloaking and related effects. Figure 3.6(a) shows the band structures (dotted lines) calculated by FEM, of a trampoline with $r_a = 41.3$ $\mu$m. Three basic modes $A_0$, $S_0$ and $SH_0$ are noted according to their modal shapes in figure 3.6(a) with $A_0$ band highlighted by a solid line. For comparison, $A_0$ band of the same structure, but without the silicon pillars, is drawn as a dashed green line in figure 3.6(a). Clearly $A_0$ band of trampoline is down shifted to the low frequencies region.

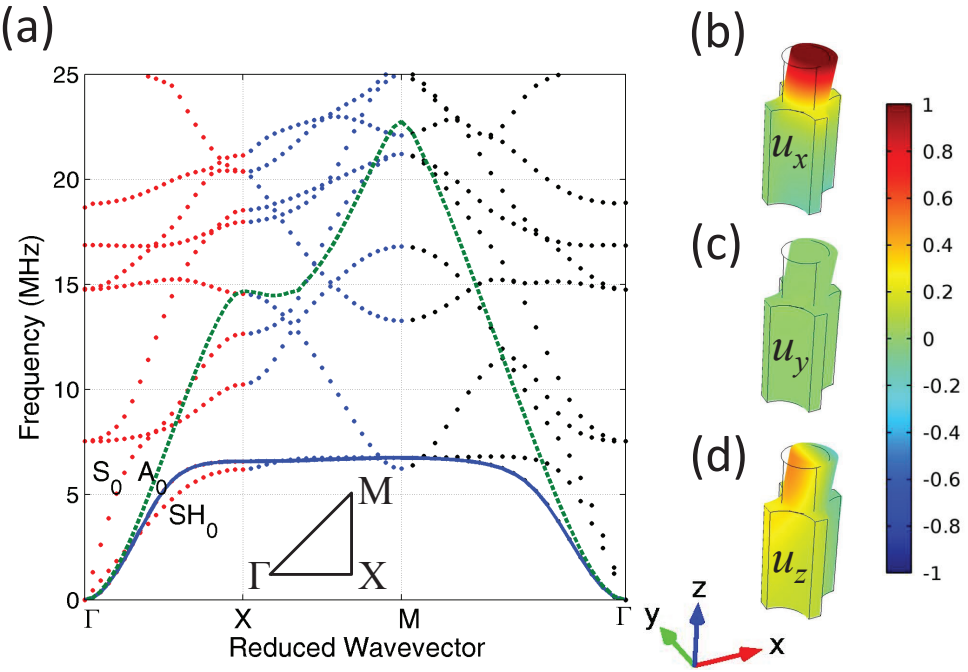


Figure 3.6: (a) Acoustic bands for a trampoline PC with $a = 100$ $\mu$m, $h = 153$ $\mu$m, $h_p = 65$ $\mu$m, $r_a = 41.3$ $\mu$m, $r_p = 30$ $\mu$m. Solid line and dashed line indicate $A_0$ mode bands of structures with and without silicon pillar, respectively. Normalized modal displacement of $A_0$ band of trampoline for (b) $u_x$, (c) $u_y$ and (d) $u_z$ along $\Gamma$X at $k_{\Gamma X} = 0.586\pi/a$. The modal deformation is also displayed in figures (b)-(d) in comparison to the initial shape of trampoline noted by solid lines.

Figure 3.6 shows the modal displacements normalized to the same scale for $A_0$ mode of trampoline along $\Gamma$X at $k_{\Gamma X} = 0.586\pi/a$ (frequency $f = 5.9$ MHz) for (b) $u_x$, (c) $u_y$ and (d) $u_z$, respectively. We showed also the modal deformation in comparison to the initial shape of trampoline as noted by the solid lines in figures 3.6(b)-(d). The silicon pillar, together with the substrate composed of air/silicon PC, is polarized within $x - z$ plane. The polarization of the displacement field associated to the pillars shows that the bending mode of the pillar well accounts

for the large shift of $A_0$ mode bands between the two structures, with and without the pillars.

As the frequency increases, the trampoline is all dominated by the low-order bending vibration of the silicon pillar with $u_x$ dominating the displacement field, so that $A_0$ band is down shifted and becomes flat along both ΓX and ΓM.

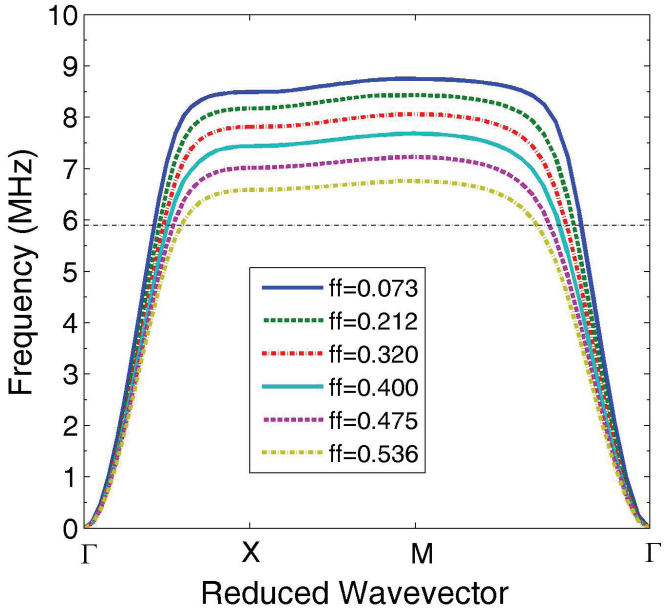


Figure 3.7: $A_0$ bands of trampoline PC with different filling ratios (ffs) determined by $\pi(r_a/a)^2$.

### 3.4.2 Design of GRIN PC

Figure 3.7 shows $A_0$ bands of trampolines with different filling ratios (filling ratio $ff = \pi(r_a/a)^2$). The frequency of the flat section in these bands decreases gradually as the filling ratio increases. In the computations, the GRIN PC was designed for the wavenumber along ΓX to have a hyperbolic secant profile

$$k_{\Gamma X}(y) = k_{\Gamma X0}\mathrm{sech}(\delta y), \tag{3.3}$$

where $k_{\Gamma X0}$ is the value of $k_{\Gamma X}$ along the central layer. The geometric constants $a$, $h$, $h_p$ and $r_p$ keep the same values as before with $D = 8a$. To underline the advantages of the trampoline structure, let us temporary neglect the anisotropy of the GRIN PC and let the lens being infinite along $x$-axis. When the wave beam is

focused on the central layer, the wavenumber reads

$$\begin{aligned} |k_y| &= \sqrt{k_{\Gamma X0}^2 - k_x^2} \\ &= k_{\Gamma X0}\sqrt{1 - \mathrm{sech}^2(\delta y_0)} \end{aligned} \tag{3.4}$$

with $y_0$ the position along $y$-axis where the wave is impinging the GRIN PC. One finds:

$$k_M = k_{\Gamma X0}\sqrt{1 - \mathrm{sech}^2(\delta D)}. \tag{3.5}$$

Now consider a focusing of the beam behind the GRIN PC as shown in figure 3.4. Owing to the conservation of $k_y$ (Snell's law), the relationship between $k_{\Gamma M}$ and $k_{\Gamma X0}$ on the interface between the GRIN PC and the background reads:

$$k_M \leq k_{\Gamma X0}\sqrt{1 - \mathrm{sech}^2(\delta D)}. \tag{3.6}$$

In comparison to $k_B$, it requires a large $k_{\Gamma X0}$ and a large $\delta$ to get $k_M > k_B$.

Many other resonant structures, such as periodic membranes,[106] soft stubs,[107] or soft-layer-coated stubs,[108,109] allow for the $A_0$ mode branch to be shifted to lower frequency in an overall behavior,[110] as do the silicon pillars. This can be explained by a cantilever beam,[110,111] or a spring-mass model.[32] On the other hand, due to the weak rigidity of the membranes, the softness of stubs, or the softness of coated layer, $A_0$ bands of these structures are separated into several individual curves which tend to be flat at certain $\mathbf{k}$ vector in the first Brillouin zone by the local resonances of resonators, instead of being overall shift to lower frequency. This can be explained to some extend by the spring-mass model: for the given mass, a weak spring constant will decrease the resonant frequency, as what happens to resonators of weak rigidity. On the other hand, for a given spring constant, if we increase too much the mass (e.g. thickness of pillars), the $A_0$ bands will also be separated into several flat bands, as what finds in previous studies.[110,112]

The air holes in the trampoline lead to further down shift of $A_0$ band in a behavior similar to springboards, resulting in enlarged $k_{\Gamma X}$ at a given frequency.[105] This amplification phenomenon is graded for the GRIN PC with the maximum amplification appearing at the central layer while the minimum one appears at the lateral layers: at 5.9 MHz, the ratio of $k_{\Gamma X}$ between structures with and without pillars is 1.30 at $y = 0$ or 1.09 at $y = \pm D$, which leads to an enlarged $\delta$. These values allow confirming that the trampolines are indeed advantageous structures to design a GRIN PC.

Before further calculations, it is crucial to analyze the ultimate resolution one

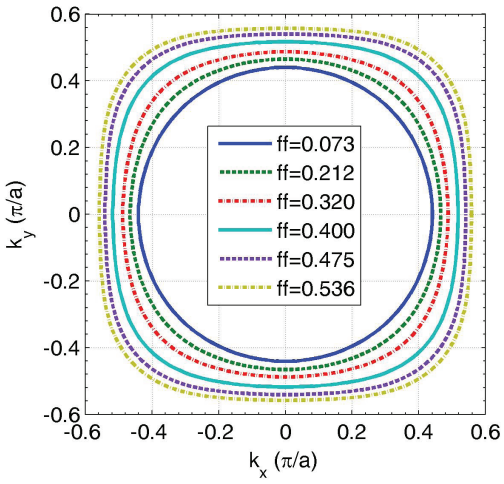


Figure 3.8: The fitting curves of EFCs for different filling ratios.

could expect. To this end, one states that $k_M$ satisfies:

$$k_M < k_{\Gamma X0} \leq \pi/a, \tag{3.7}$$

as derived from equation (3.6) in the first Brillouin zone. Therefore, if ignoring the local anisotropy in the GRIN PC, one gets:

$$\Delta = 2\pi/k_M > 2a. \tag{3.8}$$

Equation (3.8) means that the focusing of the positive-index lens is limited by the periodic constant to be $2a$. Such a value is also the minimum size for one of the negative-index photonic/phononic crystal lens.[9]

For frequencies in the upper part of $A_0$ band, the transmission of the wave from the GRIN PC to the background may be hindered because of the large impendence mismatch. Compromise frequencies shall be chosen in order to have both a large value for $k_M$ and a relatively large transmission. In the present case, 5.9 MHz is a good compromise frequency. We show in figures 3.6(b)-(d), the normalized modal displacements along $\Gamma X$ ($k_x = 0.586\pi/a$) $u_x$, $u_y$ and $u_z$, respectively, computed at 5.9 MHz for $ff = 0.536$. The displacement field $u_z$, which is essentially related to $A_0$ mode, has an amplitude about 1.5 time larger in the pillar than in the matrix. This makes it possible to transmit the elastic energy attached to the propagating mode, from the PC to the background. As for the evanescent modes, their behavior at the output interface will be described in detail bellow. The optimized parameters for the GRIN PC were finally $\delta = 0.107a^{-1}$, $k_{\Gamma X0} = 0.588\pi/a$ ($r_a = 41.3$ $\mu$m), and $k_B = 0.381\pi/a$. The ray trajectories, together with the wavenumbers $k_x$ and $k_y$, were calculated using the formalism introduced in chapter 2. Figure 3.8 shows the

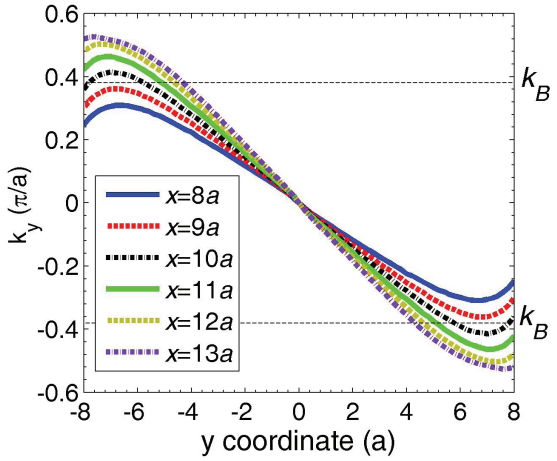


Figure 3.9: Number of $k_y$ at different position $x$ inside GRIN PC before the first focus.

EFCs of a PC with different filling ratios at 5.9 MHz. In comparison to the EFCs at the working frequency of 5.9 MHz calculated in chapter 2 (for a GRIN PC without pillars), the EFCs of the resonant structures are larger.

To determine the optimal length $L$ of GRIN PC, we have computed the value of $k_y$ at different positions inside the heterostructure before the first focus (figure 3.9). $k_M$ can be larger than $k_B$ when $L$ is larger than $9a$. With such a value of $L$, evanescent modes are expected to arise at the output interface between the GRIN PC and the background. In the following, $L$ is set as $11a$ in order to have a large $k_M$ ($k_M = 0.47\pi/a$) while at the same time a value of $L_0$ large enough to detach the focusing from the GRIN PC. Accordingly, the GRIN PC is designed to have 11 columns of air holes with identical pillars erected on one side of the plate

## 3.5 Focalization through resonant structures

### 3.5.1 Focalization of $A_0$ mode behind the GRIN PC: Numerical results

Numerical simulations using FEM were performed by placing a line source in front of GRIN PC to excite $A_0$ Lamb mode at 5.9 MHz.[66] The normal component $u_z$ was then recorded on a part of the plate free of pillars. We can also record numerically $u_z$ on the surface with pillars. However, experimentally, this is not doable at the inner of the GRIN PC. The displacement field may be highly concentrated at the feet of pillar, which may be not favorable to demonstrate the homogenized behavior of the GRIN PC.

We show in figure 3.10(a) a snapshot and 3.10(b) the normalized maxima of $u_z$

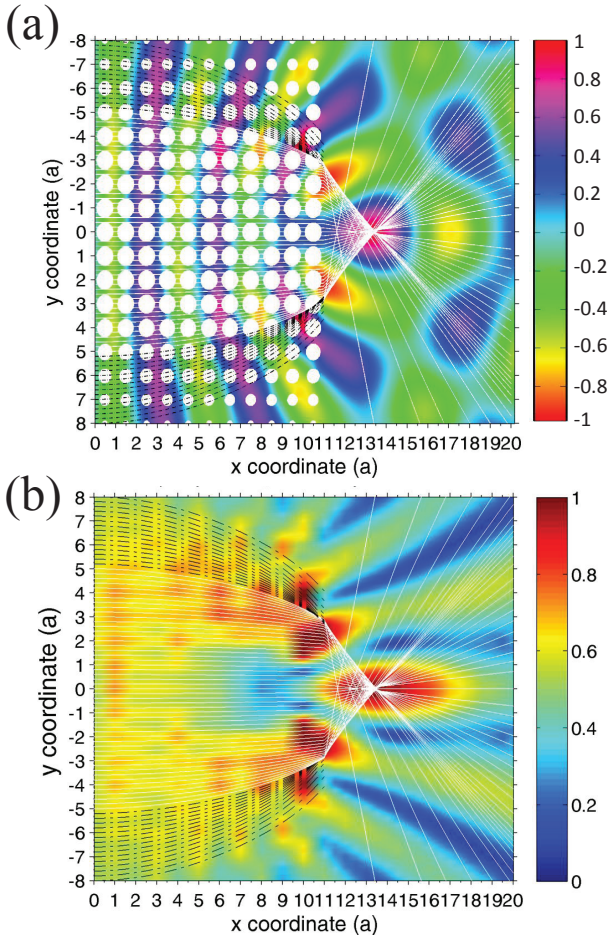


Figure 3.10: (a) Snapshot of numerical displacement $u_z$ and (b) normalized maximum $u_z$ both inside ($x = [0,\ 11a]$) and outside ($x = [11a,\ 20a]$) GRIN PC. The solid lines indicate ray trajectories of wave beams with a $|k_y| < k_B$ at exit of GRIN PC ($x = 11a$); the solid lines illustrate ray trajectories of wave beams with a $|k_y| > k_B$ at exit of GRIN PC. Accordingly these beams are no more propagating modes and ray trajectories shall not be sufficient after the exit where no ray trajectory is presented for these wave beams.

both at the inner and behind the GRIN PC. The overall maximum of $u_z$ appears at $L_0 = 2a$ ($0.38\lambda_B$, $\lambda_B = 5.25a$) behind the GRIN PC. The calculated ray trajectories can be divided into two groups: solid lines are for wave beams with $|k_y| < k_B$ at the exit of GRIN PC ($x = 11a$) while dot dashed lines are for those with $|k_y| > k_B$. Evanescent modes with imagery $k_x$ are expected to appear for those waves for which no ray trajectories are presented behind the interface. The ray trajectories for propagating modes predict a focus zone located at a position in good agreement with the numerical results.

In figure 3.10(b), the transverse profile at the peak value corresponds to FWHM of $0.44\lambda_B$, or a Rayleigh criteria $\Delta/2 = 0.37\lambda_B$ when fitted by the *sinc* function. This is very close to the Rayleigh criteria derived from equation (3.2), namely $0.41\lambda_B$. Obviously, both FWHM and Rayleigh criteria are smaller than half a wave-

length and therefore the super-resolution is predicted by our numerical simulations.

The above results mean also that, as predicted before, both propagating and evanescent components make their own contributions to this small focus zone. A density maximum is formed and the transverse profile at the peak value corresponds to a resolution less than half a wavelength: the *moderate* subwavelength pattern described by Luo *et al.*[9] is achieved numerically in the time domain.

At the focus, the amplitude of the normal displacement $u_z$ is about 1.9 times that of the incident wave. This gain factor is a little smaller than already observed in former studies.[71,77] This is mainly caused by the reflection of the propagating waves close to the symmetry axis ($y = [-2a,\ 2a]$). However, it still provides useful suggestions to enhance the transmission of the wave compared with previous studies.[23,96]

### 3.5.2 Focalization of $A_0$ mode behind the GRIN PC: Experimental results

Samples were fabricated according to the designs described before and we used the laser-based technique both to excite quasi-monochromatic $A_0$ Lamb mode and to measure the out-of-plane displacements. A series of lenses allowed to form on the surface of the sample, an image of a grating and to get optical fringes spaced at a distance of an acoustical wavelength from each other. The corresponding acoustical frequency was centered at 5.9 MHz. We show in figure 3.11 (a) a snapshot and (b) the normalized maxima of $u_z$ behind GRIN PC. During the data process, we used a very narrow Gaussian window centered at 5.9 MHz to filter the signal. The maximum of $u_z$ is found at $x = 13.7a$ or $2.7a$ ($0.51\lambda_B$) behind the interface GRIN PC / substrate. This value is slightly more than what is predicted both by ray trajectories computations and numerical results. The transverse profile at the peak value in figure 3.11(b) gives a FWHM of about $2.79a$ or $0.53\lambda_B$. Such a focusing resolution, although not surpassing the diffraction limit, is actually very close to half a wavelength and even is smaller than certain results of acoustical image using negative-index PC for $A_0$ mode.[34]

We show in figure 3.12 the SEM image of (a) the overall sample and (b) one pillar on the PC slab. Uniform silicon pillars were well erected on the surface. However, unexpected defects (resin, plasma hot spots, etc) appear here and there, which can affect to some extent the overall performances of the GRIN PC. Moreover, the actual diameter of the air holes along some rows may slightly differ from the nominal value, affecting in turn the achievements of the GRIN PC. Indeed, the center of the experimental transverse profile is shifted by $0.75a$ from the central axis of the lens. This means that the sample is not exactly symmetric. This is clearly visible on the

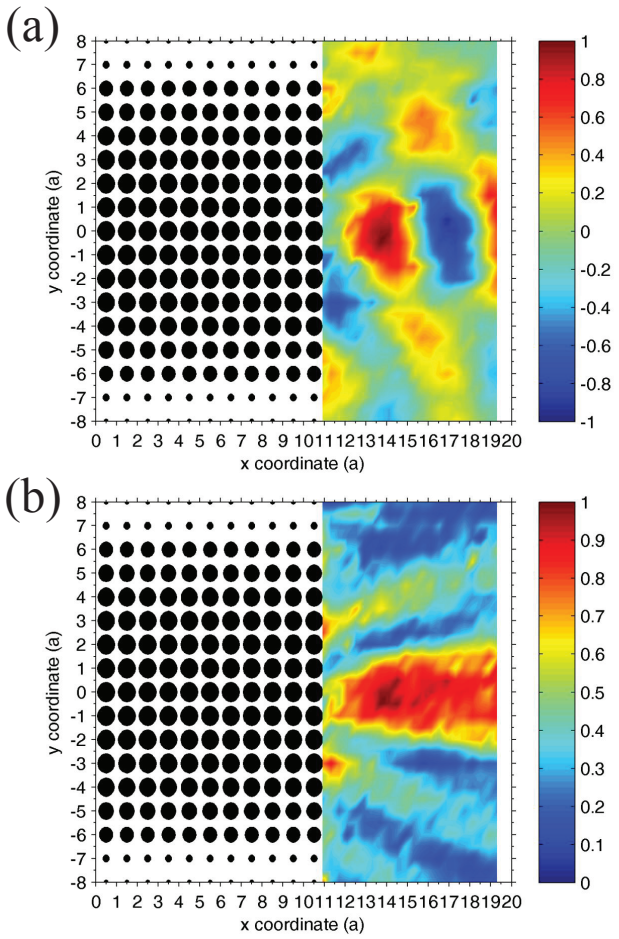


Figure 3.11: (a) Snapshot of experimental anti-plane displacement $u_z$ and (b) normalized maximum $u_z$ outside ($x = [11a,\ 20a]$) GRIN trampoline PC. The black holes indicate the designed size and position of air holes on the silicon plate.

snapshot of $u_z$ in figure 3.11(a). As a consequence, the resolution at the focus is less than expected.

One should also remember our experimental technique involves elastic pulses and not continuous waves: in the present case, the pulse comprised typically eight periods and therefore the experimental data could be affected by non-harmonic effects. On the other hand, because of transient effects, it takes some time for the "steady state" to be attained.[25] To illustrate this, we show in figure 3.13 the transverse profile (square markers) at the focus at the moment when the overall maximum $u_z$ is reached, together with the profiles derived from the numerical simulations (solid line) and theoretical predications by equation (3.2) (dashed line). At the outcomes of the numerical simulations, the theory and the experiments, we found the transverse profile $\Delta/2$ to be about $0.33\lambda_B$, $0.41\lambda_B$ and $0.46\lambda_B$, respectively. Any of these values is less than half a wavelength and hence the super-resolution is confirmed. The FWHM is $0.42\lambda_B$, $0.49\lambda_B$ and $0.52\lambda_B$ for the three methods, respectively. Al-

though not surpassing the diffraction limit, the experimentally measured FWHM is actually very close to it.

The maximum value (2.22 pm) is about 2.36 times that of the amplitude of the incident waves (0.94 pm). This gain factor is slightly larger than the value obtained by FEM, namely $\sim 1.9$. Note also that, as a general trend,[96]: the larger the gain factor is, the worse the resolution we get.

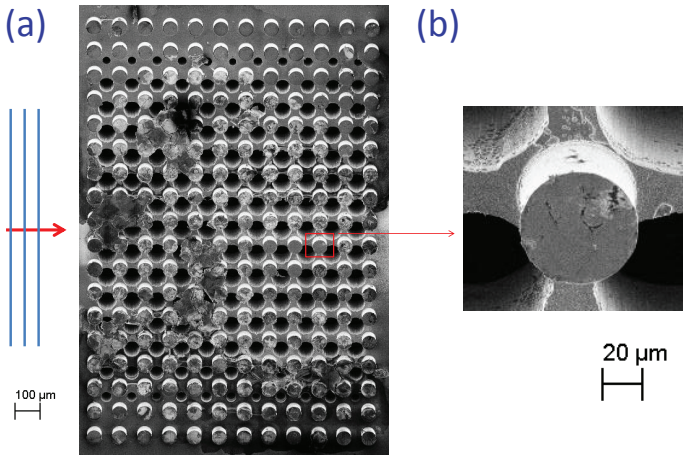


Figure 3.12: SEM image of (a) the overall sample and (b) one silicon pillar on the PC slab.

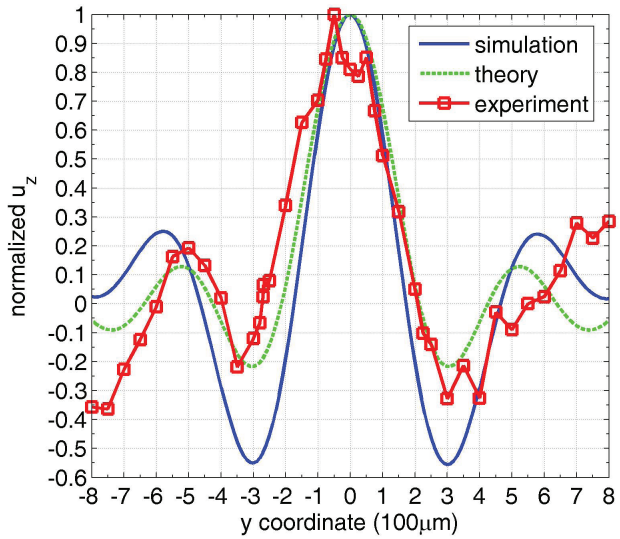


Figure 3.13: Normalized transverse profile of out-of-plane displacement $u_z$ at the focus at a moment with peak value obtained through simulation (solid line), theory (dashed line) and experiments (square markers).

It is interesting to carry out a 2D Fourier transform of both the numerical and the experimental data recorded within the focusing zone, in order to get information

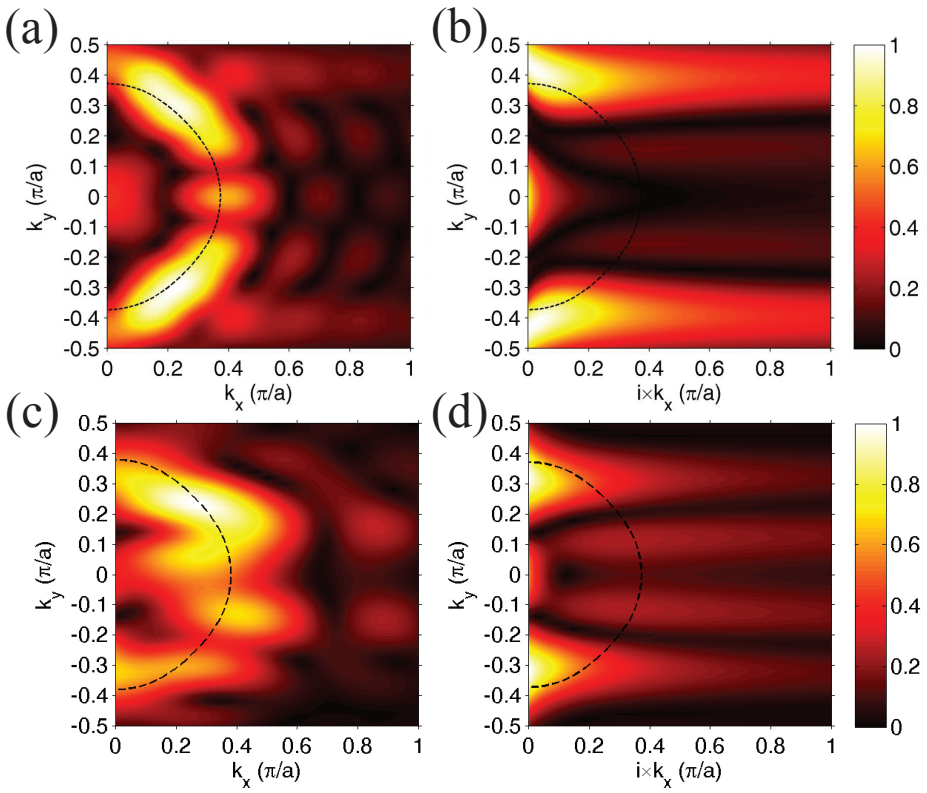


Figure 3.14: Fourier transform of the numerical snapshot of focusing at $x = [11a,\ 21a]$ in (a) real component space and (b) imaginary component space; Fourier transform of the experimental snapshot of the focusing at $x = [11a,\ 19a]$ in (c) real component space and (d) imaginary component space. In all the figures, dashed line .

in the reciprocal space.[30,113,114] We proceeded so with the data displayed in figures 3.10(a) and 3.11(a). The real part and the imaginary part of the Fourier components of the numerical results are shown in figures 3.14(a) and 3.14(b) respectively. A succession of symmetric spots is found all along the EFC at 5.9 MHZ in the background (dashed line). These bright zones correspond to high density of elastic energy and delimits the main streams for the elastic flux. The amplitude of the signal is weak for $k_y = [-0.1\pi/a,\ 0.1\pi/a]$, which is coherent with the strong reflection of the wave at the interface in the central area of the GRIN PC. If $|k_y|$ is larger than $k_B$, the $k_x$ turns to be an imaginary number, as shown by the Fourier transform in figure 3.14(b). Symmetric main spots are found at $|k_y| = [0.38\pi/a,\ 0.5\pi/a]$, in good agreement the theoretical range $|k_y| = [0.38\pi/a,\ 0.47\pi/a]$ deduced from the theoretical analysis described above and summarized in figure 3.9.

From the experimental side, the main spots in figure 3.14(c)spread asymmetrically along the EFC in the **k** vectors space. This well agrees with the statement that the sample is asymmetric. When considering the imaginary part of the Fourier transformed data, one can see that $|k_y|$ is almost always less than $k_B$. Accordingly, the FWHM is just at the limit of diffraction. We attribute the disagreement be-

tween our numerical and FEM results to some inhomogeneities or defects in the samples, as can be observed in the SEM image in figure 3.12.

To finish this section, let us notice that in our model, the evanescent components only appear at the interface during the transmission from the GRIN PC to the substrate. Therefore, for the sub-wavelength focusing of $A_0$ mode to occur behind the trampoline structure, neither the negative refraction process is involved nor is it necessary to satisfy the all-angle negative refraction (AANR) condition, which is quite different from other works. Let us notice also that, *a priori*, the focusing achievements of the trampoline structure should depend on the polarization of the elastic waves and therefore we need attach the same pillar on both sides of the PC slab if considering symmetric Lamb waves instead of $A_0$ Lamb mode.

### 3.5.3 Physical explanations

A question naturally arising is how the evanescent modes are able to get to the background medium? To answer this question, let us go back to the actual structure of these artificial media instead of viewing them as effective materials. We considered a six units crystal attached on one side to a large silicon plate, as shown in the inset in figure 3.15. Periodic conditions were applied on the lateral sides of the slab, and the bands structure was computed as shown by the dotted lines in figure 3.15.[25] $A_0$ bands of both the silicon plate (dot-dashed red line) and the trampoline (solid green line) are displayed in the same figure.

$A_0$ mode in the silicon plate features similar properties as the *sound line* in fluids,[23,90] and separates dotted curves into two parts: the propagating modes in the shaded region with $|k_y| < k_B$, and the modes bounded to the trampolines below the dot-dashed line with $|k_y| > k_B$. These bounded modes correspond to $k_x = i\sqrt{k_y^2 - k_B^2}$ being imaginary, and therefore the displacement field decays from the trampoline to the background.

At the edge of the first Brillouin zone, just above the $A_0$ band of the trampoline, some bound modes are converging. The corresponding branches become flat due to the bending vibration of the pillars, and large transverse wavenumber $|k_y|$ may be expected.[9] The bending mode of the silicon pillars is coupled to the $A_0$ mode of the silicon plate, as illustrated by the modal displacement in figure 3.6 (b-d). Such a close coherence between the resonant behavior of the silicon pillars and the vibrating modes in the silicon plate, indeed, allows the structure working towards the desired direction: enhancing the transmission of the evanescent components through the bound modes. The operating frequency of 5.9 MHz being quite close to the frequency of the flat bounded modes, and the quality factor of the resonant bending mode being low,[92] the amplitude of evanescent modes at the interface

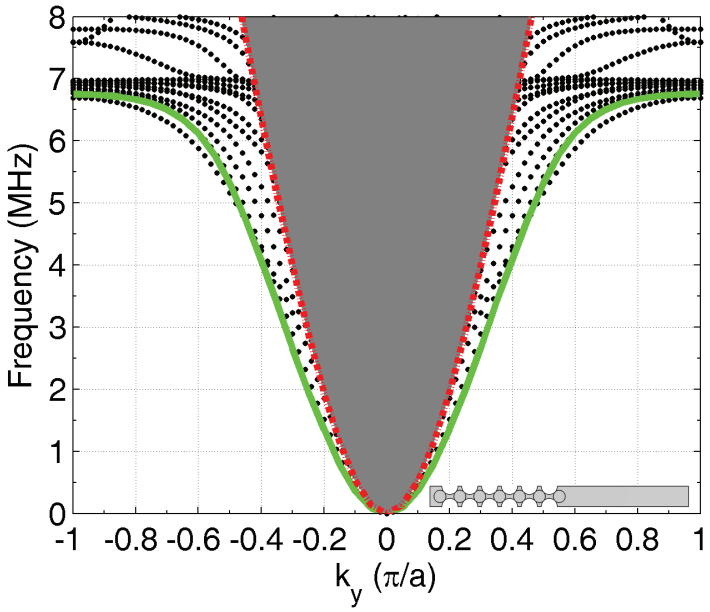


Figure 3.15: Band structures of a six-layer crystal (see inset label) along the interface direction ΓY. Radius of air holes keeps the same value of the central layer of GRIN PC with $r_a = 40.5$ $\mu$m. $A_0$ mode band of silicon plate is superposed in the figure noticed by the dot-dash line, as well as the $A_0$ mode band of trampoline presented by the solid line.

between GRIN PC and background is enhanced.

To further investigate the relationship between the bending vibration of the pillars and the bounded modes, special attention was paid to the local behaviors in the two last rows of inclusions (holes + pillars). As could be seen from the ray trajectories in figure 3.10, incident waves are concentrated into a limited region at the exit layers, exciting the pillars into their normal bending mode. Let us now consider the reverse situation where the pillars are driven into their bending mode by an external source, along the direction given by the ray trajectories in figure 3.10. However To simplify, we consider only the two last columns of air inclusions with silicon pillars inserted in between (figure 3.16(a)).

Forces are applied on the top surface of pillars at $y = 3.5a$ $(-3.5a)$, polarized in the $x - y$ plane, with an angle $-0.26\pi$ $(0.26\pi)$ with respect to $x$-axis. This corresponds to both the position and the tangent to the trajectory at the interface of the sample where $|k_y| < k_B$ (see figure 3.10). Figure 3.16(b) shows the normal displacements $u_z$ when only the pillar at $y = -3.5a$ is excited. The displacement field at $x < -2a$ are not shown since only the forward field is of interest. In the near filed, waves are found to propagate along the interface between the unit layer and the silicon plate with decreasing amplitude along $x$-direction, as expected for waves featuring an imaginary $k_x$. This means that the bounded modes can be efficiently excited by the bending mode of the pillars. Such efficiency comes probably from the

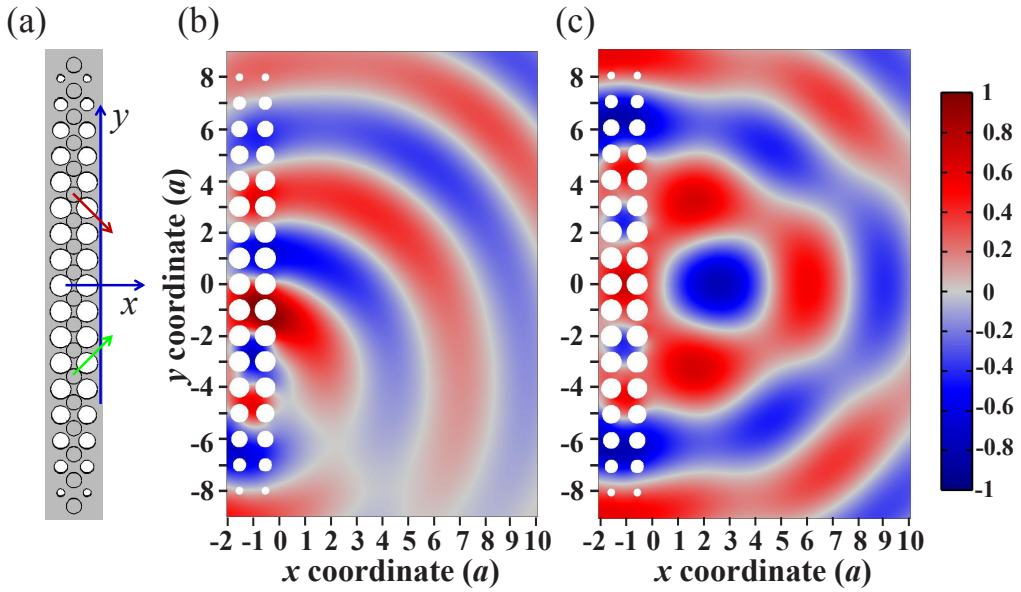


Figure 3.16: (a) scheme of column of GRIN PC with force source applied on two symmetric pillars both along $x$ and $y$ coordinates with an angle indicated by arrows ($0.26\pi$). Snapshot of $u_z$ when (b) only the pillar at $y = -3.5a$ is excited and (c) pillar at $y = \pm 3.5a$ is excited.

coherence between the vibration mode of the resonator and that of the silicon plate. Knowing whether such coherency can be extended to other polarized waves still needs further discussion. Besides, the periodicity of the sub-wavelength apertures of air holes may also help, to a certain extent,[37] the transmission of the evanescent mode.

Figure 3.16(c) shows the snapshot of $u_z$ when both pillars at $y = \pm 3.5a$ are excited into vibration. A focus spot is formed at the position $2.6a$ faraway from the interface while the transverse profile gives a FWHM of about $0.46\lambda_B$ and a $\Delta/2$ of $0.36\lambda_B$. This shows that a focus zone can be observed in the near field for wave with $|k_y| > k_M$ owing to the excitation of bounded modes. The near-field focalization after the exit of GRIN PC, indeed, can be seen as the integral of waves beams with different values of transverse wavenumber as presented by equation (3.2).

## 3.6 Conclusion

Following the work described in the previous chapter, we used here a *conventional* GRIN PC to investigate the focusing *outside* the structured part of the lens. With the help of both the ray trajectories analysis and numerical results, it is found that the position of the focus can be accurately predicted, and that the resolution at the focus is enhanced for GRIN PC with larger length. Through the analysis of transverse wavenumber $k_y$, it is found that the resolution is limited by the maximum

value of $k_y$ at the exit.

In order to enhance the resolution at the focus, a resonant structure was used as the basic unit to design the GRIN PC. The bands structure shows that the bending resonant mode of the pillar-based PC allows to shift $A_0$ Lamb mode to lower frequency. This property helps the GRIN PC to exhibit larger variations of the refractive index. By tuning the width of the GRIN PC along $y$-axis, it is found theoretically that $k_M$ may be larger than $k_B$, leading to evanescent components of the transverse wave vector at the interface. Following the theoretical predictions, numerical simulations of the wave propagation in the GRIN PC gives the focusing at the expected position. The resolution at the focus, evaluated either by FWHM or by the Rayleigh criteria $\Delta/2$, is less than half-wavelength: the super-resolution is observed numerically. The gain factor is measured to be 1.9, a little less than the counterpart in chapter 2.

For comparison with the numerical simulations, samples with the same design as for the numerical study have been elaborated. The experimental results give a focal length a few longer than predicted by the numerical simulations. The resolution at focus, evaluated by FWHM, is $0.53\lambda_B$, just above half-wavelength. However, at the moment when the maximum $u_z$ appears, the focus features $\Delta/2 = 0.46\lambda_B$, less than half-wavelength. The experimental resolution is larger than the numerical one but still remains very close to the limit of diffraction. The experimental gain factor being about 2.36 is larger than computed, but at the cost of resolution.

To get a picture of the local processes at the origin of the global behavior, we have calculated the bounded modes. We found that they couple to the evanescent modes at the interface with the silicon substrate. The bending resonances of the pillars act as a bridge connecting the bounded modes to the evanescent transverse waves, which has been numerically verified through the excitation of the pillars by an external source.

# Chapter 4

# Focalization of a Rayleigh wave inside and outside a GRIN PC

## 4.1 Introduction

In both the preceding chapters, we have investigated the focusing of $A_0$ Lamb mode both at the inner and behind the GRIN PCs. With the help of the ray trajectories, as well as the numerical and experimental results, we have understood the influence on the focusing achievements, of the anisotropy along certain lines of inclusions. We have identify some key parameters to enhance the focusing resolution behind the GRIN PCs. We are quite confident that the formalism allowing to compute the ray trajectories can be easily extended to other types of waves. However, if we wish applying our method to other waves, we may encounter some new physics inherent to these waves. This is one of the most important reasons why we turned our attention to the focusing of Rayleigh waves in GRIN PCs engraved on a semi-infinite solid for which there are few experiments available to now.[75]

We applied the same methodology to design the GRIN PC as we did previously, *i.e.*, by adjusting in a controlled manner the sub-wavelength unit in order to get a graded transverse velocity.[75] In contrast to $A_0$ mode, the Rayleigh waves have their amplitude evanescently decreasing along the direction perpendicular to the free surface, to being almost zero at one-wavelength depth. Such a property makes the velocity of a Rayleigh wave gradually varying against the depth of the air inclusions, until a fixed value when the depth gets larger than one wavelength.[115,116] Therefore to have a large gradient for the refractive index, we must consider the influence of the depth of the inclusions.

In this chapter, we designed the GRIN PC by using the air/silicon structures. We studied the focusing of Rayleigh wave both at the inner and behind GRIN PCs. Features of wave focusing were revealed with the help of ray trajectories and

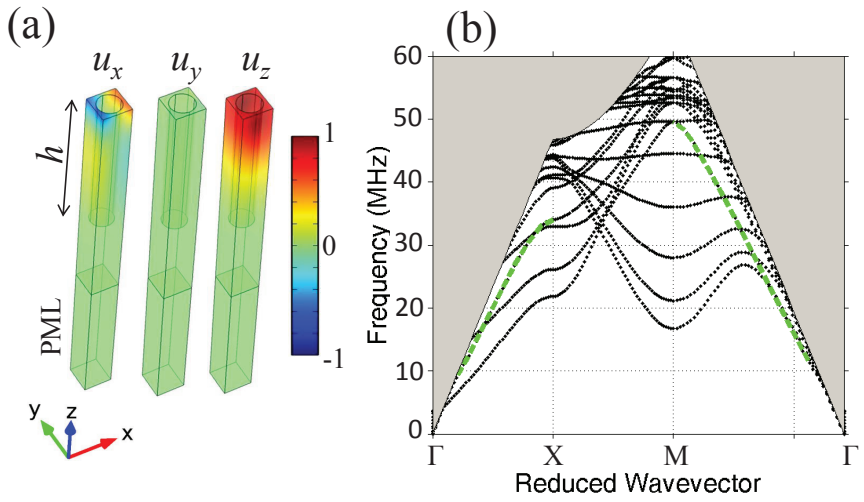


Figure 4.1: (a) Scheme of square-lattice unit cells with a periodic constant $a = 50$ $\mu$m, the radius of air hole $r = 20$ $\mu$m and the thickness of air hole $h = 250$ $\mu$m, in a semi-infinite substrate of silicon. (b) Band structures of the PC below the sound line with the bands of Rayleigh wave highlighted by the green dashed lines along ΓX and ΓM. The field of modal displacement normalized to the same scale is shown for Rayleigh wave at 20 MHz along ΓX. The $x$, $y$, and $z$-axis are parallel to the crystallographic directions $< 100 >$, $< 010 >$ and $< 001 >$, respectively.

experimental results. Meanwhile, the focus pattern was compared between Rayleigh wave and the $A_0$ Lamb mode.

## 4.2 Physical model

### 4.2.1 Band structures of Rayleigh wave

We started our studies by analyzing the bands of Rayleigh wave for PCs. To this end, FEM was applied to obtain the band structures for a PC constructed by drilling air holes in a silicon substrate. Figure 4.1(a) shows the scheme of the square-lattice unit cells with a periodic constant $a = 50$ $\mu$m, the radius of air hole $r = 20$ $\mu$m, and the thickness of air hole $h = 250$ $\mu$m. To mimic the semi-infinite substrate, we enlarged a little the thickness of the unit cells and we attached perfect match layers (PMLs) to the bottom of the unit cell.[117,118] Figure 4.1(b) shows the bands structure of the PC. They are separated into two parts by the so called *sound line*: the dotted black lines stand for the possible leaky/radiative modes to the substrate, whereas the shaded area indicates the opposite cases.[90] The *sound line* is determined by the smallest phase velocity in the semi-infinite solid for any propagation direction.[119] The slowness curves[78] show that the sound line is determined by the velocity of the shear-vertical (SV) wave along the $< 101 >$ direction, as shown in figure 4.2.

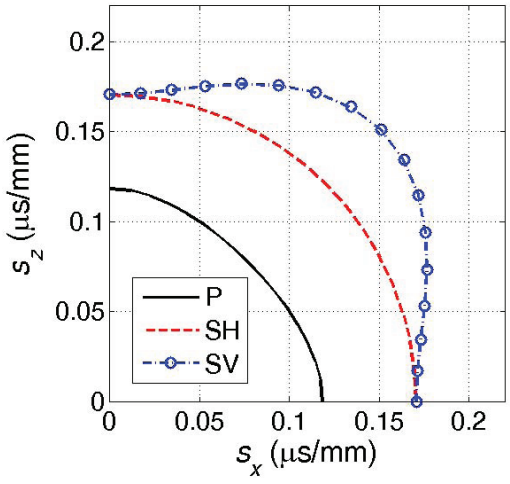


Figure 4.2: Slowness curve of the pressure (P) wave, shear-vertical (SV) and shear-horizontal (SH) wave of silicon. The $s_x$ and $s_z$ are parallel to the $< 100 >$ and $< 001 >$ of the crystalline direction of silicon, respectively.

The Rayleigh band is highlighted by the green dashed lines along ΓX and ΓM in figure 4.1(b). At 20 MHz, the Rayleigh wave has a wavenumber along ΓX $k_{\Gamma X} = 0.500\pi/a$, corresponding to a wavelength of 200 $\mu$m which is smaller than the thickness of air holes. Figure 4.1(a) shows also the fields of modal displacements normalized to the same scale at $k_{\Gamma X} = 0.500\pi/a$. The displacements are polarized in $x - z$ plane, extending over one-wavelength along $z$-direction. It should be noticed also that the normal component $u_z$ dominates over $u_x$ in the field of modal displacements.

### 4.2.2 Design of the GRIN PC

We repeated the calculation to find the Rayleigh bands for PCs with different filling ratios. These bands are found to decrease gradually as the filling ratio increases, as shown in figure 4.3(a). A GRIN PC was obtained by piercing air holes lattice of square symmetry on a silicon substrate, with the periodic constant $a = 50$ $\mu$m and a depth of holes $h = 250$ $\mu$m. The radii of the air holes change gradually along the transverse direction in such a way that the wavenumber $k_{\Gamma X}$ related to the Rayleigh waves obeys a hyperbolic secant profile

$$k_{\Gamma X}(y) = k_{\Gamma X0} \times \mathrm{sech}(\delta y), \tag{4.1}$$

where $\delta$ is the gradient coefficient, $k_{\Gamma X0}$ is the wavenumber along ΓX, within the central layer of PC. $k_B$ $(0.407\pi/a)$ stands for the wavenumber in the background along ΓX. The GRIN PC was designed to have $n_0 = 1.229$ and $\delta = 0.080a^{-1}$ at 20

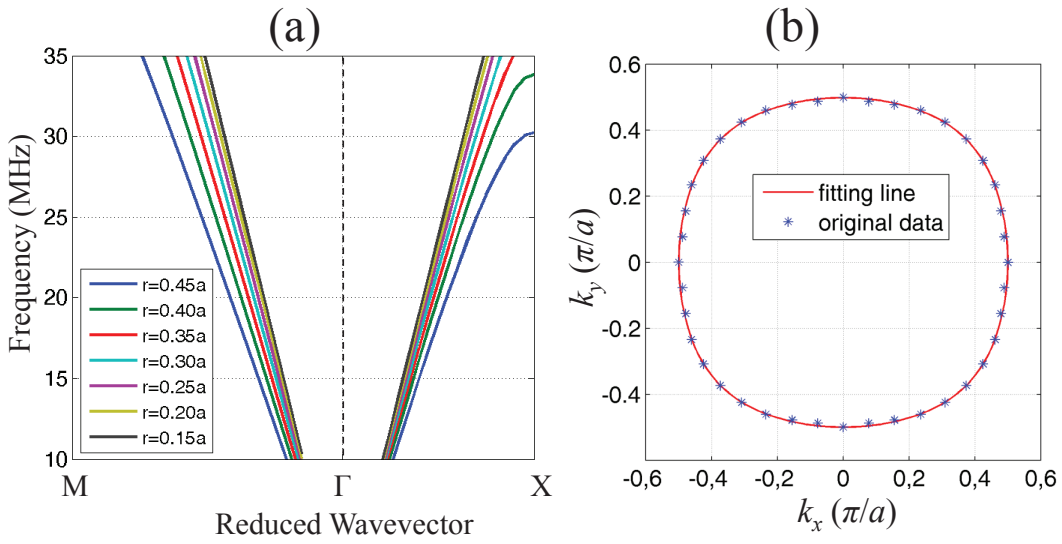


Figure 4.3: (a) Bands of Rayleigh wave in the first Brillouin zone with different radii of air holes. (b) Equal frequency contour at 20 MHz (star symbols) and its fitting curve with $r = 0.40a$.

MHz, and to insure this, the radii of the air holes changed gradually from 0.4a in the central row to 0.2a in the lateral rows.

The ray trajectories were calculated by using the same formalism as in chapter 2. To do this, the first step was to calculate the EFCs of the PCs. We show in figure 4.3(b) the EFC (star symbols) with $r = 0.40a$ at 20 MHz. The fitting curve (solid line) was derived from the formula

$$k(\theta) = k_{\Gamma X}\frac{1-\alpha\cos(4\theta)}{1-\alpha}, \quad \alpha = \frac{k_{\Gamma M}-k_{\Gamma X}}{k_{\Gamma M}+k_{\Gamma X}} \tag{4.2}$$

where $\theta$ is the angle between $\mathbf{k}$ and ΓX in in the first Brillouin zone. Excellent agreement is found between the two groups of results. The same comparison can be made for PC featuring different diameters of the air holes with as good an agreement.

## 4.3 Focalization inside the GRIN PC

### 4.3.1 Numerical results of Rayleigh wave focalization inside the GRIN PC

A GRIN PC of 30 columns of air holes was drilled on a silicon substrate according to the previous design. We used FEM to simulate the propagation of the waves in the GRIN PC. To this end, a line force was applied in front of the GRIN PC to

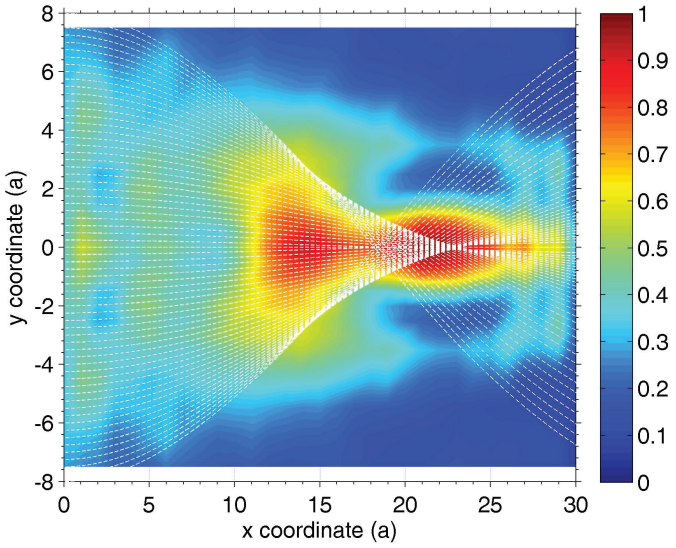


Figure 4.4: Numerical observation of normalized maximum displacement inside a GRIN PC of 30 columns. Dashed lines indicate ray trajectories.

continuously excite the Rayleigh waves at 20 MHz. Meanwhile, silicon substrates large enough to prevent from reflected waves from the boundaries, were added on both lateral sides of the GRIN PC. The simulations were set in such a way that not only Rayleigh waves get excited in the silicon but also other polarized waves. However, the displacements field was distributed mainly on the top surface with a wavelength along $x$-axis at any horizontal row of inclusions in good agreement with the value derived from $\lambda_{\Gamma X}(y) = 2\pi/k_{\Gamma X}(y)$. Figure 4.4 shows the normalized maxima of $u_z$ measured on the surface of the GRIN PC, as well as the ray trajectories noted by the dashed lines. The overall maximum value is found at $x = 22a$ with an amplitude of 2.8 times that of the incident wave, giving rise to the gain factor 2.8 at the focal distance $f_l = 22a$. The focus zone is found between $x = 20a$ and $x = 24a$. Both the focal distance and the focus zone have their positions in good agreement with the ray trajectories. In contrast from the case of $A_0$ mode in chapter 2, the focal distance of Rayleigh wave is however very close to the theoretical value $20a$ predicted by $\pi/2\delta$. One important reason is the low anisotropy of the GRIN PC for Rayleigh wave: e.g., the ratio $\eta(\theta) = (k - k_{\Gamma X})/k_{\Gamma X}$ is 0.056 along the central layer for Rayleigh wave to be compared to 0.069 for $A_0$ mode. Secondly, the GRIN PC has a large gradient coefficient $\delta$, leading to a shorter focal distance in comparison to the results in chapter 2. The focal zone is thus compacted to a smaller area along $x$-axis so that the absolute difference between numerical and theoretical values of the focal distance seems to be small.

The FWHM at the focus, is about $2.82a$ or $0.71\lambda_{min}$ with $\lambda_{min}\,(4a)$ being the wavelength in the central layer of GRIN PC along the ΓX. We will analyze the resolution below, together with the experimental results.

### 4.3.2 Experimental setup and samples

To verify the theoretical and numerical results, we fabricated a sample with 30 columns of air holes on a silicon substrate 500 $\mu$m thick, as shown in Figure 4.5. At the outcome of the fabrication process, the diameters of the holes were measured to be slightly larger than expected.[71] The laser ultrasonic technique was applied both to excite Rayleigh wave pulses and to monitor the normal displacements $u_z$ on the top surface of the GRIN PC, as already described in Chapter 2. A finer mask was used here in order to get a shorter distance between the light fringes impinging onto the sample, *i.e.*, to increase the working frequency up to 20 MHz. The incident waves stretched over a width much greater than the size of the GRIN PC, making it valid treating the incident waves as plane waves.

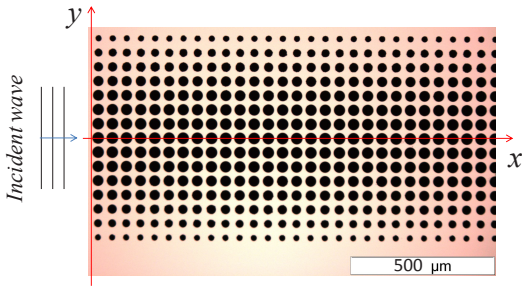


Figure 4.5: Image of experimental sample of GRIN PC.

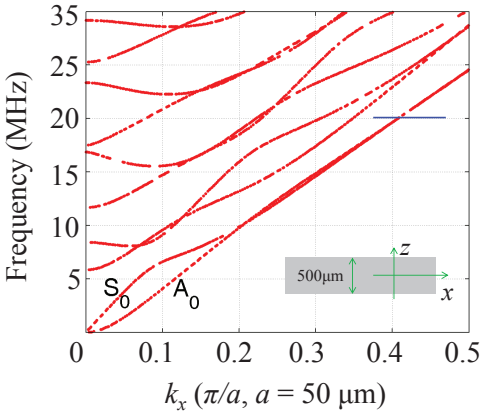


Figure 4.6: Dispersion curves of Lamb wave for a silicon plate of 500 $\mu$m in the $x$-$z$ plane as shown by the inset figure.

Before measuring $u_z$ in the GRIN PC, it is necessary to make sure that Rayleigh waves at 20 MHz can actually be excited on a 500 $\mu$m thick silicon substrate. To this end, we calculated the dispersion curves of Lamb waves,[120] as shown in figure 4.6. At 10 MHz and above, both $A_0$ and $S_0$ modes converge to the Rayleigh mode confirming that the substrate is semi-infinite at the working frequency of 20 MHz.

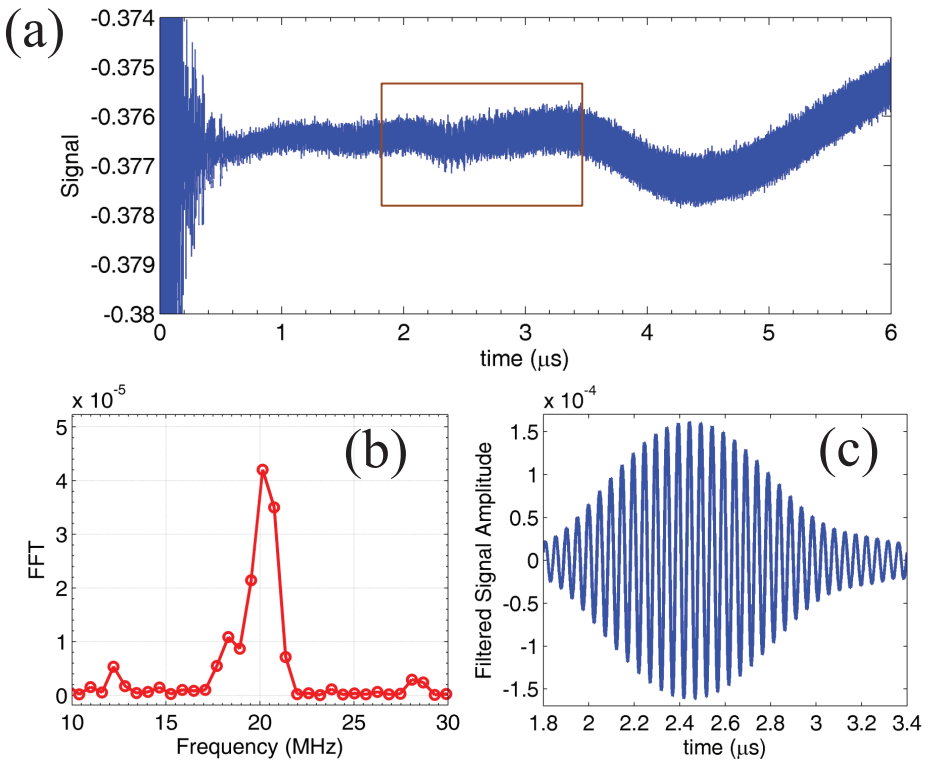


Figure 4.7: (a) Amplitude of observed original in a function of time, (b) frequency spectrum of an interested region from 1.8 $\mu$s to 3.4 $\mu$s, and (c) the filtered signal amplitude of interested region by a Gaussian profile centered at 20 MHz.

Figure 4.7(a) shows the signal $I(t)$ observed directly through the high-speed photodiode measured $\sim 600$ $\mu$m before the elastic waves impinge the GRIN PC. The signal of interest is located in the time range from 1.8 $\mu$s to 3.4 $\mu$s. Figure 4.7(b) shows the frequency spectrum of the averaged signal $\widetilde{I}(t)$ (see chapter 2) in this time range. The frequency is well centered at $\sim 20$ MHz with a FWHM of about 1 MHz, well satisfying the requirement. We show in figure 4.7(c) the filtered value $\widehat{I}(t)$ (see chapter 2) filtered by a Gaussian profile centered at 20 MHz. Very few noise affects $u_z$ and high S/N is achieved. Furthermore, $u_z$ has been recorded at several points over a 500 $\mu m$ length along $x$-axis, right in front of the GRIN PC. The measured wavelength at 20 MHz is about 250 $\mu m$, in excellent agreement with the theoretical value of 246 $\mu m$. Therefore our experimental technique is well suited to investigate the propagation of Rayleigh waves in air/silicon PCs.

### 4.3.3 Experimental results of Rayleigh wave focalization inside the GRIN PC

Both time and space dependence of the normal displacement $u_z$ was recorded on the middle part of the GRIN PC, in between $y = -5.5a$ and $y = 5.5a$. We have only

kept the maximum value of $u_z$ from each measurement. All these maxima were then normalized to unity, as shown in figure 4.8. A focusing zone clearly appears along $x$-coordinate, in between $x = 20a$ and $x = 25a$, which is in good agreement both with the calculated ray trajectories and with the numerical results. The overall maximum value of $u_z$ appears on the central row of inclusions at $x = 25a$ with an amplitude (25.9 pm) 3.2 times that of the incident wave (8.14 pm), in fairly good agreement with the values derived from our numerical simulations.

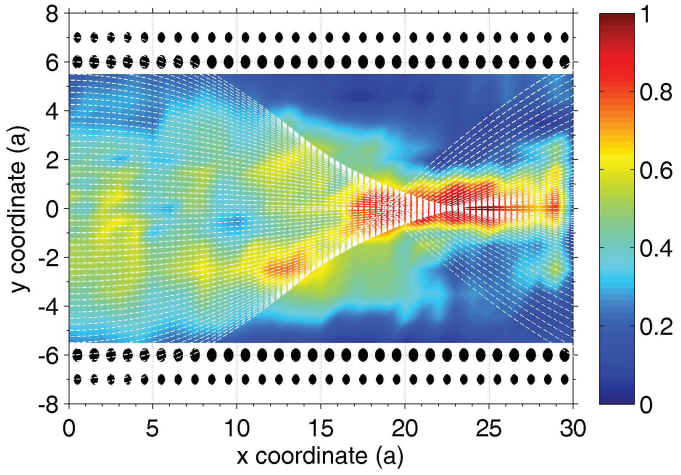


Figure 4.8: Experimental observation of normalized maximum displacement inside a GRIN PC of 30 columns. Dashed lines indicate ray trajectories. Circles indicate the air holes, and they do not keeps the real spatial ratio just for the display of figure.

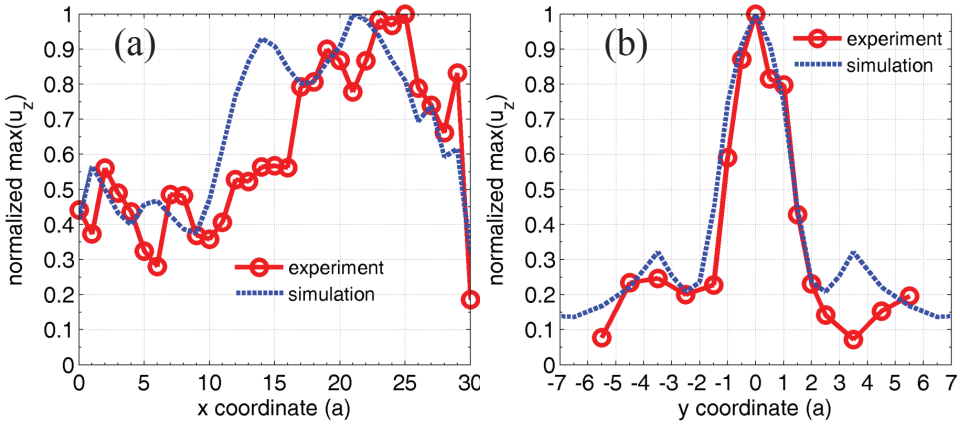


Figure 4.9: Focusing through a GRIN PC of 30 columns: (a) experimental (solid line) and numerical (dashed line) horizontal profile of normalized maxima of $u_z$ at the symmetric layer of GRIN PC, and (b) experimental (solid line) and numerical (dashed line) transverse profile of normalized maxima of $u_z$ at the focusing.

To further analyze the focus zone, we show in figure 4.9(a) the profile along the central layer and in figure 4.9(b) the transverse profile at the peak value. Along the

horizontal profile, the experiment yields a focal zone at a position slightly larger from the simulated value ($x = 25a$ instead of $x = 22a$). This small discrepancy could be imputed to the samples. Actually, as already noticed, the radii of the air holes are a little larger than the nominal value. Secondly, the air holes are designed to have a depth 5 times of the periodic constant. Upon completion of the fabrication process, the largest holes had a depth as designed while the smallest ones had not. This may affect the achievements of the GRIN PC. Actually, there is another peak at x=20a in figure 4.9(a), in a position different from the one predicted by the numerical study, *i.e.* $x = 15a$. This is probably caused by the same reason.

On the other hand, the profile measured along $y$-axis is in very good agreement with the numerical findings (figure 4.9(b)). The FWHM, either measured experimentally or derived from FEM computations, is $2.53a$ ($0.63\lambda_{min}$). The resolution is even smaller than the resolution of $A_0$ Lamb mode ($0.71\lambda_{min}$) we found in in chapter 2, for the square lattice. This is well explained by the larger gradient coefficient $\sim 0.80a^{-1}$ of the GRIN PC for the Rayleigh waves here than $\sim 0.67a^{-1}$ for $A_0$ Lamb mode in chapter 2. Moreover, the silicon is less anisotropic against the Rayleigh waves than it is against the Lamb modes. These two features combined, help increasing the $\mathbf{k_y}$ at the focus while at the same time reducing the impact of the anisotropy. The resolution is comparable and even better than an earlier study[75] with spoof surface acoustic wave (SSAW) in which a resolution of $0.70\lambda_{min}$ was claimed. The most relevant reason is that in our case, the depth of the air holes is larger than one wavelength and therefore the entire displacement field is affected, allowing the surface waves to converge at the focus in an ultimate manner.

## 4.4 Focalization outside GRIN PC

### 4.4.1 Experimental results of Rayleigh wave focalization behind GRIN PC

Both the simulations and the experiments have yielded sub-wavelength focusing for Rayleigh waves in a GRIN PC. In this Section, we move to the focusing behind the GRIN PC. To do this, another sample was elaborated, with 14 columns of air holes along $x$-coordinate.

The displacements $u_z$ were recorded on the plain silicon behind the lattice, over a length of $10a$, in between $y = -5.5a$ and $y = 5.5a$. Figure 4.10 shows the normalized maxima of $u_z$, together with the ray trajectories (dashed lines). A focusing zone stretching from $x = 16a$ to $x = 19a$ is clearly observed, which is in very good agreement with the calculated ray trajectories. Moreover, along the central layer, on the interface, $u_z$ is found with a large value. We have not clear explanation for

this feature but one hypothesis is that it might be caused by some resonant effect of the silicon bridges in between two consecutive holes.[92]

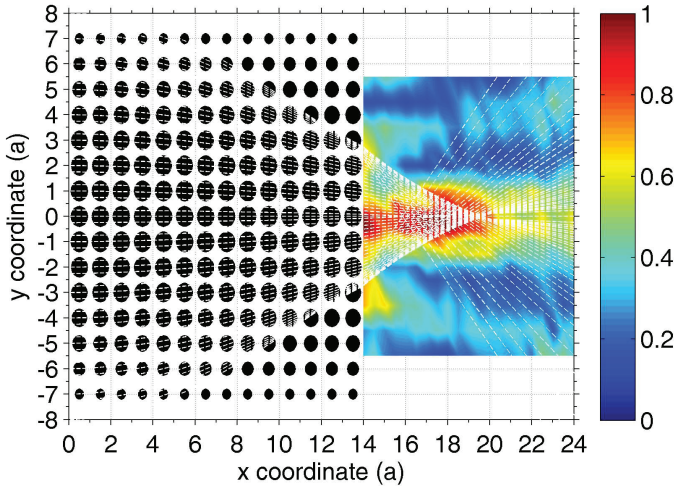


Figure 4.10: Experimental observation of normalized maximum displacement after a GRIN PC covering $x = [0,\ 14a]$. Dashed lines indicate ray trajectories both at the inner and behind the GRIN PC. Circles indicate the air holes.

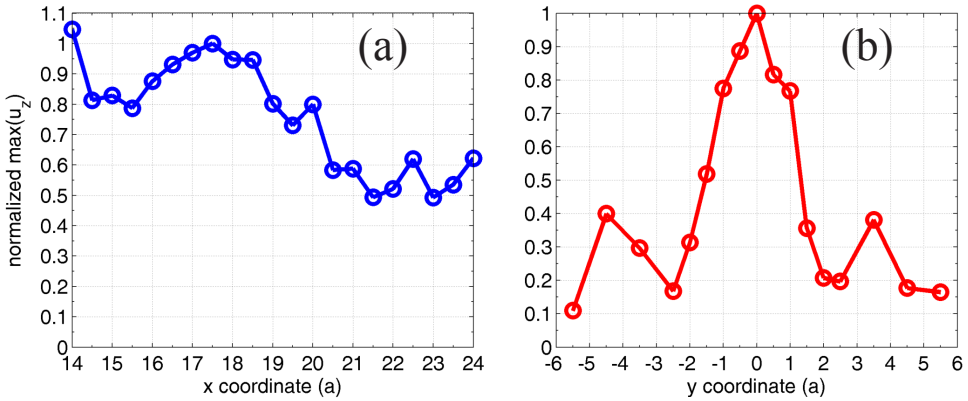


Figure 4.11: Focusing through a GRIN PC of 14 columns: (a) the horizontal profile of normalized maxima of $u_z$ along the central layer of GRIN PC, and (b) the transverse profile of normalized maxima of $u_z$ at the focusing.

To get insight into the quality of the focus, we show in figure 4.11(a) the horizontal profile of the normalized maxima at $y = 0$. The overall maximum $u_z$ is found at $x = 17.5a$, with an amplitude (19.6 pm) 2.2 times more than the amplitude of the incident wave (8.9 pm); this corresponds to a gain factor of 2.2. The gain factor is larger for the inward focusing than for the focusing behind the GRIN PC. This is natural since the waves are less converged in a lens of 14 columns than in a GRIN PC of 30 columns. Moreover, the partial reflection of the waves at the

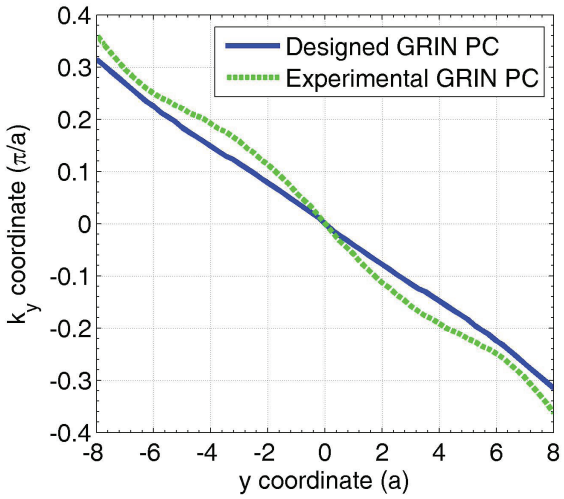


Figure 4.12: Profile of wave number $k_y$ corresponding to the incident position for the designed GIRN PC (solid line) and experimental GRIN PC (dashed line).

interface between the GRIN PC and the background still lessen the amplitude at the focusing.

The transverse profile at the peak value in 4.11(b) gives a FWHM of $2.87a$, which is larger than the absolute value of $2.53a$ measured in figure 4.9(b). Here again, this is attributed to the fact that incident waves are less focused by a GRIN PC of 14 columns. The FWHM, normalized to the wavelength in the background ($\lambda_B = 4.91a$), is however $0.58\lambda_B$, slightly smaller than the resolution $0.63\lambda_{min}$ for the inner focusing. Clearly, this should be attributed to the change of the reference wavelength. However, as compared to the resolution ($0.72\lambda_B$) measured in chapter 3 behind "conventional" GRIN PC, this resolution is much better and very close to the diffraction limit here. The reason is nothing else but the value of the ratio $k_M/k_B$, as discussed in what follows.

### 4.4.2 Discussions on the focusing resolution

To evaluate the focusing behind the GRIN PC, figure 4.12 shows the profiles of $k_y$ at the interface between GRIN PC and the background, both for the designed GRIN PC (solid line) with $k_M = 0.315\pi/a$ and for the actual sample (dashed line) with $k_M = 0.362\pi/a$. Before further analysis, figure 13 shows the ray trajectories for the experimental GRIN PC: the highest density appears at $x \sim 17a$, in good agreement with the experimental result, $x \sim 17.5a$.

The elastic energy carried by each acoustic ray may suffer losses during the propagation through the GRIN PC or at the interface between the GRIN PC and the background. The losses are different according to the trajectory since the elastic

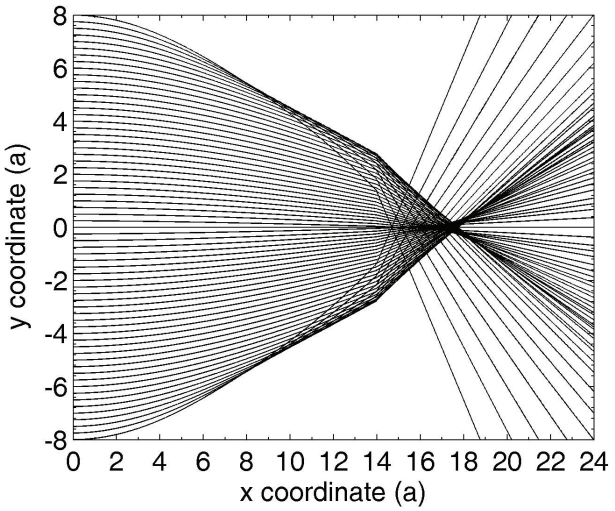


Figure 4.13: Ray trajectories of incident waves through the actual sample of GRIN PC.

impendence is position-dependent in. Once admitted this characteristic, we start the analysis by stating the dissipation is weak. We ignore the aberrations at the focus, considering that the focus is restricted to a small region of the unstructured isotropic substrate. Thus, the transverse profile at the peak becomes straight. It is similar to the image of a point source produced by a negative-index lens which, reads[9,25]

$$|u_z(y)| = \Big| \int_{-k_M}^{k_M} exp(ik_y y) dk_y \Big|. \tag{4.3}$$

Equation (4.3) leads to a primary spot with a full width $\Delta = 2\pi/k_M$, which displays an inverse relationship between the spot size and $k_M$. Figure 4.14 shows the transverse profile of $u_z$ at the peak value, derived from equation (4.3) for both the designed (blue solid line) and actual dimensions obtained at the end of the elaboration process (green dashed line) GRIN PCs, together with the profile of experimental results (circles). The FWHM along $y$-axis is $3.83a$ ($0.78\lambda_B$) for the designed GRIN PC and $3.32a$ ($0.68\lambda_B$) for the experimental GRIN PC. It sounds good for the experimental lens to feature a finer focusing since larger $k_M$ arise from the enlargement of the air holes because of fabrication issues. The derived profile of the experimental GRIN PC is actually in good agreement with the measured profile featuring a FWHM of $0.58\lambda_B$.

In order to go even further, we show in figure 4.15(a) a snapshot of the experimental focus while figure 4.15(b) represents the 2D Fourier transform of the snapshot. In figure 4.15(b), the components of **k** vector spread along the EFC for Rayleigh waves at 20 MHz, propagating in the background (solid line). Two main spots centered at $k_y = \pm 0.32\pi/a$ indicate the distribution of elastic energy within

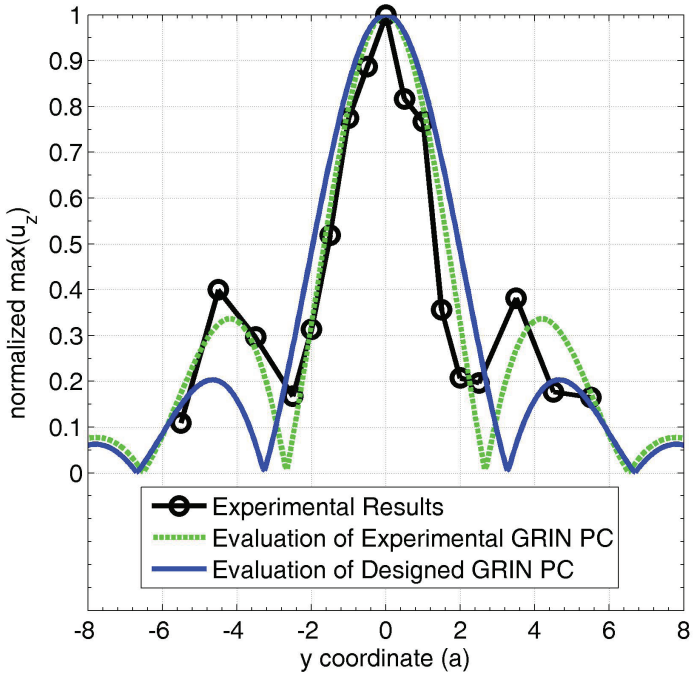


Figure 4.14: Transverse profile of maxima of $|u_z|$ at the peak value of focus: experimental result (circles), evaluation by equation (4.3) for the actual sample of the GRIN PC (green dashed line) or the designed one (blue solid line).

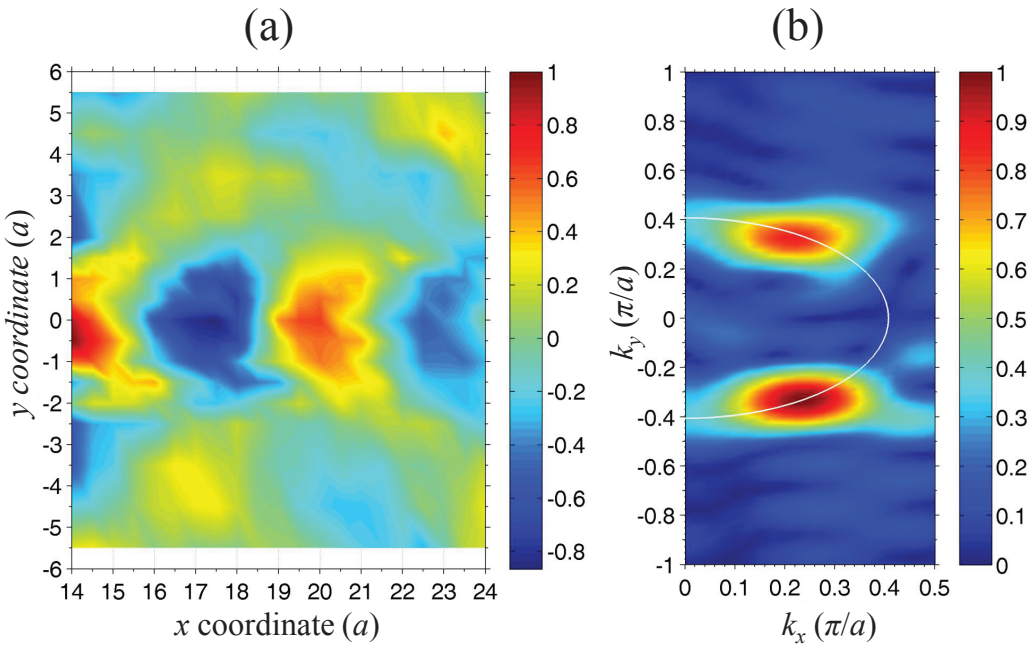


Figure 4.15: (a) Snapshot of the focusing and (b) the normalized two-dimensional Fourier transform of the snapshot image. The white solid line indicate the EFC of Rayleigh wave at 20 MHz.

the focal spot. This distribution along the EFC may have its origins in the internal resonances in the GRIN PC.[30] We however analyzed the features in the **k**-vector space using a continuous model. Firstly, within the focal spot, the absolute value of $k_y$ is restricted to the range $|k_y| < 0.36\pi/a$, in good agreement with the value of $k_M$ we found in the experimental GRIN PC. At the same time, the coefficient of the Fourier components takes small values in the range $|k_y| < 0.2\pi/a$, which corresponds to the layers within the zone $|y| < 4a$ in figure 4.12, because of the wave reflection caused by the large size of the air holes.

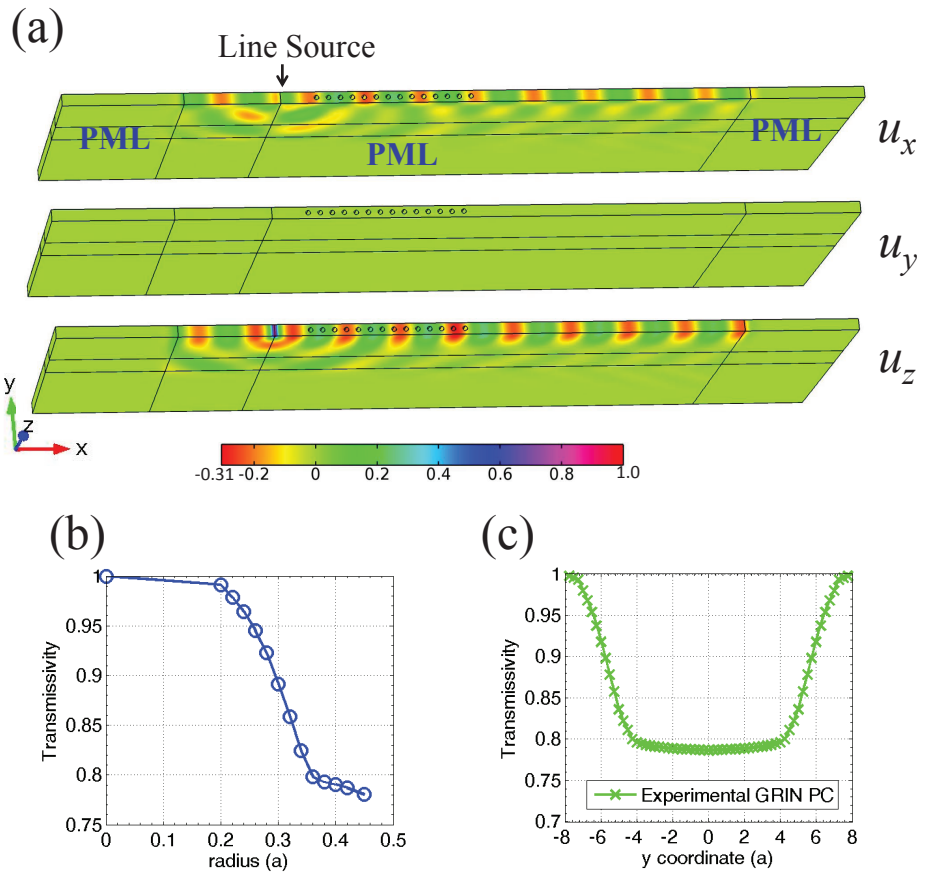


Figure 4.16: (a) Field of displacements in response to a line source applied in front of PC with 14 layers of air holes along the ΓX. PMLs were attached to prevent the effect of wave reflection. Periodic condition was applied along the lateral sides of PC and silicon plate to mimic an infinite PC. (b) Transmissivity as a function of the radius of air holes. The transmissivity is the ratio of $|u_z|$ measured after the PC to the $|u_z|$ of incident wave. (c) Transmissivity as a function of the position of incident wave.

We refine now the analysis by accounting for the transmissivity against $y$-axis, of each beam. Equation (4.3) changes[9]

$$|u_z(y)| = \left| \int_{-k_M}^{k_M} T(k_y) exp(ik_y y) dk_y \right|. \tag{4.4}$$

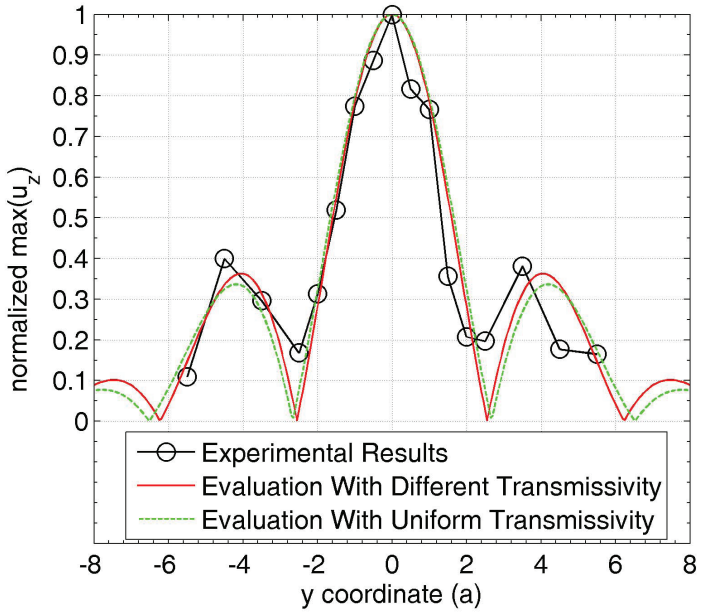


Figure 4.17: Transverse profile of $|u_z|$ at the peak value of focus: the experimental result (line with circles), the evaluation for the actual sample of the GRIN PC when considering (red solid line, by equation (4.3)) or ignoring (green dashed line, by equation (4.3)) the transmissivity.

where $T(k_y)$ is the transmissivity of the heterostructure which shall be location-dependent in the direct space and angle-dependent in the first Brillouin zone.

To simplify the physical model, the transmissivity was calculated along ΓX. Figure 4.16(a) shows the numerical model: a line of 14 identical air holes are drilled on the silicon substrate with the same depth, as in figure 4.1(a). The radius of the holes is an input parameter of the simulation. Periodic conditions were applied on each side along $y$-axis to mimic an infinite PC.[119] We implemented PMLs to enclose the substrate in an absorbing medium and to inhibit any reflection from boundaries. A vibrating line force was applied along $z$-axis, in front of the GRIN PC to excite the Rayleigh waves. In contrast to former chapters, we used here the *frequency domain* module in *structures* in Comsol Multiphysics to solve the 3D problem. In figure 4.16(a), the displacements field polarized within $x-z$ plane is confined over a one-wavelength depth from the top surface of the substrate, with $u_z$ dominating the displacements field. This confirms that the waves are properly excited. Whatever the radius of the air holes is, the maximum value of $u_z$ occurs within a spatial range of $3\lambda_B$ behind the GRIN PC. The transmissivity, defined as the ratio between the measured maximum of $u_z$ and the amplitude of the incident Rayleigh wave, is shown in Figure 4.16(b) for different radii of air holes. As expected, the transmissivity decreases gradually as the radius increases.

It is straightforward to deduce from figure 4.16(b) the transmissivity against

the position along $y$-axis. The result is shown in figure 4.16(c). The transmissivity for each horizontal row of inclusions being known, the transverse profile at the focus can be simply evaluated using equation (4.4). The result for a virtual sample having the actual dimensions of the sample that we used in the experiments is shown as red solid line in figure 4.17. For comparison, we show in the same figure as a green line, the transverse profile derived from equation (4.3) and as circles the experimental data. Accounting for the transmissivity does not affect the calculated transverse profile in a large extent; the FWHM is computed to $0.65\lambda_B$, very close to the experimental value $0.58\lambda_B$. This however allows to better account for the experimentally measured high and position of the lateral wings.

## 4.5 Conclusion

In this chapter, we have studied the focusing of Rayleigh waves both at the inner and outside a GRIN PC. We designed the heterostructure with squared symmetry by gradually modifying the radii of the air holes along the transverse direction of a silicon substrate.

A sample featuring 30 columns of air holes was fabricated on a substrate with a thickness two times the operating wavelength. The laser ultrasonic technique was applied both to excite and to detect the propagation of the Rayleigh waves. This technique allows for an accurate excitation of pulsed Rayleigh wave at an operating wavelength that can be finely tuned; this paves the way for further experiments. A sub-wavelength focusing is experimentally observed in the inner of the GRIN PC at a distance in good agreement with the predictions of ray trajectories analysis. The focus features a gain factor of 3.2 comparable with the one obtained with $A_0$ Lamb mode in chapter 2 and a FWHM of $0.63\lambda_{min}$. The fine focus obtained with the Rayleigh waves is attributed to a large gradient of the refractive index and the reduced anisotropy against the Rayleigh mode of the GRIN PC.

Then, a sample featuring 14 columns of air holes was used to study the focusing behind the GRIN PC. A sub-wavelength focusing is observed experimentally at the position predicted by the ray trajectories analysis, with a gain factor of 2.2. The transverse profile at the peak has a FWHM of $0.58\lambda_B$, even finer than the resolution for the $A_0$ Lamb mode behind the "conventional" GRIN PC in chapter 3. Such a sharp focus comes from the transverse components of the wave vector gathered at the focus, as noticed by the range of $k_y$ at the interface between the GRIN PC and the background. In fact, the resolution is found to be determined by the maximum of the transverse wavenumber. Finally, we discussed the effects of the transmissivity on the focusing properties. With such consideration, the focusing resolution gets very close to the experimental one of $0.65\lambda_B$.

# General Conclusion

GRIN PCs have demonstrated their merits to control the wave propagation by using the subwavelength unit cells. In this thesis, we followed this basic idea to control the propagation of elastic waves in such artificial lenses, including a series of works on both the $A_0$ mode Lamb wave and Rayleigh wave. The numerical and experimental results from these works, together with the formalism developed to calculate ray trajectories, have given some new understandings of the wave focusing in the acoustical lenses. We would like to give a summary of all the works in what follows.

At the very beginning, we investigated the $A_0$ mode focusing at the inner of GRIN PCs. We used two different lattice symmetries to design the artificial lens: the square lattice by modifying the radii of inclusions, and the rectangular lattice by modifying the distance between inclusions. A universal formalism was proposed to calculate the ray trajectories in any of the designed structures. This formalism, taking account of the anisotropy along any horizontal layer of PCs, has helped us to reveal the existence of aberrations at the inner focusing. The numerical results, together with the experimental results, have verified the accuracy of the formalism to predict the focus pattern, including the focal distance and focusing resolution at the low frequency. Both simulations and experiments have given a focus with a large gain factor and a small lateral resolution close to the diffraction limit. Meanwhile, the rectangular lattice has proven stronger ability to get a sharper resolution $\sim 0.64\lambda_{min}$ than its counterpart $\sim 0.71\lambda_{min}$ of the square lattice due to the reduced anisotropy.

After that, we have investigated numerically the efficiency of these devices to focalize waves within a broad range of frequencies: from the long-wavelength regime to the short-wavelength regime at the first acoustic branch. The formalism shows always high efficiency to predict the focus pattern within any of this broad range. At higher frequencies, the GRIN PC gets a shorter focal distance but an enlarged the gain factor with almost the same focusing resolution. These results can be useful for the experimental investigation in future.

Encouraged by the results on the inner focusing of $A_0$ in the lenses, we turned

our efforts to the focusing of $A_0$ mode behind them. The idea was to reduce the size of the artificial structures along the propagation direction and allow the elastic wave to converge in the non-structured plate behind the lenses. By this way, such PC based acoustical lens can be considered like a conventional optical lens and be useful for various instrumental applications. We used the GRIN PC of rectangular symmetry as found in chapter 2. We tried also several values smaller than the focal distance for the size of the lens in order to find a suitable one. For both numerical and experimental results, we find behind the lens a focusing zone well located at the position as predicted by the ray trajectories. The focusing resolution is found mostly relevant to the maximum transverse wavenumber $k_M$, in an inverse relationship.

To get a large $k_M$, a resonant structure formed by erecting pillars on the bridge of air/silicon PC was used as the basic unit to design GRIN PCs. The lens was designed in such a way that the $k_M$ was found surpass the wavenumber $k_B$ in the background, producing evanescent components at the exit of lens. With such a lens, we have found numerically the superlensing effect behind lens: the focusing resolution (FWHM) reached $0.44\lambda_B$. The bound modes, which are leaky between the PC and the background, work as the mechanism to transfer the evanescent components to the focus, giving rise to the superlensing effect together with the propagative modes. The experimental results, although not being able to surpass the diffraction limit, have indeed ensured a focusing resolution $0.53\lambda_B$ being very close to the limit. The disagreement between the experiments and simulations comes mainly from the fabrication of experimental samples, as noticed in chapter 3. However, the resonant GRIN PC has shown its dramatic abilities to get a focusing behind itself with a very small resolution.

Different from the $A_0$ mode Lamb wave, Rayleigh waves travel on the surface of an semi-infinite solid substrate penetrating to a depth of one wavelength. These waves are interesting for their sensitivity to surface defects (and other surface features) and can be used to inspect areas that other waves might have difficulty reaching. Analogously to previous chapters, we designed the GRIN PC for Rayleigh wave by gradually modifying the radii of inclusions. The ray trajectories, together with experimental results, have revealed first the focus pattern at the inner of lens. Without using silicon pillars, the lens gives a large gain factor and a focusing resolution $0.63\lambda_{min}$ due to the large gradient coefficient and the reduced anisotropy. Secondly, we turned to the focusing behind the lens. The analysis of Fourier component and wave transmission, together with experimental results, has revealed a focus pattern with the resolution determined by the $k_M$ in this case, close to $0.58\lambda_B$.

This work is devoted to study of focusing the plate and surface acoustic waves by using the GRIN PCs. For both the long-wavelength and short-wavelength regimes, we show that the formalism of computing ray trajectories serves an useful tool to

the engineering of such acoustical lenses, aiding the lens as smart and compact devices in future. The formalism shall be useful in future where the anisotropy may display important influences. In a view of engineering, we show that the $k_M$ is one of the most important parameters to determine the focusing resolution behind the lens. However, for the inner focusing, we have not claimed the same conclusion, for both the aberrations at the focus and most importantly the graded properties of lens. This may be one of our future topics.

This work has not claimed to now the possible applications of the resonant structures proposed in Ref [119] by Khelif *et al.*, to design graded lens for Rayleigh wave. As proposed in chapter 3, once the transverse wavenumber can be larger than wavenumber in the background, the artificial lens has a chance to gather the fine information carried by the evanescent components at the focus, so that the superlensing effect is possible for the positive-index lens. However this needs being verified in future.

Another topic of interest is to focalize the zero-order symmetric ($S_0$) Lamb mode by the trampoline, which is already noticed in chapter 3. In future, we need possible modifications of the resonant structure to find suitable designs for the $S_0$ mode, so that we can have a chance to get evanescent components.

# Appendix A

# Examples of computing ray trajectories

The formalism that we have developed to compute ray trajectories was used throughout this work. In this appendix, we would like to give examples on the formalism together with the ABCD law.

## A.1 k vector based method

We began with an example by using the GRIN PC of square symmetry in chapter 2 where the GRIN PC was assumed to have the wavenumber

$$k(y,\theta) = k_{\Gamma X}(y)\frac{1-\alpha(y)cos(4\theta)}{1-\alpha(y)}, \quad \alpha(y) = \frac{k_{\Gamma M}(y)-k_{\Gamma X}(y)}{k_{\Gamma M}(y)+k_{\Gamma X}(y)} \tag{A.1}$$

with $k_{\Gamma X}(y)$ and $k_{\Gamma M}(y)$ the wavenumber along the ΓX and ΓM, $\theta$ the angle in the first Brillouin zone, and $\alpha(y)$ the anisotropy coefficient. At 5 MHz, $k_{\Gamma X}(y)$ is described by a hyperbolic secant profile

$$k_{\Gamma X}(y) = 0.457\pi/a \times \text{sech}(0.065y/a), \tag{A.2}$$

while the anisotropy coefficient $\alpha(y)$ can be fitted by the polynomials

$$\begin{aligned}\alpha(y) = 0.0332 - \frac{7.585}{10^{19}}(\frac{y}{a}) - \frac{9.994}{10^{4}}(\frac{y}{a})^2 + \frac{5.384}{10^{20}}(\frac{y}{a})^3 \\ + \frac{3.866}{10^{6}}(\frac{y}{a})^4 - \frac{5.571}{10^{22}}(\frac{y}{a})^5 + \frac{2.808}{10^{9}}(\frac{y}{a})^6\end{aligned}. \tag{A.3}$$

Figure A.1 shows the profiles of both (a) the wavenumber $k_{\Gamma X}$ and (b) the anisotropy coefficient $\alpha$. The discrete values obtained by FEM (circles) are in good agreement with the fitting curves (solid lines) derived from equations (A.2) and (A.3).

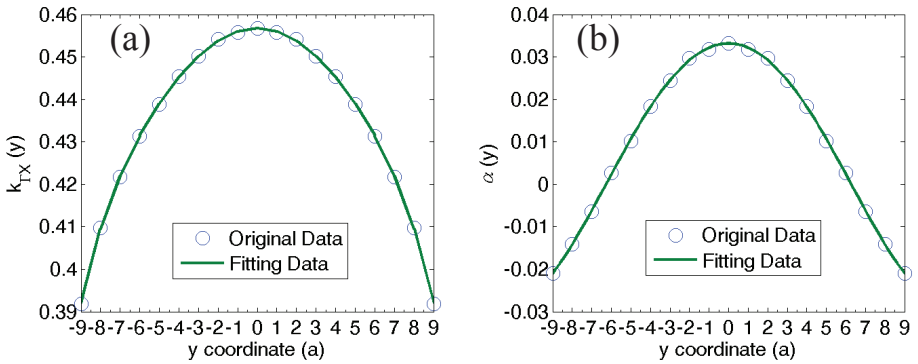


Figure A.1: Profiles of (a) wavenumber $k_{\Gamma X}$ and (b) anisotropy coefficient $\alpha$. In both figures, the circles stand for discrete obtained by FEM while the solid lines indicate the fitting curves from equations (A.2) and (A.3).

The strategy of computation is to find ray trajectories one by one. Let us think about one trajectory starting at $y = 8a$, as shown in figure A.2. We set $y|_{x=0} = 8a$ as the first position of ray trajectory at which the $\mathbf{k}$ vector has its component $k_y = 0$ while the $k_x$ determined by

$$k_x^0 = k(y{=}8a, \theta{=}0). \tag{A.4}$$

The Snell's law says that the transverse wavenumber is conserved at the interface between two materials. As a consequence, $k_x$ keeps the constant along any ray trajectory within the GRIN lens. To find the trace at other positions, we defined an uniform spatial step $\Delta x$ along the $x$-axis. At the second position with $x = \Delta x$, it assumes

$$y|_{x=\Delta x} = y|_{x=0} + \Delta y, \tag{A.5}$$

where $\Delta y$ stands for the increment of $y(x)$. Actually, equation (A.2) says that the wavenumber $k(y < 8a, \theta = 0)$ is larger than the wave number $k(y = 8a, \theta = 0)$. Supported by the Snell's law, when wave propagates from the first position to the second one, the $\mathbf{k}$ vector tilts away from the horizontal direction towards the central layer of GRIN PC. This gives rise to the $\Delta y \neq 0$. For a small step $\Delta x$, the $\mathbf{k}$ vector is expected to have a small angle, which produces a tiny value for $\Delta y$ assumed to be $-1e^{-5}$ in our calculation. We have also tried other values for $\Delta y$ with each time the same path for the ray. Besides, $\Delta y$ needs changing its sign for a ray starting at the opposite side of lens for example at $y = -8a$.

Considering $k_x$ keeps constant along any ray trajectory, angle $\theta$ at the second position can be derived from

$$\begin{aligned} k_x &= k_x^0, \\ k_x &= k(y|_{x=\Delta x}, \theta)\cos(\theta). \end{aligned} \tag{A.6}$$

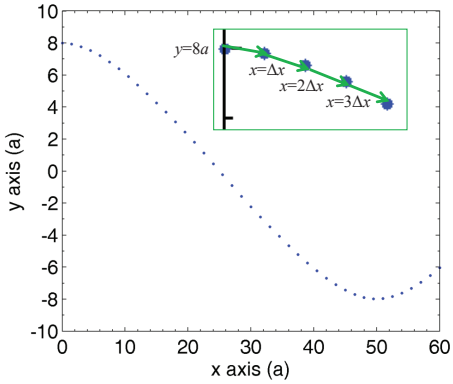


Figure A.2: Scheme of calculation of ray trajectory beginning at $y$=8$a$. The first several points are amplified as shown by the inset.

It is not doable to give an analytical solution to this equation. We used here a numerical skill to find the solution of $\theta$ by defining a function

$$g(\psi) = k(y|_{x=\Delta x}, \psi)\cos(\psi) - k_x^0, \tag{A.7}$$

where $\psi$ stands for a variable in the first Brilluion zone. Scan the $\psi$ in the range $[0, -\pi/2]$ with a small step $\Delta\psi$ ($\pi/1000$ here). At certain value, the function $g(\psi)$ will change the sign, and set the $\theta$ be equal to this $\psi$. Again, for a ray leaving at $y = -8a$ we scan the $\psi$ in the opposite range $[0, \pi/2]$. The group velocity is perpendicular to the EFC of GRIN PC, yielding to the relationship

$$\begin{aligned} \tan(\varphi) &= -\frac{\partial k_x}{\partial \theta}\left(\frac{\partial k_y}{\partial \theta}\right)^{-1} \\ k_x = k(y,\theta)\cos(\theta), &\quad k_y = k(y,\theta)\sin(\theta) \end{aligned}. \tag{A.8}$$

where $\varphi$ is the angle between the group velocity and ΓX orientation. Meanwhile, the group velocity is parallel to the tangent of ray path, so that it holds

$$\tan(\varphi) = \frac{\mathrm{d}y(x)}{\mathrm{d}x}. \tag{A.9}$$

Combining equations (A.8) and (A.9), ray trajectory at the third position $x$=2$\Delta x$ is found as

$$y|_{x=2\Delta x} = y|_{x=\Delta x} + \Delta x \times \tan(\varphi|_{x=\Delta x}). \tag{A.10}$$

To obtain ray trajectory at following positions $x = m\Delta x$ ($m \geq 3$), it needs just the repetition of equations (6)-(10) in order, by replacing the $x = \Delta x$ with $x = (m-1)\Delta x$ and $x = 2\Delta x$ with $x = m\Delta x$, respectively. In figure 2 the ray trajectory $y(x)$ becomes very close to the $y = -8a$ at $x = 49a$. During the calculation, once the $|y(x)| > 8a$, the ray trajectory is adjusted since physically this kind of situation

is not reasonable.

To get other rays, it needs just the repetition of equations (A.4)-(A.10) by replacing $y = 8a$ with the corresponding starting position. The formalism is sufficient to find not only the ray trajectory $y(x)$, the angle $\theta$, or the $\tan(\varphi)$, but also the wavenumber $k_y$ and the ratio $\tan(\varphi)/\tan(\theta)$. Same processes can be easily extended to other waves for the focusing both at the inner of GRIN PCs or behind them.

## A.2 ABCD law

When ignoring the anisotropy of any horizontal inclusion, wavenumber of the GRIN PC changes into

$$k = k_{\Gamma X} = 0.457\pi/a \times \mathrm{sech}(0.065y/a), \tag{A.11}$$

which means that the refractive index $n_{eff}$ follows the hyperbolic secant profile

$$\begin{aligned} n_{eff} &= n_0 \mathrm{sech}(\delta y), \\ n_{eff} &= k/k_B, \end{aligned} \tag{A.12}$$

with $n_0 = 1.166$ the refractive index of the central layer, $\delta = 0.065a^{-1}$ the gradient coefficient, and $k_B = 0.392\pi/a$ the wavenumber of the background.

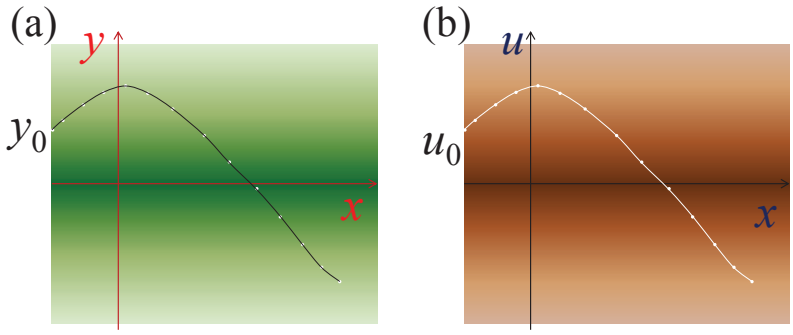


Figure A.3: Scheme of one ray trajectory in a GRIN lens in the (a) $x - y$ space and (b) $x - u$ space. A coordinate transformation is make for the $y$-coordinate into a hyperbolic coordinate $u$ by equation (A.13).

Figure A.3 shows the scheme of one trajectory in the GRIN lens, beginning at $y_0$ with a slope $\dot{y}_0$. To find the ray trajectory at any position, we make first a coordinate transformation

$$\begin{aligned} u &= \sinh(\delta y), \\ \dot{u} &= \dot{y}\delta\cosh(\delta y). \end{aligned} \tag{A.13}$$

of $y$-coordinate into the hyperbolic coordinate $u$. Ray trajectory at any position in

the $x-u$ space can be determined by a transfer matrix or the ABCD law

$$\begin{aligned}\begin{bmatrix} u(x) \\ \dot{u}(x) \end{bmatrix} &= \begin{bmatrix} H_f & H_a \\ \dot{H}_f & \dot{H}_a \end{bmatrix} \begin{bmatrix} u_0 \\ \dot{u}_0 \end{bmatrix} \\ &= \begin{bmatrix} \cos(\delta x) & \sin(\delta x)/\delta \\ -\sin(\delta x)/\delta & \cos(\delta x) \end{bmatrix} \begin{bmatrix} u_0 \\ \dot{u}_0 \end{bmatrix},\end{aligned} \tag{A.14}$$

where $H_a$ and $H_f$ are the axial and the field rays whereas $\dot{H}_a$ and $\dot{H}_f$ are the slopes of the axial and field rays, respectively. $u_0$ and $\dot{u}_0$ are derived from equation (A.13)

$$\begin{aligned} u_0 &= \sinh(\delta y_0), \\ \dot{u}_0 &= \dot{y}_0 \delta \cosh(\delta y_0). \end{aligned} \tag{A.15}$$

Equation (A.14) shows that once $u_0$ and $\dot{u}_0$ are known, we can infer the $u$ and $\dot{u}$ at any position $x$ in the lens. Different from our formalism, the ABCD law needs not knowing the $u$ and $\dot{u}$ at the previous neighbor point. The ABCD law applies however to very few transverse profiles within the framework of paraxial approximation. It cannot evaluate the influences of anisotropy as what does our formalism to now.

The ray trajectory at any position in the direct space can be derived by using the inverse computation of equation (A.13)

$$\begin{aligned} y &= \sinh^{-1}\big[u(x)\big]/\delta, \\ \dot{y} &= \frac{\dot{u}(x)}{\delta \cosh(\delta x)}. \end{aligned} \tag{A.16}$$

We consider now the normal incident wave in the planar GRIN lens. It says $\dot{y}_0 = 0$ for any trajectory and in turn $\dot{u}_0 = 0$ as derived from equation (A.15). Substituting $\dot{u}_0 = 0$ into equations (A.14) and (A.16), it finds that

$$y(x) = \frac{\sinh^{-1}\big[\cos(\delta x) \times \sinh(\delta y_0)\big]}{\delta}. \tag{A.17}$$

Clearly, the hyperbolic profile gives an oscillatory path for any trajectory in the planar lens. Meanwhile, it promises for any of them

$$\begin{aligned} y(x|_{f_l}) &= 0, \\ f_l &= \frac{\pi}{2\delta}. \end{aligned} \tag{A.18}$$

Therefore, the hyperbolic secant profile focus all the ray trajectories at the same point with the focal distance $f_l$ depending only on the gradient coefficient $\delta$.

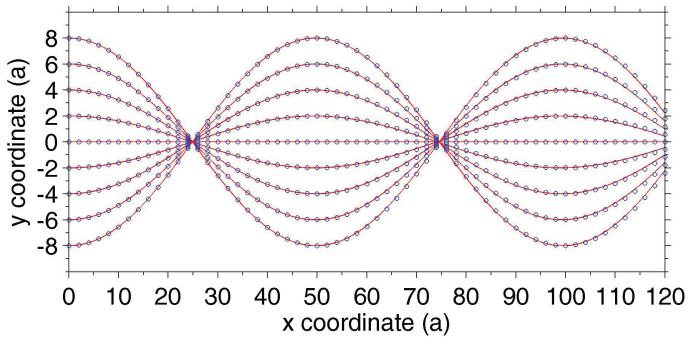


Figure A.4: Ray trajectories in a planer GRIN lens featuring the hyperbolic secant profile as in equation (A.12) with $n_0 = 1.116$ and $\delta = 0.065^{-1}$. Circles lines stand for results derived from the ABCD law while solid lines are for results from the **k** vector based method.

Figure A.4 shows the path of rays in a planer GRIN lens featuring the hyperbolic secant profile as in equation (A.12) with $n_0 = 1.116$ and $\delta = 0.065^{-1}$. We used both the ABCD law (circles) and the **k** vector based method (solid lines) to find the focal distance. Ray trajectories derived from the two methods are in excellent agreement. All the rays are converged to the same point at a distance about $25a$ as predicted by $\pi/2\delta$.

We consider now a general expression for the hyperbolic secant profile

$$n_{eff}^2 = n_s^2 + (n_0^2 - n_s^2)\mathrm{sech}^2(\delta y), \tag{A.19}$$

with $n_s$ the refractive index of substrate. To find the ray trajectory, we make the same coordinate transformation as equation (A.13), and get the transfer matrix

$$\begin{bmatrix} u(x) \\ \dot{u}(x) \end{bmatrix} = \begin{bmatrix} \cos(\delta\gamma x) & \sin(\delta\gamma x)/\delta\gamma \\ -\sin(\delta\gamma x)/\delta\gamma & \cos(\delta x) \end{bmatrix} \begin{bmatrix} u_0 \\ \dot{u}_0 \end{bmatrix}, \tag{A.20}$$

where $\gamma$ is written as

$$\gamma = \frac{\sqrt{l_0^2 - n_s^2}}{l_0}, \quad l_0 = \frac{n(y)}{\sqrt{(1+\dot{y}^2)}}. \tag{A.21}$$

$l_0$ stands for the cosine of optical index along $y$-axis. It is invariant along any ray within the medium. The inverse computation of $u(x)$ finds the same expression as equation (A.16). Substituting $\dot{u}_0 = 0$ into equations (A.20) and (A.16), it finds that

$$y(x) = \frac{\sinh^{-1}\left[\cos(\delta\gamma x) \times \sinh(\delta y_0)\right]}{\delta}, \tag{A.22}$$

with the focal distance

$$f_l = \frac{\pi}{2\delta\gamma}. \tag{A.23}$$

Let us return to equation (A.21). It says $\dot{y}_0 = 0$ for the initial slope of any ray of the normal incident wave. Therefore, $\gamma$ can be written as

$$\gamma = \frac{\sqrt{n(y)^2 - n_s^2}}{n(y)}. \tag{A.24}$$

$\gamma$ is relevant to the $n(y)$ so that it is variant between different ray trajectories although it keeps constant along the same path. As a consequence, the focal distance $f_l$ is different between ray trajectories, yielding to aberrations at the focus. Furthermore, equation (A.24) gives a $\gamma$ smaller than one so that the focal distance $\pi/2\delta\gamma$ in equation (A.23) is enlarged in comparison to the one $\pi/2\delta$ in equation (A.18).

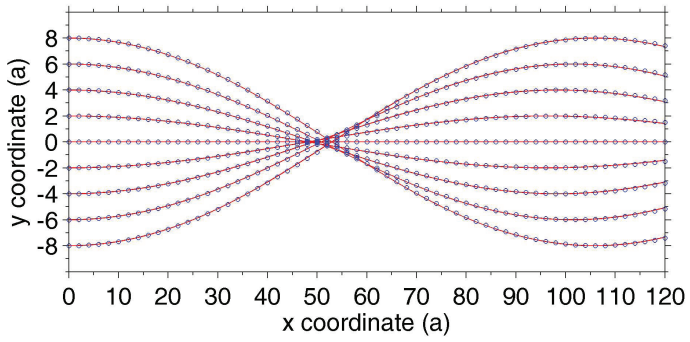


Figure A.5: Ray trajectories in a planer GRIN lens featuring the general hyperbolic secant profile as in equation (A.19) with $n_0 = 1.116$, $n_s = 1$, and $\delta = 0.065^{-1}$. Circles lines stand for results derived from the ABCD law while solid lines are for results from the **k** vector based method.

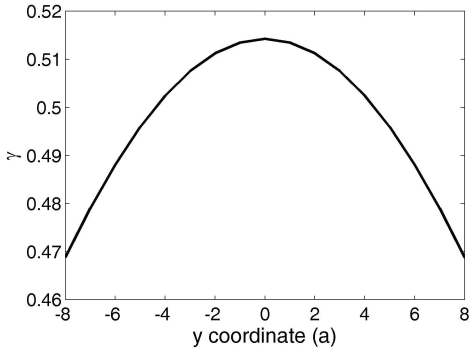


Figure A.6: Profile of $\gamma$ against $y$-axis for the planer GRIN lens with a general hyperbolic secant profile as in equation (A.19) with $n_0 = 1.116$, $n_s = 1$, and $\delta = 0.065^{-1}$.

Figure A.5 shows the path of rays in a planer GRIN lens featuring the general hyperbolic secant profile as in equation (A.19) with $n_0 = 1.116$, $n_s = 1$, and $\delta = 0.065^{-1}$. The ABCD law (circles) and the **k** vector based method (solid lines) have produced the same results. We observe a focus with geometrical aberrations

located at a distance about $50a$, almost two times of the focal distance $25a$ in figure A.4. This is understandable if we review the profile of $\gamma$ against $y$-axis as shown in figure A.6. The $\gamma$ takes its value close 0.5 which can double the focal distance $\pi/2\delta$ according to equation (A.23). Meanwhile, $\gamma$ decreases gradually from the symmetric axis of lens to the lateral sides. As a result, ray trajectories beginning from the lateral sides are crossed to the symmetric axis at a distance larger than those from the center axis of lens.

# Bibliography


[1] M. S. Kushwaha, P. Halevi, L. Dobrzynski, and B. Djafari-Rouhani, "Acoustic band structure of periodic elastic composites," *Physical Review Letters*, vol. 71, pp. 2022–2025, Sep 1993.

[2] M. S. Kushwaha, P. Halevi, G. Martínez, L. Dobrzynski, and B. Djafari-Rouhani, "Theory of acoustic band structure of periodic elastic composites," *Physical Review B*, vol. 49, pp. 2313–2322, Jan 1994.

[3] S. John, "Strong localization of photons in certain disordered dielectric superlattices," *Physical Review Letters*, vol. 58, p. 2486, June 1987.

[4] E. Yablonovitch, "Inhibited spontaneous emission in solid-state physics and electronics," *Physical Review Letters*, vol. 58, p. 2059, May 1987.

[5] B. Léon, *Wace Propagation in Periodic Structures*. Dover Publications, Inc., dover phoenix editions ed., 1953.

[6] J. B. Pendry, "Negative refraction makes a perfect lens," *Physical Review Letters*, vol. 85, pp. 3966–3969, Oct 2000.

[7] V. G. Veselago, "The electrodynamics of substances with simultaneously negative values of $\epsilon$ and $\mu$," *Soviet Physics Uspekhi*, vol. 10, pp. 509–514, January 1968.

[8] C. Luo, S. G. Johnson, J. D. Joannopoulos, and J. B. Pendry, "All-angle negative refraction without negative effective index," *Physical Review B*, vol. 65, p. 201104, May 2002.

[9] C. Luo, S. G. Johnson, J. D. Joannopoulos, and J. B. Pendry, "Subwavelength imaging in photonic crystals," *Physical Review B*, vol. 68, p. 045115, Jul 2003.

[10] S. Durant, Z. Liu, J. M. Steele, and X. Zhang, "Theory of the transmission properties of an optical far-field superlens for imaging beyond the diffraction limit," *Journal of the Optical Society of America B*, vol. 23, pp. 2383–2392, November 2006.

[11] Z. Liu, S. Durant, H. Lee, Y. Pikus, N. Fang, Y. Xiong, C. Sun, and X. Zhang, "Far-field optical superlens," *Nano Letters*, vol. 7, no. 2, pp. 403–408, 2007.

[12] F. Lemoult, G. Lerosey, J. de Rosny, and M. Fink, "Resonant metalenses for breaking the diffraction barrier," *Physical Review Letters*, vol. 104, p. 203901, May 2010.

[13] X. Hu, Y. Shen, X. Liu, R. Fu, and J. Zi, "Superlensing effect in liquid surface waves," *Physical Review E*, vol. 69, p. 030201, Mar 2004.

[14] X. Zhang and Z. Liu, "Negative refraction of acoustic waves in two-dimensional phononic crystals," *Applied Physics Letters*, vol. 85, no. 2, pp. 341–343, 2004.

[15] J. Li, Z. Liu, and C. Qiu, "Negative refraction imaging of acoustic waves by a two-dimensional three-component phononic crystal," *Physical Review B*, vol. 73, p. 054302, Feb 2006.

[16] M. Ke, Z. Liu, C. Qiu, W. Wang, J. Shi, W. Wen, and P. Sheng, "Negative-refraction imaging with two-dimensional phononic crystals," *Physcial Review B*, vol. 72, p. 064306, Aug 2005.

[17] C. Qiu, X. Zhang, and Z. Liu, "Far-field imaging of acoustic waves by a two-dimensional sonic crystal," *Physical Review B*, vol. 71, p. 054302, Feb 2005.

[18] A. Sukhovich, L. Jing, and J. H. Page, "Negative refraction and focusing of ultrasound in two-dimensional phononic crystals," *Physcial Review B*, vol. 77, p. 014301, Jan 2008.

[19] Z. He, Y. Heng, S. Peng, Y. Ding, M. Ke, and Z. Liu, "Acoustic collimating beams by negative refraction in two-dimensional phononic crystal," *Journal of Applied Physics*, vol. 105, no. 11, p. 116105, 2009.

[20] M. Notomi, "Theory of light propagation in strongly modulated photonic crystals: Refractionlike behavior in the vicinity of the photonic band gap," *Physcial Review B*, vol. 62, pp. 10696–10705, Oct 2000.

[21] S. Yang, J. H. Page, Z. Liu, M. L. Cowan, C. T. Chan, and P. Sheng, "Focusing of sound in a 3d phononic crystal," *Phys. Rev. Lett.*, vol. 93, p. 024301, Jul 2004.

[22] M.-H. Lu, C. Zhang, L. Feng, J. Zhao, Y.-F. Chen, Y.-W. Mao, J. Zi, Y.-Y. Zhua, S.-N. Zhu, and N.-B. Ming, "Negative birefraction of acoustic waves in a sonic crystal," *Nature Materials*, vol. 6, pp. 744–748, August 2007.

[23] A. Sukhovich, B. Merheb, K. Muralidharan, J. O. Vasseur, Y. Pennec, P. A. Deymier, and J. H. Page, "Experimental and theoretical evidence for sub-wavelength imaging in phononic crystals," *Physical Review Letters*, vol. 102, p. 154301, Apr 2009.

[24] Z. He, X. Li, J. Mei, and Z. Liu, "Improving imaging resolution of a phononic crystal lens by employing acoustic surface waves," *Journal of Applied Physics*, vol. 106, no. 2, p. 026105, 2009.

[25] J.-F. Robillard, J. Bucay, P. A. Deymier, A. Shelke, K. Muralidharan, B. Merheb, J. O. Vasseur, A. Sukhovich, and J. H. Page, "Resolution limit of a phononic crystal superlens," *Physical Review B*, vol. 83, p. 224301, Jun 2011.

[26] M. Farhat, S. Guenneau, S. Enoch, A. B. Movchan, and G. G. Petursson, "Focussing bending waves via negative refraction in perforated thin plates," *Applied Physics Letters*, vol. 96, no. 8, p. 081909, 2010.

[27] B. Morvan, A. Tinel, A.-C. Hladky-Hennion, J. Vasseur, and B. Dubus, "Experimental demonstration of the negative refraction of a transverse elastic wave in a two-dimensional solid phononic crystal," *Applied Physics Letters*,

vol. 96, no. 10, p. 101905, 2010.

[28] J. Pierre, O. Boyko, L. Belliard, J. O. Vasseur, and B. Bonello, "Negative refraction of zero order flexural lamb waves through a two-dimensional phononic crystal," *Applied Physics Letters*, vol. 97, no. 12, p. 121919, 2010.

[29] C. Croënne, E. D. Manga, B. Morvan, A. Tinel, B. Dubus, J. Vasseur, and A.-C. Hladky-Hennion, "Negative refraction of longitudinal waves in a two-dimensional solid-solid phononic crystal," *Physcial Review B*, vol. 83, p. 054301, Feb 2011.

[30] A.-C. Hladky-Hennion, C. Cronne, B. Dubus, J. Vasseur, L. Haumesser, D. Manga, and B. Morvan, "Negative refraction of elastic waves in 2d phononic crystals: Contribution of resonant transmissions to the construction of the image of a point source," *AIP Advances*, vol. 1, no. 4, p. 041405, 2011.

[31] I. A. Veres, T. Berer, O. Matsuda, and P. Burgholzer, "Focusing and subwavelength imaging of surface acoustic waves in a solid-air phononic crystal," *Journal of Applied Physics*, vol. 112, no. 5, p. 053504, 2012.

[32] M. A. Al-Lethawe, M. Addouche, A. Khelif, and S. Guenneau, "All-angle negative refraction for surface acoustic waves in pillar-based two-dimensional phononic structures," *New Journal of Physics*, vol. 14, no. 12, p. 123030, 2012.

[33] N. Swinteck, J. O. Vasseur, A. C. Hladky-Hennion, C. Cronne, S. Bringuier, and P. A. Deymier, "Multifunctional solid/solid phononic crystal," *Journal of Applied Physics*, vol. 112, no. 2, p. 024514, 2012.

[34] M. Dubois, M. Farhat, E. Bossy, S. Enoch, S. Guenneau, and P. Sebbah, "Flat lens for pulse focusing of elastic waves in thin plates," *Applied Physics Letters*, vol. 103, no. 7, p. 071915, 2013.

[35] H. Jia, M. Lu, Q. Wang, M. Bao, and X. Li, "Subwavelength imaging through spoof surface acoustic waves on a two-dimensional structured rigid surface," *Applied Physics Letters*, vol. 103, no. 10, p. 103505, 2013.

[36] M. Addouche, M. A. Al-Lethawe, A. Choujaa, and A. Khelif, "Superlensing effect for surface acoustic waves in a pillar-based phononic crystal with negative refractive index," *Applied Physics Letters*, vol. 105, no. 2, p. 023501, 2014.

[37] J. L. Henri and T. Tineke, "Diffracted evanescent wave model for enhanced and suppressed optical transmission through subwavelength hole arrays," *Optics Express*, vol. 12, pp. 3629–3651, August 2004.

[38] R. Zia, M. D. Selker, and M. L. Brongersma, "Leaky and bound modes of surface plasmon waveguides," *Physical Review B*, vol. 71, p. 165431, Apr 2005.

[39] R. J. P. Engelen, D. Mori, T. Baba, and L. Kuipers, "Subwavelength structure of the evanescent field of an optical bloch wave," *Physical Review Letters*, vol. 102, p. 023902, Jan 2009.

[40] C. Li, J. M. Holt, and A. L. Efros, "Far-field imaging by the veselago lens

made of a photonic crystal," *Journal of the Optical Society of America B*, vol. 23, pp. 490–497, March 2006.

[41] J. Christensen and F. J. G. de Abajo, "Anisotropic metamaterials for full control of acoustic waves," *Physcial Review Letters*, vol. 108, p. 124301, Mar 2012.

[42] B. C. Gupta and Z. Ye, "Theoretical analysis of the focusing of acoustic waves by two-dimensional sonic crystals," *Physical Review E*, vol. 67, p. 036603, Mar 2003.

[43] F. Cervera, L. Sanchis, J. V. Sánchez-Pérez, R. Martínez-Sala, C. Rubio, F. Meseguer, C. López, D. Caballero, and J. Sánchez-Dehesa, "Refractive acoustic devices for airborne sound," *Physical Review Letters*, vol. 88, p. 023902, Dec 2001.

[44] A. Håkansson, J. Sánchez-Dehesa, and L. Sanchis, "Acoustic lens design by genetic algorithms," *Physcial Review B*, vol. 70, p. 214302, Dec 2004.

[45] C.-H. Kuo and Z. Ye, "Sonic crystal lenses that obey the lensmaker's formula," *Journal of Physics D: Applied Physics*, vol. 37, no. 15, p. 2155, 2004.

[46] F. Cai, F. Liu, Z. He, and Z. Liu, "High refractive-index sonic material based on periodic subwavelength structure," *Applied Physics Letters*, vol. 91, no. 20, p. 203515, 2007.

[47] R. B. Greegor, C. G. Parazzoli, J. A. Nielsen, M. A. Thompson, M. H. Tanielian, and D. R. Smith, "Simulation and testing of a graded negative index of refraction lens," *Applied Physics Letters*, vol. 87, no. 9, p. 091114, 2005.

[48] D. R. Smith, J. J. Mock, A. F. Starr, and D. Schurig, "Gradient index metamaterials," *Physical Review E*, vol. 71, p. 036609, Mar 2005.

[49] E. Centeno, D. Cassagne, and J.-P. Albert, "Mirage and superbending effect in two-dimensional graded photonic crystals," *Physcial Review B*, vol. 73, p. 235119, Jun 2006.

[50] Q. Wu, J. M. Gibbons, and W. Park, "Graded negative index lens by photonic crystals," *Optics Express*, vol. 16, pp. 16941–16949, October 2008.

[51] Q. Cheng, H. F. Ma, and T. J. Cui, "Broadband planar luneburg lens based on complementary metamaterials," *Applied Physics Letters*, vol. 95, no. 18, p. 181901, 2009.

[52] H. Kurt and D. S. Citrin, "Graded index photonic crystals," *Optics Express*, vol. 15, no. 3, pp. 1240–1253, 2007.

[53] A. O. Cakmak, E. Colak, H. Caglayan, H. Kurt, and E. Ozbay, "High efficiency of graded index photonic crystal as an input coupler," *Journal of Applied Physics*, vol. 105, no. 10, p. 103708, 2009.

[54] M. Lu, B. K. Juluri, S.-C. S. Lin, B. Kiraly, T. Gao, and T. J. Huang, "Beam aperture modifier and beam deflector using gradient-index photonic crystals," *Journal of Applied Physics*, vol. 108, no. 10, p. 103505, 2010.

[55] E. Cassan, K.-V. Do, C. Caer, D. Marris-Morini, and L. Vivien, "Short-wavelength light propagation in graded photonic crystals," *Journal of Lightwave Technology*, vol. 29, pp. 1937–1943, Jul 2011.

[56] B. Vasi and R. Gaji, "Self-focusing media using graded photonic crystals: Focusing, fourier transforming and imaging, directive emission, and directional cloaking," *Journal of Applied Physics*, vol. 110, no. 5, p. 053103, 2011.

[57] K. Do, X. Le Roux, D. Marris-Morini, L. Vivien, and E. Cassan, "Experimental demonstration of light bending at optical frequencies using a non-homogenizable graded photonic crystal," *Optics Express*, vol. 20, pp. 4776–4783, February 2012.

[58] K. Deng, Y. Ding, Z. He, H. Zhao, J. Shi, and Z. Liu, "Graded negative index lens with designable focal length by phononic crystal," *Journal of Physics D: Applied Physics*, vol. 42, no. 18, p. 185505, 2009.

[59] S. Peng, Z. He, H. Jia, A. Zhang, C. Qiu, M. Ke, and Z. Liu, "Acoustic far-field focusing effect for two-dimensional graded negative refractive-index sonic crystals," *Applied Physics Letters*, vol. 96, no. 26, p. 263502, 2010.

[60] D. Torrent and J. Snchez-Dehesa, "Acoustic metamaterials for new two-dimensional sonic devices," *New Journal of Physics*, vol. 9, p. 323, July 2007.

[61] S.-C. S. Lin, T. J. Huang, J.-H. Sun, and T.-T. Wu, "Gradient-index phononic crystals," *Physcial Review B*, vol. 79, p. 094302, Mar 2009.

[62] S.-C. S. Lin, B. R. Tittmann, J.-H. Sun, T.-T. Wu, and T. J. Huang, "Acoustic beamwidth compressor using gradient-index phononic crystals," *Journal of Physics D: Applied Physics*, vol. 42, no. 18, p. 185502, 2009.

[63] A. Climente, D. Torrent, and J. Snchez-Dehesa, "Sound focusing by gradient index sonic lenses," *Applied Physics Letters*, vol. 97, no. 10, p. 104103, 2010.

[64] T. P. Martin, M. Nicholas, G. J. Orris, L.-W. Cai, D. Torrent, and J. Snchez-Dehesa, "Sonic gradient index lens for aqueous applications," *Applied Physics Letters*, vol. 97, no. 11, p. 113503, 2010.

[65] L.-Y. Wu and L.-W. Chen, "An acoustic bending waveguide designed by graded sonic crystals," *Journal of Applied Physics*, vol. 110, no. 11, p. 114507, 2011.

[66] T.-T. Wu, Y.-T. Chen, J.-H. Sun, S.-C. S. Lin, and T. J. Huang, "Focusing of the lowest antisymmetric lamb wave in a gradient-index phononic crystal plate," *Applied Physics Letters*, vol. 98, no. 17, p. 171911, 2011.

[67] L. Zigoneanu, B.-I. Popa, and S. A. Cummer, "Design and measurements of a broadband two-dimensional acoustic lens," *Physcial Review B*, vol. 84, p. 024305, Jul 2011.

[68] T. M. Chang, G. Dupont, S. Enoch, and S. Guenneau, "Enhanced control of light and sound trajectories with three-dimensional gradient index lenses," *New Journal of Physics*, vol. 14, no. 3, p. 035011, 2012.

[69] Y. Li, B. Liang, X. Tao, X.-f. Zhu, X.-y. Zou, and J.-c. Cheng, "Acoustic focusing by coiling up space," *Applied Physics Letters*, vol. 101, no. 23, p. 233508,

2012.

[70] S.-C. S. Lin, B. R. Tittmann, and T. J. Huang, "Design of acoustic beam aperture modifier using gradient-index phononic crystals," *Journal of Applied Physics*, vol. 111, no. 12, p. 123510, 2012.

[71] J. Zhao, R. Marchal, B. Bonello, and O. Boyko, "Efficient focalization of antisymmetric lamb waves in gradient-index phononic crystal plates," *Applied Physics Letters*, vol. 101, no. 26, p. 261905, 2012.

[72] A. Climente, D. Torrent, and J. Snchez-Dehesa, "Gradient index lenses for flexural waves based on thickness variations," *Applied Physics Letters*, vol. 105, no. 6, p. 064101, 2014.

[73] D. Torrent, Y. Pennec, and B. Djafari-Rouhani, "Effective medium theory for elastic metamaterials in thin elastic plates," *Physical Review B*, vol. 90, p. 104110, Sep 2014.

[74] X. Yan, R. Zhu, G. Huang, and F.-G. Yuan, "Focusing guided waves using surface bonded elastic metamaterials," *Applied Physics Letters*, vol. 103, no. 12, p. 121901, 2013.

[75] Y. Ye, M. Ke, Y. Li, T. Wang, and Z. Liu, "Focusing of spoof surface-acoustic-waves by a gradient-index structure," *Journal of Applied Physics*, vol. 114, no. 15, p. 154504, 2013.

[76] M.-J. Chiou, Y.-C. Lin, T. Ono, M. Esashi, S.-L. Yeh, and T.-T. Wu, "Focusing and waveguiding of lamb waves in micro-fabricated piezoelectric phononic plates," *Ultrasonics*, vol. 54, no. 7, pp. 1984 – 1990, 2014.

[77] J. Zhao, B. Bonello, R. Marchal, and O. Boyko, "Beam path and focusing of flexural lamb waves within phononic crystal-based acoustic lenses," *New Journal of Physics*, vol. 16, no. 6, p. 063031, 2014.

[78] A. H. Nayfeh, *Wave propagation in layered anisotropic media with applications to composites*. Elsevier Science, Amsterdam, Netherlands, 1995.

[79] M. Oudich, *Contribution à l' étude des cristaux phononiques à résonance locale dans les régimes sonique et hypersonique: approches théorique et expérimentale*. PhD thesis, Université Henri Poincaré, Nancy, French, November 2011.

[80] A. Khelif, B. Aoubiza, S. Mohammadi, A. Adibi, and V. Laude, "Complete band gaps in two-dimensional phononic crystal slabs," *Physcial Review E*, vol. 74, p. 046610, Oct 2006.

[81] J. Li, Y.-S. Wang, and C. Zhang, "Finite element method for analysis of band structures of three dimensional phononic crystals," in *2008 IEEE international ultrasonics symposium proceedings*, (Beijing), pp. 1468–1471, IEEE, IEEE, November 2008.

[82] C. Gomez-Reino, M. V. Perez, and C. Bao, *Gradient-Index Optics: Fundamentals and Applications*, vol. - of -. -: Springer, - ed., - Berlind:2002.

[83] R. Marchal, O. Boyko, B. Bonello, J. Zhao, L. Belliard, M. Oudich, Y. Pennec, and B. Djafari-Rouhani, "Dynamics of confined cavity modes in a phononic

crystal slab investigated by in situ time-resolved experiments," *Physial Review B*, vol. 86, p. 224302, Dec 2012.

[84] K. Kokkonen and M. Kaivola, "Scanning heterodyne laser interferometer for phase-sensitive absolute-amplitude measurements of surface vibrations," *Applied Physics Letters*, vol. 92, no. 6, p. 063502, 2008.

[85] A. H. Nayfeh and D. E. Chimenti, "Ultrasonic wave reflection from liquid-coupled orthotropic plates with application to fibrous composites," *Journal of Applied Mechnics*, vol. 55, pp. 863–870, December 1988.

[86] B. Hosten, "Reflection and transmission of acoustic plane waves on an immersed orthotropic and viscoelastic solid layer," *Journal of Acoustical Society of America*, vol. 89, pp. 2745–2752, June 1991.

[87] M. Castaings, P. Cawley, R. Farlow, and G. Hayward, "Single sided inspection of composite materials using air coupled ultrasound," *Journal of Nondestructive Evaluation*, vol. 17, no. 1, pp. 37–45, 1998.

[88] J. L. Rose, *Ultrasonic Waves in Solid Media*. Cambridge, United Kingdom, 1999.

[89] V. M. Alexander, S.-R. Kishore, Y. Fumin, D. Yanqing, and Z. Markus, "Interdigital sensors and transducers," *Proceedings of the IEEE*, vol. 92, pp. 808–845, May 2004.

[90] S. Benchabane, A. Khelif, J.-Y. Rauch, L. Robert, and V. Laude, "Evidence for complete surface wave band gap in a piezoelectric phononic crystal," *Physical Review E*, vol. 73, p. 065601, Jun 2006.

[91] C.-Y. Huang, J.-H. Sun, and T.-T. Wu, "A two-port zno/silicon lamb wave resonator using phononic crystals," *Applied Physics Letters*, vol. 97, no. 3, p. 031913, 2010.

[92] R. Marchal, *Métamatériaux acoustiques actifs*. PhD thesis, Université Pierre and Marie Curie, Paris, France, Decembre 2014.

[93] W. Śmigaj and B. Gralak, "Validity of the effective-medium approximation of photonic crystals," *Physcial Review B*, vol. 77, p. 235445, Jun 2008.

[94] Y. G. Ma, S. Sahebdivan, C. K. Ong, T. Tyc, and U. Leonhardt, "Subwavelength imaging with materials of in-principle arbitrarily low index contrast," *New Journal of Physics*, vol. 14, no. 2, p. 025001, 2012.

[95] J. C. Miano, J. Snchez-Dehesa, J. C. Gonzlez, P. Bentez, D. Graboviki, J. Carbonell, and H. Ahmadpanahi, "Experimental evidence of super-resolution better than $\lambda/105$ with positive refraction," *New Journal of Physics*, vol. 16, no. 3, p. 033015, 2014.

[96] F. M. Huang and N. I. Zheludev, "Super-resolution without evanescent waves," *Nano Letters*, vol. 9, no. 3, pp. 1249–1254, 2009.

[97] T. F. Rogers Edward and I. Z. Nikolay, "Optical super-oscillations: sub-wavelength light focusing and super-resolution imaging," *Journal of Optics*, vol. 15, no. 9, p. 094008, 2013.

[98] T. Brunet, J.-L. Thomas, and R. Marchiano, "Transverse shift of helical beams and subdiffraction imaging," *Physical Review Letters*, vol. 105, p. 034301, July 2010.

[99] Z. Liu, X. Zhang, Y. Mao, Y. Y. Zhu, Z. Yang, C. T. Chan, and P. Sheng, "Locally resonant sonic materials," *Science*, vol. 289, pp. 1734–1736, September 2000.

[100] Z. Liu, C. T. Chan, P. Sheng, A. L. Goertzen, and J. H. Page, "Elastic wave scattering by periodic structures of spherical objects: Theory and experiment," *Physical Review B*, vol. 62, pp. 2446–2457, Jul 2000.

[101] Z. Liang and J. Li, "Extreme acoustic metamaterial by coiling up space," *Physical Review Letters*, vol. 108, p. 114301, Mar 2012.

[102] V. Laude, Y. Achaoui, S. Benchabane, and A. Khelif, "Evanescent bloch waves and the complex band structure of phononic crystals," *Physical Review B*, vol. 80, p. 092301, Sep 2009.

[103] M. W. Kowarz, "Homogeneous and evanescent contributions in scalar near-field diffraction," *Applied Optics*, vol. 34, pp. 3055–3063, June 1995.

[104] K. G. Makris and D. Psaltis, "Huygensfresnel diffraction and evanescent waves," *Optics Communications*, vol. 284, no. 6, pp. 1686 – 1689, 2011.

[105] O. R. Bilal and M. I. Hussein, "Trampoline metamaterial: Local resonance enhancement by springboards," *Applied Physics Letters*, vol. 103, no. 11, p. 111901, 2013.

[106] C.-Y. Sun, J.-C. Hsu, and T.-T. Wu, "Resonant slow modes in phononic crystal plates with periodic membranes," *Applied Physics Letters*, vol. 97, no. 3, p. 031902, 2010.

[107] M. Oudich, M. B. Assouar, and Z. Hou, "Propagation of acoustic waves and waveguiding in a two-dimensional locally resonant phononic crystal plate," *Applied Physics Letters*, vol. 97, no. 19, p. 193503, 2010.

[108] M. Oudich, Y. Li, M. B. Assouar, and Z. Hou, "A sonic band gap based on the locally resonant phononic plates with stubs," *New Journal of Physics*, vol. 8, p. 083049, August 2010.

[109] R. Zhu, X. N. Liu, G. L. Huang, H. H. Huang, and C. T. Sun, "Microstructural design and experimental validation of elastic metamaterial plates with anisotropic mass density," *Physical Review B*, vol. 86, p. 144307, Oct 2012.

[110] T.-C. Wu, T.-T. Wu, and J.-C. Hsu, "Waveguiding and frequency selection of lamb waves in a plate with a periodic stubbed surface," *Physical Review B*, vol. 79, p. 104306, Mar 2009.

[111] Y. El Hassouani, C. Li, Y. Pennec, E. H. El Boudouti, H. Larabi, A. Akjouj, O. Bou Matar, V. Laude, N. Papanikolaou, A. Martinez, and B. Djafari Rouhani, "Dual phononic and photonic band gaps in a periodic array of pillars deposited on a thin plate," *Physcial Review B*, vol. 82, p. 155405, Oct 2010.

[112] M. Rupin, F. Lemoult, G. Lerosey, and P. Roux, "Experimental demonstra-

tion of ordered and disordered multiresonant metamaterials for lamb waves," *Physical Review Letters*, vol. 112, p. 234301, Jun 2014.

[113] D. M. Profunser, O. B. Wright, and O. Matsuda, "Imaging ripples on phononic crystals reveals acoustic band structure and bloch harmonics," *Physcial Review Letters*, vol. 97, p. 055502, Aug 2006.

[114] D. M. Profunser, E. Muramoto, O. Matsuda, O. B. Wright, and U. Lang, "Dynamic visualization of surface acoustic waves on a two-dimensional phononic crystal," *Physcial Review B*, vol. 80, p. 014301, Jul 2009.

[115] M. E. Korotyaeva, A. A. Kutsenko, A. L. Shuvalov, and O. Poncelet, "Love waves in two-dimensional phononic crystals with depth-dependent properties," *Applied Physics Letters*, vol. 103, no. 11, p. 111902, 2013.

[116] T.-W. Liu, Y.-C. Lin, Y.-C. Tsai, T. Ono, S. Tanaka, and T.-T. Wu, "Evidence of a love wave bandgap in a quartz substrate coated with a phononic thin layer," *Applied Physics Letters*, vol. 104, no. 18, p. 181905, 2014.

[117] A. Khelif, S. Mohammadi, A. A. Eftekhar, A. Adibi, and B. Aoubiza, "Acoustic confinement and waveguiding with a line-defect structure in phononic crystal slabs," *Journal of Applied Physics*, vol. 108, no. 8, p. 084515, 2010.

[118] D. Yudistira, Y. Pennec, B. Djafari Rouhani, S. Dupont, and V. Laude, "Non-radiative complete surface acoustic wave bandgap for finite-depth holey phononic crystal in lithium niobate," *Applied Physics Letters*, vol. 100, no. 6, p. 061912, 2012.

[119] A. Khelif, Y. Achaoui, S. Benchabane, V. Laude, and B. Aoubiza, "Locally resonant surface acoustic wave band gaps in a two-dimensional phononic crystal of pillars on a surface," *Physcial Review B*, vol. 81, p. 214303, Jun 2010.

[120] S. I. Rokhlin and L. Wang, "Stable recursive algorithm for elastic wave propagation in layered anisotropic media: Stiffness matrix method," *The Journal of the Acoustical Society of America*, vol. 112, no. 3, pp. 822–834, 2002.